

USING REAL TIME STATISTICAL DATA TO IMPROVE LONG TERM VOLTAGE STABILITY IN STOCHASTIC POWER SYSTEMS

A Thesis Presented

by

Samuel Chapman Chevalier

to

The Faculty of the Graduate College

of

The University of Vermont

In Partial Fulfillment of the Requirements
For the Degree of Master of Science
Specializing in Electrical Engineering

October, 2016

Defense Date: August 9th, 2016

Thesis Examination Committee:

Paul Hines, Ph.D., Advisor

Taras Lakoba, Ph.D., Chairperson

Mads Almassalkhi, Ph.D.

Cynthia J. Forehand, Ph.D., Dean of the Graduate College

Abstract

In order to optimize limited infrastructure, many power systems are frequently operated close to critical, or bifurcation, points. While operating close to such critical points can be economically advantageous, doing so increases the probability of a blackout. With the continued deployment of Phasor Measurement Units (PMUs), high sample rate data are dramatically increasing the real time observability of the power grids. Prior research has shown that the statistics of these data can provide useful information regarding network stability and associated bifurcation proximity. Currently, it is not common practice for transmission and distribution control centers to leverage the higher order statistical properties of PMU data. If grid operators have the tools to determine when these statistics warrant control action, though, then the otherwise unused statistical data present in PMU streams can be transformed into actionable information.

In order to address this problem, we present two methods that aim to gauge and improve system stability using the statistics of PMU data. The first method shows how sensitivity factors associated with the spectral analysis of the reduced power flow Jacobian can be used to weight and filter incoming PMU data. We do so by demonstrating how the derived participation factors directly predict the relative strength of bus voltage variances throughout a system. The second method leverages an analytical solver to determine a range of “critical” bus voltage variances. The monitoring and testing of raw statistical data in a highly observable load pocket of a large system are then used to reveal when control actions are needed to mitigate the risk of voltage collapse. A simple reactive power controller is then implemented that pushes the stability of the system back to a stable operating paradigm. Full order dynamic time domain simulations are used in order to test this method on both the IEEE 39 bus system and the 2383 bus Polish system. We also compare this method to two other, more conventional, controllers. The first relies on voltage magnitude signals, and the second depends only on local control of a reactive power resource. This comparison illustrates how the use of statistical information from PMU measurements can substantially improve the performance of voltage collapse mitigation methods.

Citation Page

Material from this thesis has been published in the following form:

Chevalier, S., Hines, P.. (2016). Identifying System-Wide Early Warning Signs of Instability in Stochastic Power Systems. IEEE Power and Energy Soc. Gen. Meeting, Jul. 2016.

Dedication

To Mom & Dad, to Hannah & Mike, to Kate & Joe.

...and in Him, all things hold together.

~ Colossians 1:17b

Acknowledgements

I would like to first express my deepest appreciation towards Dr. Paul Hines, my graduate advisor. I cannot quantify the impact he has already had on my academic future, my career goals, and the deep respect I have for the work we do. I would like to thank Dr. Mads Almassalkhi for the care he has shown for me as a student and for his willingness to serve on my thesis committee. Through his courses, his guidance, and his encouragement, I have been pushed to pursue my research endeavors with greater rigor and excellence. Similarly, Dr. Lakoba has been a valuable mentor to myself and to the others in our research group as we have investigated the Critical Slowing Down phenomena and its associated mathematics. I am deeply appreciative of his willingness to serve as chairperson of my thesis committee.

I would also like to acknowledge the impact that all of the faculty in the electrical engineering department has had on my studies at UVM. Dr. Varhue, Dr. Frolik, Dr. Oughstun, Dr. Titcomb, and Dr. Xia have all had unique contributions to my various successes and failures, and I am very satisfied with the experience I have been afforded while a student in this department.

Finally, my family, as listed in the Dedication section, and my friends, especially Mahraz Amini, have supported me and contributed to my successes over this last year in countless ways. Thank you all so much.

Table of Contents

Citation Page	ii
Dedication	iii
Acknowledgements	iv
List of Figures	ix
List of Tables	x
Chapter 1 Introduction	1
1.1 Motivation	1
1.2 Voltage Stability Concepts	2
1.2.1 Formulating the Power Flow Problem	3
1.2.2 Modeling Voltage Collapse	6
1.2.3 “Static” Voltage Collapse Analysis	8
1.2.4 Voltage Stability Index	14
1.2.5 Voltage Collapse and the Power Flow Jacobian	16
1.2.6 Voltage Collapse on the 2 Bus Power System	17
1.2.7 PV Curve Analysis: Graphical Results	18
1.2.8 Using Variance to Define a Stability Margin Threshold	21
1.2.9 PV Curve Analysis: Increasing Reactive Power Injection	23
1.2.10 PV Curve Analysis: Variance as a Robust Stability Margin Threshold Indicator	25
1.2.11 Quantifying Load Noise with First and Second Order Delta Methods	28
1.3 Critical Slowing Down	30
1.4 Continuation Power Flow and the Holomorphically Embedded Load Flow Method .	31
1.5 Forward	33
1.5.1 Thesis Outline	33
1.5.2 Key Innovations	33

Chapter 2 Spectral Analysis of the Reduced Power Flow Jacobian	34
2.1 Introduction	34
2.2 Mathematical Methods for Spectral Analysis	35
2.3 Uses of Participation Factors: Experimental Results	38
2.3.1 Polish Test Case System Overview	38
2.3.2 Evidence for Bus Voltage Variance Prediction	40
2.3.3 Evidence for Locating Generators with Elevated Voltage Autocorrelation . . .	42
2.4 Conclusions	43
Chapter 3 Using PMU Statistics to Reduce the Probability of Voltage Collapse	44
3.1 Introduction	44
3.2 Analytically Computing the Algebraic Variable Covariance Matrices	45
3.2.1 Power System Model Overview	45
3.2.2 State Variable Covariance Matrix	45
3.2.3 Algebraic Covariance Matrix	47
3.2.4 Autocorrelation and Cross-Correlation Matrices	48
3.2.5 Extension to the Line Current Covariance Matrix	48
3.2.6 Load Noise Model	48
3.3 Adapting HELM to Solve CPF	50
3.3.1 Using HELM to Solve the Power Flow Problem	50
3.3.1.1 Load Bus Model	51
3.3.1.2 Swing Bus Model	52
3.3.1.3 Generator Bus Model	52
3.3.1.4 Model Summary	53
3.3.1.5 Using the Derived Model to Solve Power Flow	54
3.3.2 CPF via HELM	56
3.3.2.1 Using the Holomorphic Parameter s to Scale Loads	56
3.3.2.2 CPF via HELM: PV and Swing Bus Model	57
3.3.2.3 CPF via HELM: PQ Bus Model	57
3.3.2.4 Choosing the Number of Recursive Routines N_c	58
3.3.2.5 Using a Holomorphic Function to Solve for a Critical Voltage	58

3.3.2.6	Using CPF via HELM to Estimate Voltage Collapse Loading Conditions	59
3.3.2.7	Testing CPF via HELM on the IEEE 39 Bus System	59
3.4	Defining a Probabilistic Loading Margin Based on Escape Probability	64
3.4.1	Employing the Ornstein-Uhlenbeck Process to Model $s(t)$	65
3.4.2	Survival Probability	66
3.4.3	Modeling the Diffusion Coefficient for Consistent Stability Margin Calculations	68
3.5	Using HELM to Compute Optimal Control Action	71
3.6	Controller Overview	71
3.7	Test Results	76
3.7.1	IEEE 39 Bus System: Reactive Power Controller Tests	76
3.7.1.1	System and Experiment Set Up	76
3.7.1.2	Simulation Processes	80
3.7.1.3	Test Results	80
3.7.2	IEEE 39 Bus System: Using Variance to Manage Active Power Injection . . .	86
3.7.3	Polish 2383 Bus System	89
3.7.3.1	System and Experiment Set Up	90
Chapter 4	Conclusions	95
4.1	Future Work	96
4.1.1	Generator Reactive Power Limits	96
4.1.2	Generator Participation Factors	97
4.1.3	Using Data Driven Covariance Matrices to Estimate the Jacobian Matrix .	100
Appendix A:	Technical Notation	102
Appendix B:	Common Abbreviations	103
Appendix C:	Nose Curve Derivation	104
Appendix D:	Quantifying Load Noise via Second Order Delta Method	107
Appendix E:	Detailed Power System Model Overview	111
Appendix F:	Line Current Covariance Matrix	116
Appendix G:	Solving CPF via HELM with Configurable Loading Rates	121
Appendix H:	Overview of Method for Critical Bus Voltage Solution	132

List of Figures

1.1	Two Bus Pi Model	3
1.2	Stability Indices for Lossless 39 Bus System with PF = 0.90	12
1.3	Stability Indices for Lossy 39 Bus System with PF = 0.90	13
1.4	Stability Indices for Lossy 39 Bus System with PF = 0.97	13
1.5	Two Bus System Circuit	14
1.6	Complex Voltage for Maximum Loading Conditions	15
1.7	Transmission to Distribution Meshed Network	16
1.8	Two Bus Power System Model	17
1.9	Standard PV Curves	19
1.10	PV Curve with Tap Changer Voltage Support	19
1.11	PV Curve with Shunt Voltage Support	20
1.12	PV Curve with Shunt Support and Stability Traces	20
1.13	Load Bus Voltage Variance (Low Load)	22
1.14	Load Bus Voltage Variance (High Load)	23
1.15	PV Curve Comparison for Static and Increasing Shunt Support	24
1.16	PV Curve Comparison for Static and Increasing Power Factors	24
1.17	Base Case Nose Curve	26
1.18	Load Variance Calculations	30
2.1	Comparison of Bus Voltage Variance and Participation Factors	40
2.2	Participation Factor Evolution	41
2.3	Average Autocorrelation of Generators	43
3.1	Topology of the IEEE 39 Bus System	60
3.2	39 Bus System Voltage Magnitudes as a Function of s	61
3.3	39 Bus System Complex Power Injections as a Function of s	62

3.4	39 Bus System Complex Power Injection Error	63
3.5	Controller 1: Variance and Mean Based Controller	74
3.6	Controller 2: Mean Based Controller	75
3.7	Controller 3: Controller Based on Synchronous Condenser Regulation	76
3.8	IEEE 39 Bus System with Load Pocket	77
3.9	Bifurcation Load Level for Each Controller Across 10 Trials	81
3.10	Voltage Magnitude and Variance for Controller1	82
3.11	Voltage Magnitude and Variance for Controller1	83
3.12	Voltage Magnitude and Variance for Controller1	83
3.13	Probability of Voltage Collapse in the 39 Bus System	84
3.14	Distance to Voltage Collapse	85
3.15	IEEE 39 Bus System with Condenser and Battery	87
3.16	39 Bus System Voltage Profile	88
3.17	Probability of Collapse on the 39 Bus System for Various Injections	89
3.18	Topology of the Polish System	90
3.19	Polish System Load Pocket	91
3.20	Polish System Load Pocket with SC Bus	91
3.21	Polish System Voltage Profiles	93
3.22	Polish System Average Voltage Magnitude and Variance for Controllers 1 and 2	94
4.1	Current Phasor Triangle	118

List of Tables

1.1	2 Bus System Stability Margins	21
1.2	2 Bus System Nose Curve Derivatives	21
3.1	HELM Model Summary	53
3.2	PV and Swing Bus Model Summary for CPF Application	57
3.3	Loading Rate Profiles	79
3.4	Simulation Processes and Methods	80
3.5	Initial, Largest, Smallest, and Average Load Level Reach for Controllers 1, 2, and 3 .	81
3.6	Average Percent Increase in Apparent Power Loading for Controllers 1, 2, and 3 . .	81
3.7	Bifurcation Loading Statistics for Controllers 1 and 2	92

Chapter 1

Introduction

1.1 Motivation

On an extremely hot day in July of 1987, the power system infrastructure in Tokyo Japan saw a dramatic increase in demand as millions of air conditioning units were turned on line. This demand spike occurred very rapidly and caused system-wide voltages to sag. Voltage collapse soon followed, leaving almost 3 million people without electrical power. According to [25] and [30], inadequate operational planning coupled with poor situational awareness were the primary causes of the blackout. Unfortunately, this is not an isolated voltage collapse incident: in order to optimize limited infrastructure, many power systems are frequently operated close to critical, or bifurcation, points. Although often economically advantageous [13], such practices greatly reduce the stability margins of the system and elevate the consequences of a rapid load build up or a sudden loss of stochastic renewable resources. This ultimately leaves power systems more vulnerable to the devastating effects of a catastrophic phenomena known as voltage collapse. To show its pervasiveness, [23] lists 26 voltage collapse related power system failures which have occurred over the last few decades. One of the more recent entries is the Northeast Blackout of 2003. At a total cost of over \$6 Billion and 11 lives lost, this event caused 50 million people to lose electrical power for a period of time. Although there were a variety of factors which lead to the outage, including ground faults and relay trips, the event ultimately crescendoed in voltage collapse caused by severely overloaded transmission infrastructure. According to a report compiled by U.S.-Canada Power System Outage Task Force directly after this incident, one of the four primary contributing factors to the collapse was an “Inadequate level of situation awareness” [2]. Despite the advent of the Phasor Measurement

Unit (PMU) and other advanced data collection techniques (such as fiber optic links and web based data sharing), situational awareness will only be achieved when control centers have the necessary tools to process and interpret these data. Through the work presented in this thesis, we hope to introduce methods which will contribute to transforming real-time high sample rate data collected from PMUs¹ into “actionable information” which will enhance the overall situational awareness of power grid operators.

1.2 Voltage Stability Concepts

Power systems are liable to experience a variety of critical transitions, including Hopf, pitchfork, and limit-induced bifurcations [26]. In this paper, though, we are primarily interested in factors associated with a classification known as *Long Term Voltage Instability* (LTVS). As outlined by the IEEE/CIGRE Joint Task Force on Stability Terms and Definitions [24], LTVS involves slower system changes associated with reactive power limits on generators (caused by field or armature current limiters), tap changers, and sustained load build up. A general definition of voltage stability (both long term and short term) is given by the authors of [24].

Voltage stability refers to the ability of a power system to maintain steady voltages at all buses in the system after being subjected to a disturbance from a given initial operating condition. (Kundur *et al.* 1390)

Power system operators are interested in maintaining acceptable LTVS in order to achieve two primary goals. The first and most obvious reason is so that voltage magnitudes remain in an acceptable region (typically between 0.95 and 1.05 p.u. (V)). The second reason is to avoid Voltage Collapse. As shall be shown, keeping an acceptable voltage magnitude profile does not always guarantee avoidance of voltage collapse, and even if a system is far from collapse, it still may have undesirably high or low bus voltages. Therefore, even though these two goals are interlinked, they are also highly decoupled in the sense that they must be addressed independently. Short term voltage stability, on the other hand, relates to electromechanical transients present in synchronous generators and transmission lines along with the dynamics of fast acting loads [24]. This thesis focuses on the slower progression towards voltage collapse rather than the short term instabilities.

¹To see of full list of common acronyms used throughout this document, refer to Appendix B.

1.2.1 Formulating the Power Flow Problem

Before further discussion on LTVs, we wish to succinctly derive the algebraic equations associated with the power flow problem; we employ them extensively in later chapters. Such an overview can be found in a variety of power system analysis textbooks [5, 21]. We begin by considering the two bus system shown in Figure 1.1. The pi model places a series admittance between the buses, and it distributes one half of the line's shunt capacitance to each bus. This is also known as the Unified Branch Model.

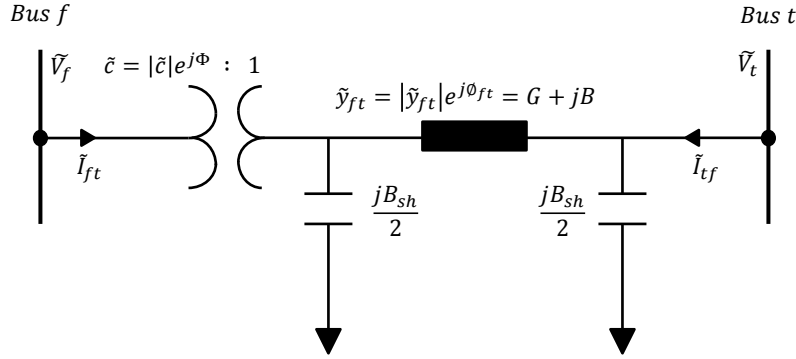


Figure 1.1: Two Bus Pi Model with Off-Nominal Turns Ratio Transformer

When standard transformers exist in a per unit transmission system, their presence (aside from losses) can be neglected unless they have an off nominal tap ratio or a phase shifting capability. Figure 1.1 shows the presence of such a transformer incorporated into the standard pi circuit model. The currents² $\tilde{I}_{f,t}$ and $\tilde{I}_{t,f}$ can be derived using Kirchhoff's Current Law and the transformer equations. The voltage across the secondary side of the transformer is given by \tilde{V}'_f and can be computed by rearranging the following equation, which relates turn ratios to winding voltages. The secondary side current $\tilde{I}'_{f,t}$ can be found in very similar way (notice the necessary complex conjugate operator on the current equation).

$$\frac{\tilde{V}_f}{\tilde{c}} = \frac{\tilde{V}'_f}{1} \implies \tilde{V}'_f = \frac{\tilde{V}_f}{\tilde{c}} \quad (1.1)$$

$$\tilde{I}_{f,t}(\tilde{c})^* = \tilde{I}'_{f,t}(1) \implies \tilde{I}'_{f,t} = \tilde{I}_{f,t}(\tilde{c})^* \quad (1.2)$$

²To see a full list of the technical notation used throughout this document, refer to Appendix A

We can use the known bus voltage values to compute the unknown currents.

$$\tilde{I}'_{f,t} = \tilde{V}'_f \left(j \frac{B_{sh}}{2} \right) + \left(\tilde{V}'_f - \tilde{V}_t \right) (\tilde{y}_{f,t}) \quad (1.3)$$

$$\tilde{I}_{t,f} = \tilde{V}_t \left(j \frac{B_{sh}}{2} \right) + \left(\tilde{V}_t - \tilde{V}'_f \right) (\tilde{y}_{f,t}) \quad (1.4)$$

The expressions for primary side winding complex voltage and complex current can be found by substituting the previous expressions.

$$\tilde{I}_{f,t} = \frac{\frac{\tilde{V}_f}{c} \left(j \frac{B_{sh}}{2} \right) + \left(\frac{\tilde{V}_f}{c} - \tilde{V}_t \right) (\tilde{y}_{f,t})}{\tilde{c}^*} \quad (1.5)$$

$$\tilde{I}_{t,f} = \tilde{V}_t \left(j \frac{B_{sh}}{2} \right) + \left(\tilde{V}_t - \frac{\tilde{V}_f}{\tilde{c}} \right) (\tilde{y}_{f,t}) \quad (1.6)$$

Both of these current values can now be placed in matrix form.

$$\begin{bmatrix} \tilde{I}_{f,t} \\ \tilde{I}_{t,f} \end{bmatrix} = \begin{bmatrix} \frac{\tilde{y}_{f,t} + j \frac{B_{sh}}{2}}{|\tilde{c}|^2} & -\frac{\tilde{y}_{f,t}}{\tilde{c}^*} \\ -\frac{\tilde{y}_{f,t}}{c} & \tilde{y}_{f,t} + j \frac{B_{sh}}{2} \end{bmatrix} \begin{bmatrix} \tilde{V}_f \\ \tilde{V}_t \end{bmatrix} \quad (1.7)$$

It can be noted that if the transformer does not cause phase shifting, the admittance matrix of (1.7) is symmetric (because \tilde{c} is purely real). Further, if the transformer also has a nominal turns ratio, the admittance matrix simplifies to the following symmetric matrix.

$$\begin{bmatrix} \tilde{y}_{f,t} + j \frac{B_{sh}}{2} & -\tilde{y}_{f,t} \\ -\tilde{y}_{f,t} & \tilde{y}_{f,t} + j \frac{B_{sh}}{2} \end{bmatrix} = \begin{bmatrix} Y_{f,f} & Y_{f,t} \\ Y_{t,f} & Y_{t,t} \end{bmatrix} \quad (1.8)$$

As will be shown, (1.8) is essential for the development of the Power Flow Problem. We now formally introduce the Y bus matrix which is defined in the following way:

$$\begin{aligned} Y_{i,i} &= \text{sum of admittances connected to bus } i \\ Y_{i,k} &= -(\text{sum of admittances connected between bus } i \text{ and } k) \text{ for } i \neq k \end{aligned}$$

Because the pi circuit model is used, the shunt admittance between any two buses is shared (equally) in the diagonal terms. This is only true, though, if no transformer with an off nominal turns ratio is present. When such a transformer is present, we must employ the admittance values given in (1.7).

For bus i in a power system, nodal current I_i is defined as the injected nodal current. Using Kirchhoff's Current Law, these injected currents can be calculated. The term $y_{i,k}$ is an admittance value, while $Y_{i,k}$ is a Y-bus value. The following analysis is completed for a system with $\tilde{c} = 1$ in order to simplify calculations. The results hold for the general case, though. For a 3 bus system, where transmission lines connect bus i to buses j and k , nodal current injection at bus i is computed as follows:

$$I_i = \left[y_{i,j}(V_i - V_j) + j \frac{B_{i,j}}{2} V_i \right] + \left[y_{i,k}(V_i - V_k) + j \frac{B_{i,k}}{2} V_i \right] \quad (1.9)$$

↓

$$I_i = V_i \left[y_{i,j} + j \frac{B_{i,j}}{2} + y_{i,k} + j \frac{B_{i,k}}{2} \right] + V_j [-y_{i,j}] + V_k [-y_{i,k}] = V_i(Y_{i,i}) + V_j(Y_{i,j}) + V_k(Y_{i,k}) \quad (1.10)$$

Alternatively, the equation for the injected nodal current in a generalized system can be written using the sum of the admittance bus elements. We assume there are N total buses in the system.

$$I_i = \sum_{k=1}^N Y_{i,k} V_k \quad i \in \mathcal{N} \quad (1.11)$$

The previous expression can then be vectorized.

$$\mathbf{I} = Y\mathbf{V} \quad (1.12)$$

where $\mathbf{V} = [V_1, V_2 \dots V_N]^\top$ and $\mathbf{I} = [I_1, I_2 \dots I_N]^\top$. Once injected currents are known, injected complex power can be calculated. At each bus, this is simply the product of the voltage and the complex conjugate of the injected current.

$$P_i + jQ_i = V_i \left[\sum_{k=1}^N Y_{i,k} V_k \right]^* \quad i \in \mathcal{N} \quad (1.13)$$

At this point, phasor notation of the voltages is invoked, and the admittance values are written in rectangular coordinates.

$$P_i + jQ_i = V_i \sum_{k=1}^N V_k e^{j(\theta_i - \theta_k)} [G_{i,k} - jB_{i,k}] \quad i \in \mathcal{N} \quad (1.14)$$

The voltage angle difference between node i and k is now defined as follows.

$$\theta_i - \theta_k = \theta_{i,k} \quad (1.15)$$

To decompose (1.14), the voltage phasor is split into rectangular coordinates.

$$\begin{aligned} P_i + jQ_i &= V_i \sum_{k=1}^N V_k [\cos(\theta_{i,k}) + j \sin(\theta_{i,k})] [G_{i,k} - jB_{i,k}] \\ &= V_i \sum_{k=1}^N V_k [G_{i,k} \cos(\theta_{i,k}) + B_{i,k} \sin(\theta_{i,k}) + jG_{i,k} \sin(\theta_{i,k}) - jB_{i,k} \cos(\theta_{i,k})] \quad i \in \mathcal{N} \end{aligned}$$

Now that the power injection expression has been decomposed, it can be separated into its real and reactive power components. Following are the steady state power flow equations.

$$P_i = V_i \sum_{k=1}^N V_k [G_{i,k} \cos(\theta_{i,k}) + B_{i,k} \sin(\theta_{i,k})] \quad i \in \mathcal{N} \quad (1.16)$$

$$Q_i = V_i \sum_{k=1}^N V_k [G_{i,k} \sin(\theta_{i,k}) - B_{i,k} \cos(\theta_{i,k})] \quad i \in \mathcal{N} \quad (1.17)$$

In order to solve the traditional power flow problem via Newton Raphson, we populate vector \mathbf{x} with the unknown voltage phase and magnitude variables from the appropriate sets, as noted by the subscripts.

$$\mathbf{x} = \begin{bmatrix} \boldsymbol{\theta}_r \\ \mathbf{V}_{\text{PQ}} \end{bmatrix}$$

We then build the Jacobian matrix and iterate towards a solution which drives the mismatch power injection vector to 0.

$$\mathbf{J}(\mathbf{x}) = \begin{bmatrix} \frac{\partial \mathbf{P}_r(\mathbf{x})}{\partial \boldsymbol{\theta}} & \frac{\partial \mathbf{P}_r(\mathbf{x})}{\partial \mathbf{V}} \\ \frac{\partial \mathbf{Q}_{\text{PQ}}(\mathbf{x})}{\partial \boldsymbol{\theta}} & \frac{\partial \mathbf{Q}_{\text{PQ}}(\mathbf{x})}{\partial \mathbf{V}} \end{bmatrix} \quad (1.18)$$

1.2.2 Modeling Voltage Collapse

To have a clear understanding of how to achieve LTVs, Voltage Collapse must be understood. Voltage collapse is a type of instability experienced by heavily loaded power systems which encounter monotonically decreasing voltages to the point of blackout [22]. In order to study any power system,

mathematical frameworks must be employed which models the physics of the real system. These models consist of a series Differential and Algebraic Equations (DAEs). A framework for these equations is given in [27].

$$\begin{bmatrix} \dot{\mathbf{x}} \\ \mathbf{0} \end{bmatrix} = \begin{bmatrix} \mathbf{f}(\mathbf{x}, \mathbf{y}, \lambda, \mathbf{p}) \\ \mathbf{g}(\mathbf{x}, \mathbf{y}, \lambda, \mathbf{p}) \end{bmatrix} \quad (1.19)$$

In this case, \mathbf{x} includes the differential state variables, \mathbf{y} includes the algebraic variables, λ is the bifurcation parameter (such as slow load build up) which the operator has no control over, and \mathbf{p} represent controller set points (such as tap settings). Finally, \mathbf{f} and \mathbf{g} are the differential and algebraic functions which govern the system. The algebraic power flow equations³ describe how the power flows through the transmission system, while a series of differential equations model the dynamics of the voltage controllers, governors, and machine models of the generators in a system. Since these equations (the power flow equations in particular) are nonlinear, there can be a variety of stable and unstable mathematical solutions for a given system operating point. Voltage collapse is typically considered to be a type of Saddle-Node bifurcation [11]. In this sort of bifurcation, multiple equilibrium points (or solutions) merge together and disappear [26] as the bifurcation parameter λ changes. In [11], Dobson *et al.* demonstrate mathematically how the stable and unstable operating points coalesce at the bifurcation point for a system with a single state variable. They also consider how the mathematics change once dynamic parameters (dynamic loads, tap changers, and generator limits) enter the system model. As they conclude,

Voltage collapse takes place when the system state falls into an expanding collapse region. A special case of this theory is when bifurcation occurs and leads to loss of equilibrium. Then, the whole state space becomes the collapse region. (Dobson *et al.* 45)

Hence, there may be regions in the state space which corresponds to monotonically decreasing bus voltages (a sign of voltage collapse) even if the saddle node bifurcation point is never actually reached.

For LTVS analysis, the slowly varying bifurcation parameter λ is often treated as load level. We now consider the load model, as it has an important impact on the bifurcation point. In [29], the ZIP load is introduced. In this load model, a fraction of the load is modeled as having a constant impedance, a fraction is modeled as having a constant current demand, and a fraction modeled

³Although differential equations are required to model the electromagnetic dynamics associated with transmission line flows, these dynamic processes are much fast than the dynamics of the machines and thus assumed instantaneous [16]. The power flow equations are thus reduced to a set of algebraic equations.

as having a constant power demand. Mathematically, this can be described by a set of algebraic equations.

$$P_{\text{ZIP}} = k (\alpha V^2 + aV + P_c) \quad (1.20)$$

$$Q_{\text{ZIP}} = k (\beta V^2 + bV + Q_c) \quad (1.21)$$

Where P_{ZIP} and Q_{ZIP} are the active and reactive loads at a bus and the coefficients a , b , α , and β determine the percentage of the load which should be governed by Z, I, or P. What is very important to note, though, can be seen in Figure 3 of [29]. Using a dynamic load model, they show that even though the maximum power transfer point (MPTP) for a simple two bus system sits on the nose curve of the PV curve, the SN bifurcation point occurs *after* this point; it sits on the low voltage side of the nose curve. For this reason, load models are extremely important to consider when studying voltage collapse, as stability margins can be shifted drastically depending on how the loads respond to voltage sag. Indeed, a system that relies exclusively on constant current and constant impedance loads cannot even be used to assess voltage collapse [7].

As noted in the supplementary information of [7], relying on constant power load models is very common in the voltage collapse literature when dealing with steady-state security analysis. Indeed, all of the analysis performed in this project assumes a balanced three phase system operating in sinusoidal steady state where all of the loads are constant power (with a slight frequency dependence during dynamic simulation). In fact, [7] notes that constant power analysis is actually the most conservative analysis which can be performed (when compared against an alternative ZIP load model), as numerical limits are hit much sooner with constant power loads. It therefore directly exposes the transfer limitations of a transmission system.

1.2.3 “Static” Voltage Collapse Analysis

The authors of [24] note that static analysis, where the dynamic models of power generation and fast acting loads are not considered, is often times an adequate approach for gauging LTVs margins and system performance. For example, [7] encodes the system-wide voltage phase shifts into the susceptance matrix of the network. After computing the open circuit voltages of the networks, an iteration free and closed form condition based on the decoupled power flow equations is developed which attempts to guarantee a unique, stable, high-voltage solution. In order to explain this method, we begin by writing out the reactive power injection equation at bus i for a lossless transmission

system (where $G_{ik} \sin(\theta_{ik}) \ll B_{ik} \cos(\theta_{ik})$) with K buses.

$$Q_i^{\text{inj}} = -V_i \sum_{k=1}^K V_k B_{ik} \cos(\theta_{ik}) \quad (1.22)$$

We now introduce a new term B'_{ik} which is the product of the voltage phase shift between buses and the susceptance (or strength of connection). This term is substituted in to the reactive power flow equation.

$$B'_{ik} = B_{ik} \cos(\theta_{ik}) \quad (1.23)$$

\Downarrow

$$Q_i^{\text{inj}} = -V_i \sum_{k=1}^K V_k B'_{ik} \quad (1.24)$$

We now re-order the system such that buses 1 through n are load (L) buses while buses $n+1$ through m are generator (G) buses. We then partition the susceptance matrix and thus define the following Coupling Matrix:

$$B' = \begin{bmatrix} B'_{LL} & B'_{LG} \\ B'_{GL} & B'_{GG} \end{bmatrix} \quad (1.25)$$

This matrix serves the following purpose. In typically loaded power system, we have the following relationship between complex current injections, complex bus voltages, and the Y bus matrix:

$$\tilde{\mathbf{I}} = \mathbf{Y}_{\text{bus}} \tilde{\mathbf{V}} \quad (1.26)$$

We now write a very similar expression this in terms of voltage magnitudes, current magnitudes, and the coupling matrix for our lossless, reordered system.

$$\mathbf{I} = B' \mathbf{V} \quad (1.27)$$

\Downarrow

$$\begin{bmatrix} \mathbf{I}_L \\ \mathbf{I}_G \end{bmatrix} = \begin{bmatrix} B'_{LL} & B'_{LG} \\ B'_{GL} & B'_{GG} \end{bmatrix} \begin{bmatrix} \mathbf{V}_L \\ \mathbf{V}_G \end{bmatrix} \quad (1.28)$$

In the open circuit model, there will be no current flowing into the load buses.

$$\mathbf{I}_L = \mathbf{0} = B'_{LL} \mathbf{V}_L + B'_{LG} \mathbf{V}_G \quad (1.29)$$

↓

$$-B'_{LL} \mathbf{V}_L = B'_{LG} \mathbf{V}_G \quad (1.30)$$

↓

$$\mathbf{V}_L^* = -B'^{-1}_{LL} B'_{LG} \mathbf{V}_G \quad (1.31)$$

This is how we define the pseudo-open circuit voltage vector \mathbf{V}_L^* of all the load buses. Of course, we have encoded the voltage phase shift into the matrix B' , so this is not a true open circuit voltage (OCV). The vector \mathbf{V}_G contains all of the generator set point voltages. Next, the authors of [7] introduce a critical matrix Q_{crit} .

$$Q_{\text{crit}} = \frac{1}{4} \text{diag}(\mathbf{V}_L^*) B'_{LL} \text{diag}(\mathbf{V}_L^*) \quad (1.32)$$

To understand how this critical matrix has been derived, we apply the reactive power flow equations to a simple 2 bus power system with generator bus i and load bus k with a single lossless transmission line connected in between. Next, we compute the reactive power injections at the load bus, where V_i is the voltage magnitude of the load and V_k is the voltage of the generator.

$$Q^{\text{inj}} = -V_i^2 B'_{ii} - V_i V_k B'_{ik} \quad (1.33)$$

We invoke the use of the open circuit voltage \mathbf{V}^* . From above, we compute it in the following way:

$$\mathbf{V}^* = -B'^{-1}_{LL} B'_{LG} \mathbf{V}_G = -\frac{1}{B_{ii}} B'_{ik} V_k \quad (1.34)$$

↓

$$-\frac{V^* B'_{ii}}{B'_{ik}} = V_k \quad (1.35)$$

We can now redefine the reactive power injection.

$$Q^{\text{inj}} = -V_i^2 B'_{ii} + V_i \left(\frac{V^* B'_{ii}}{B'_{ik}} \right) B'_{ik} \quad (1.36)$$

↓

$$0 = V_i^2 B'_{ii} - V_i V^* B'_{ii} + V_i^0 Q^{\text{inj}} \quad (1.37)$$

Of course, the open circuit voltage is static, as is the susceptance B'_{ii} . We can therefore solve for V_i using the quadratic equation.

$$V_i = \frac{V^* B'_{ii} \pm \sqrt{(V^* B'_{ii})^2 - 4 B'_{ii} Q^{\text{inj}}}}{2 B'_{ii}} \quad (1.38)$$

There is therefore a critical reactive power injection which cannot be exceeded.

$$(V^* B'_{ii})^2 - 4 B'_{ii} Q^{\text{inj}} = 0 \quad (1.39)$$

↓

$$Q^{\text{inj}}_{\text{crit}} = \frac{(V^* B'_{ii})^2}{4 B'_{ii}} = \frac{1}{4} B_{ii} (V^*)^2 \quad (1.40)$$

The similarity between (1.32) and (1.40) is clear. In this case of the two bus system, if $Q^{\text{inj}} = Q^{\text{inj}}_{\text{crit}}$, then we have the following:

$$V_i = \frac{V^* B_{ii} \pm \sqrt{0}}{2 B_{ii}} = \frac{V^*}{2} \quad (1.41)$$

The collapse voltage is one half of the open circuit voltage. They then define $\Delta = \frac{q}{q_{\text{crit}}}$. Then we have the following:

$$\delta_{\pm} = \frac{1 \pm \sqrt{1 - \Delta}}{2} = \frac{|V_i - V_i^*|}{V_i^*} \quad (1.42)$$

When $q = q_{\text{crit}}$, $\Delta = 1$ and

$$\delta_{\pm} = \frac{1}{2} = \frac{|V_i - V_i^*|}{V_i^*} \Rightarrow V_i = \frac{V^*}{2}$$

Retuning to a generalized n bus system, we now put the reactive loads in the vector $\mathbf{Q}_L = Q_1, \dots, Q_n$. Finally, we can compute the voltage stability index Δ .

$$\Delta = \|\Delta\|_\infty = \|Q_{\text{crit}}^{-1} \mathbf{Q}_L\|_\infty \quad (1.43)$$

According to the authors, a necessary and sufficient condition for voltage collapse is that $\Delta \geq 1$. Of course, this assumption is based on the decoupled power flow equations, so it is an optimistic upper bound, and it assumes that the collapse voltage is approximately one half the open circuit voltage (as shown above). In a system with a low power factor (lower than 0.9 lagging), this assumption is adequate, but in many other situations, voltage collapse can occur well before $\Delta = 1$.

We implemented this method on the IEEE39 bus system and applied increased uniform loading and generation until the system reached a collapse condition. Results from four tests are presented below. In the first test, the line resistances on all 46 lines were set to 0 to ensure a lossless operating paradigm and the average power factor of the loads was set to 0.90 lagging. Clearly, in this situation, Δ approaches the unity threshold when the system experiences a MPTP.

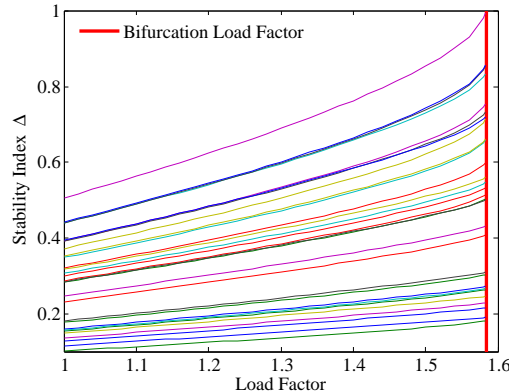


Figure 1.2: Stability Indices for each bus of the IEEE39 Bus System as Load Factor is increased right up to voltage collapse. The system parameters have been adjusted so the transmission lines are lossless (the Y-bus matrix is purely imaginary) and the average power factor of the loads is 0.90 lagging.

In the second test, the line resistances on all 46 lines were not set to 0, but the average power factor of the loads was set to 0.90 lagging. Clearly, in this situation, Δ is still an adequate measure of distance to collapse, but it under-performs the lossless system.

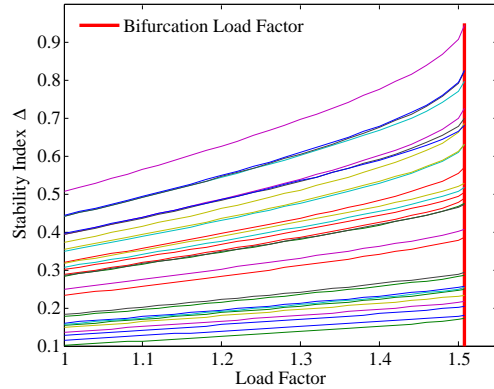


Figure 1.3: Stability Indices for the Lossy IEEE39 Bus System as Load Factor is increased right up to voltage collapse. The system parameters have been adjusted so the average power factor of the loads is 0.90 lagging.

In the third test, the line resistances on all 46 lines were not set to 0, but the average power factor of the loads was set to 0.97 lagging. Clearly, in this situation, Δ begins to become a very poor indicator of distance to bifurcation.

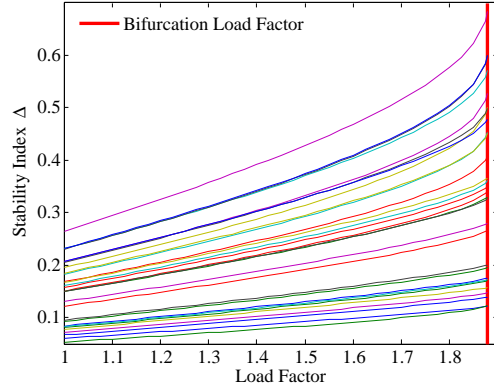


Figure 1.4: Stability Indices for the Lossy IEEE39 Bus System as Load Factor is increased right up to voltage collapse. The system parameters have been adjusted so the average power factor of the loads is 0.97 lagging.

In order to improve the inadequacies of this method (assumptions of losslessness and decoupling), we are attempting to answer the following question: **For a load bus with demand $(P_i + jQ_i)$, what value of $(0 + jQ_i^*)$ will cause an equivalent voltage drop across the transmission lines?**

Using a series of linear algebraic load transformations, we transformed all complex loading into purely reactive power loads which caused the same system-wide voltage profile. Although this was

successful, (1.43) was still not able to give us an accurate measure of distance to collapse under this transformation.

1.2.4 Voltage Stability Index

There are a number of other ways to employ static analysis in order to gauge proximity to voltage collapse. In [32], the authors employ a method for gauging proximity to voltage collapse by defining a ratio of voltage drop across a transmission line. Consider the simple two bus system shown in Figure 1.5. As shown, the sending side voltage is fixed at 1 per unit with a phase angle of $\theta = 0^\circ$.

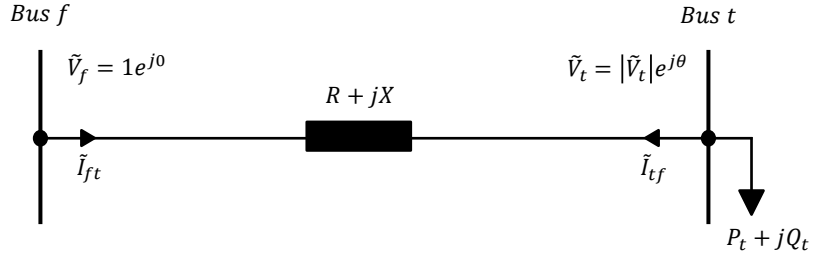


Figure 1.5: Simple two bus system circuit with fixed “from” bus voltage magnitude and phase

In order to solve for the load bus voltage as a function of power, the following relationships can be used.

$$\tilde{S} = \tilde{V}_t \tilde{I}_t^* = \tilde{V}_t \left(\frac{\tilde{V}_f - \tilde{V}_t}{R + jX} \right)^* = \tilde{V}_t \frac{1 - \tilde{V}_t^*}{R - jX} \quad (1.44)$$

↓

$$(R - jX) \tilde{S} = \tilde{V}_t - |\tilde{V}_t|^2 \quad (1.45)$$

Given resistance, reactance, and complex load parameters, the roots of (1.45) can be solved for, thus determining the phase and magnitude of the “to” bus voltage as load is increased. In Figure 1.6, this is done for several power factor profiles ($R = 0.1$ and $X = 1.0$). The complex power at the load is continually increased and the complex voltage at the receiving (or “to”) bus V_t is monitored.

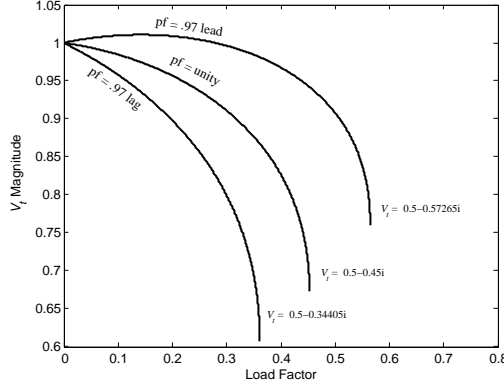


Figure 1.6: Complex Receiving End Voltage for Maximum Loading Conditions

Ramirez *et al.* claim that at the maximum loadability point (the point of voltage collapse), the ratio of the voltage drop across the transmission corridor to the “to” bus voltage is equal to one. This ratio functions as a Voltage Stability Index.

$$\text{VSI} = \frac{|\Delta V_{tf}|}{|V_t|} \cdot 100 \quad (1.46)$$

The results presented in Figure 1.6 indeed validate the claim that the voltage stability index approaches 1 as the system approaches voltage collapse. Mathematically, this is shown below.

$$\text{Leading Power Factor: } \frac{|\tilde{V}_f - \tilde{V}_t|}{|\tilde{V}_t|} = \frac{|(1 + j0) - (0.5 - j0.57265)|}{|0.5 - j0.57265|} = \frac{0.7602}{0.7602} = 1$$

$$\text{Unity Power Factor: } \frac{|\tilde{V}_f - \tilde{V}_t|}{|\tilde{V}_t|} = \frac{|(1 + j0) - (0.5 - j0.45)|}{|0.5 - j0.45|} = \frac{0.6727}{0.6727} = 1$$

$$\text{Lagging Power Factor: } \frac{|\tilde{V}_f - \tilde{V}_t|}{|\tilde{V}_t|} = \frac{|(1 + j0) - (0.5 - j0.34405)|}{|0.5 - j0.34405|} = \frac{0.6069}{0.6069} = 1$$

Clearly, maximum power transfer occurs when the ratio of the voltage drop is equal in magnitude to the load side voltage. In [32], the authors suggest using an alarm of some sort. For instance, if the VSI exceeds 80%, remedial action must be taken. Although this is a highly useful metric, its application is limited since most transmission systems are configured in some sort of a meshed network. An example is shown in Figure 1.7.

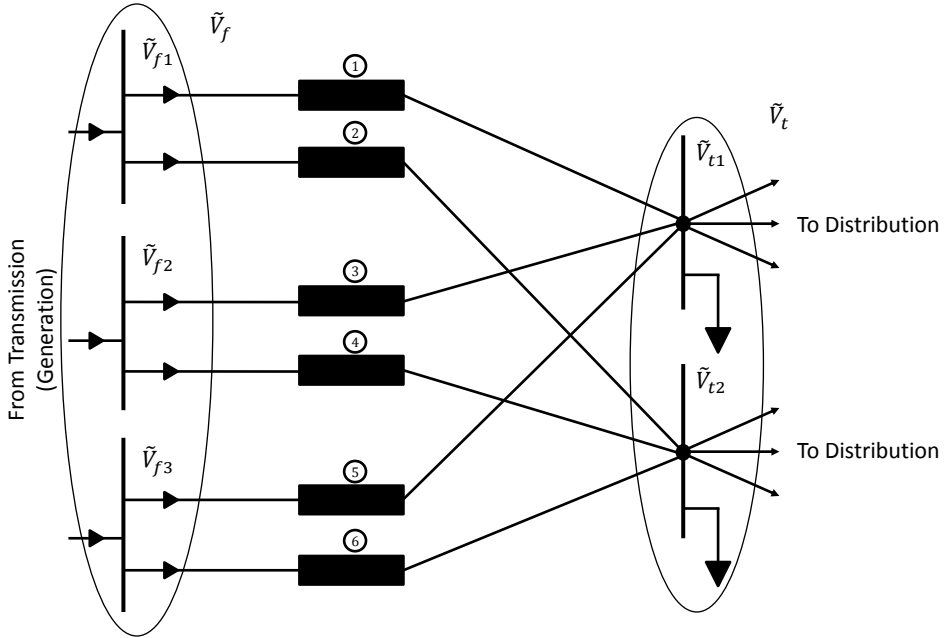


Figure 1.7: Transmission to Distribution Meshed Network

We have circled two subsets of buses since the methods in [32] focus on reducing meshed circuits into equivalent one-line diagrams on which 1.46 can be applied. The methods presented leverage a number of assumptions and are not universally applicable, but they still provide insight into new ways for thinking about the voltage collapse problem.

1.2.5 Voltage Collapse and the Power Flow Jacobian

The presence of voltage collapse results in the AC power flow equations failing to converge to a solution (via Newton-Raphson) [11]. Indeed, when a MPTP has been reached and the system experiences a saddle node bifurcation, the power flow Jacobian becomes singular [1]. There is a vast range of literature on different methods for gauging proximity to voltage collapse using the power flow, or load flow, Jacobian [38, 8, 14]. Singular value decomposition, modal analysis, sensitivity functions, and other power flow related methods all attempt to make determinations about where different parts of the system are operating on the nose curve and what sort of margin exists between stability and collapse. This topic is explored further in chapter 2 where we introduce a method which can use the participation factors of the reduced power flow Jacobian in order to weight or interpret real time phasor measurement unit data.

Although this sort of analysis is useful, it has been understood for many decades that system-wide

voltage stability cannot be determined exclusively by the condition of the power flow Jacobian. As identified by Sauer and Pai in [36], the absolute upper limit on system loadability is seldom reached, as the dynamics of the system will generally become unstable before the power flow Jacobian reaches singularity. This fact is confirmed in [35], where it is shown for a number of test cases that a Hopf bifurcation often precedes the saddle node bifurcation associated with voltage collapse. Additionally, reference [36] shows that only under very strict system conditions can analysis of the load flow Jacobian ever show signs of dynamic instability. Our experiments do no meet these conditions. The methods in this thesis primarily (but not entirely) apply static analysis to the LTV problem, so we readily acknowledge that they do not address the full spectrum of problems associated with power system stability (such as the Hopf bifurcation).

1.2.6 Voltage Collapse on the 2 Bus Power System

From generation down to transmission and distribution, there are a variety of mechanisms in a power system which hold system voltages high: Automatic Voltage Regulators, capacitor banks, tap changing transformers, and various other Flexible AC Transmission System (FACTS) devices. Predicting the onset of voltage instability, therefore, is made difficult thanks to the effort made by these devices to hold system voltages high [7]. Although switched shunt capacitors and dynamic tap settings maintain acceptable voltage profiles, they effectively conceal the low stability margin to (1) the operators and (2) the control devices which depend on voltage magnitude signals. To understand why this is the case, we perform algebraic analysis on the system shown in Figure 1.8. In this system, a constant voltage ($V_f = 1e^{j0}$) generator is placed at the “from” bus, and a constant power injection ($P_t + jQ_t$) is placed at the “to” bus. Capacitive shunt support is also placed at the load bus.

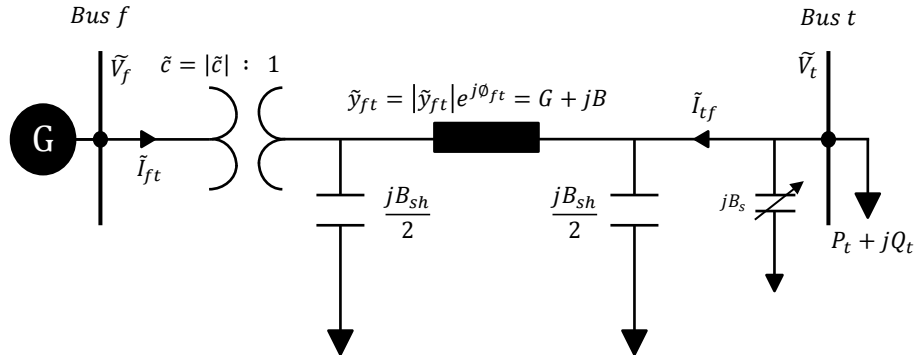


Figure 1.8: Two Bus Power System with Tap Changing Transformer and Shunt Support

Appendix C outlines the process of solving for the load bus voltage magnitude V_t . The derived expression uses series admittance (conductance & susceptance) terms. Line parameters are usually given in terms of series impedance (resistance & reactance). The relationship between these parameters is given below.

$$R = \Re \left\{ \frac{1}{G + jB} \right\} \Rightarrow G = \Re \left\{ \frac{1}{R + jX} \right\} \quad (1.47)$$

$$X = \Im \left\{ \frac{1}{G + jB} \right\} \Rightarrow B = \Im \left\{ \frac{1}{R + jX} \right\} \quad (1.48)$$

1.2.7 PV Curve Analysis: Graphical Results

In order to investigate the relationship between V_t and loading, power factor, tap settings, and shunt support, we set out to draw a range of PV curves. Before we do so, though, we consider the bifurcation point. This occurs when the low voltage solution and the high voltage solution coalesce and disappear. For a 2 bus network with regulated “from” bus voltage, we may predict when this point will occur by looking at the inner radicand of the quadratic expression for V_t (see Appendix C). The MPTP occurs when it equal to 0.

$$\left(2P_D G - 2\beta P_D \left(B + \frac{B_{sh}}{2} + B_s \right) - \frac{G^2}{c^2} - \frac{B^2}{c^2} \right)^2 - 4 \left(G^2 + \left(B + \frac{B_{sh}}{2} + B_s \right)^2 \right) \left(P_D^2 + \beta^2 P_D^2 \right) = 0 \quad (1.49)$$

Clearly, the bifurcation point, even for a two bus system, is concealed in the complex relationships of the system parameters. We now draw the PV curves for the system. Before doing so, we define the following parameters for the system. Obviously, these parameters are more representative of a large scale transmission system rather than a distribution system.

$$R = 0.01$$

$$X = 0.1$$

$$\frac{B_{sh}}{2} = 0.5$$

For the first set of PV curves, consider the situation where there is no voltage support. Therefore, we encode the following parameters:

$$c = 1$$

$$B_s = 0$$

We draw the PV curves for a system with the following power factors: 1.0, 0.95, and 0.80.

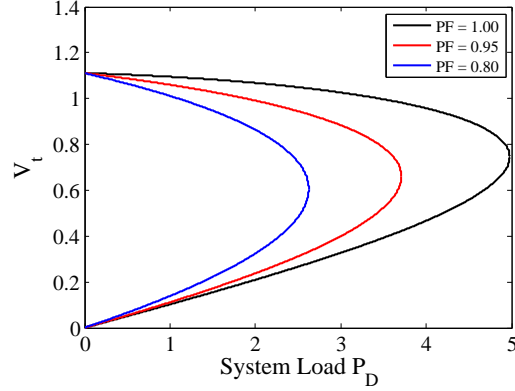


Figure 1.9: Load Bus Voltage as a Function of P_D for Various Power Factors ($c = 1$ and $B_s = 0$)

What can be noticed is that as power factor drops, the MPTP gets pushed closer to the y-axis (essentially, the system can handle less and less load). What should also be noticed is for higher power factors, the MPTP occurs closer to nominal system voltage. Next, we plot the same system with a fixed power factor and variable tap ratios.

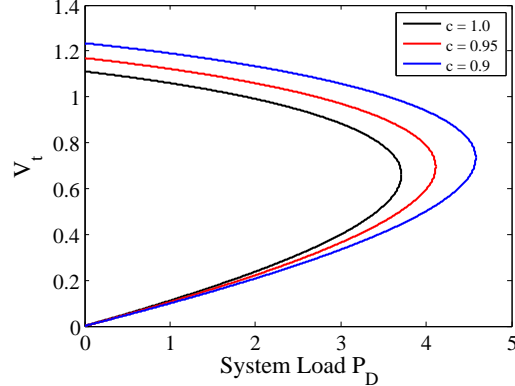


Figure 1.10: Load bus Voltage as a Function of P_D for Various Tap Ratios ($PF=0.95$, $B_s = 0$)

As the tap ratio is decreased (which effectively raises the voltage on the secondary), more voltage support is applied, but again, the MPTP is pushed closer into the nominal voltage range. This can act to conceal the true stability margin of the system. Next, we plot the same system with a fixed tap ratio and variable shunt support.

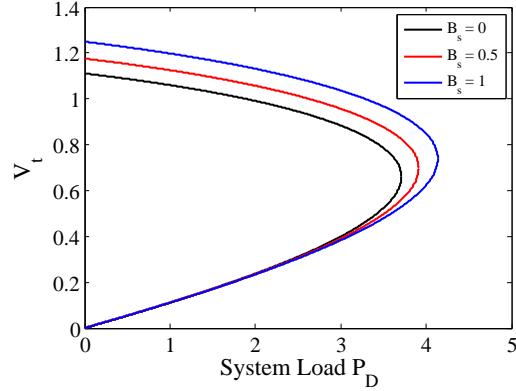


Figure 1.11: Load Bus Voltage as a Function of P_D for Various Levels of Shunt Support

Again, it is shown how supporting voltage has the affect of pushing the MPTP closer the nominal system voltage. To prove this point, we edit the previous plot by adding two lines: one shows an arbitrary minimum tolerable system voltage (0.90 p.u.), and one showing the voltage magnitude at the MPTP for each paradigm. The distance between these lines represents the voltage stability margin of the system.

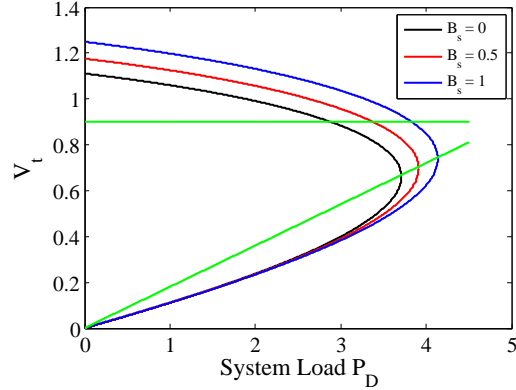


Figure 1.12: Load Bus Voltage as a Function of P_D for Various Shunt Values. Green Voltage Magnitude Traces are shown: the lower trace connects the noses of the PV plots while the upper trace shows an arbitrary minimum tolerable system voltage.

Clearly, as the shunt support and loading jointly increase, the stability margin effectively decreases for a given voltage magnitude. We consider these three systems operating at 0.9V with their respective loads, and we consider the stability margin (in terms of P_D) for each system.

Shunt Support	Load Bus Voltage (pu)	Stability Margin (pu)
$B_s = 0$	0.9	0.8260
$B_s = 0.5$	0.9	0.5260
$B_s = 1.0$	0.9	0.3060

Table 1.1: 2 Bus System Stability Margins

Although each system has the same mean load bus voltage, the stability margin of the third system is less than half of the first system (of course, the third system sees a much higher load). We can begin to understand the stability margin by considering the derivative of the nose curve. For each system, at the point of bifurcation, the derivative of the curve, with respect to P_D , approaches $-\infty$. In the following table, we take the derivative of each curve when voltage is 0.90 p.u.:

Shunt Support	Load Bus Voltage (pu)	Derivative (pu/pu)	Derivative Squared
$B_s = 0$	0.9	-0.1315	0.0173
$B_s = 0.5$	0.9	-0.1784	0.0318
$B_s = 1.0$	0.9	-0.2536	0.0643

Table 1.2: 2 Bus System Nose Curve Derivatives

Again, although the nominal bus voltages are equal, the derivative of the third curve is more than twice as large as the derivative of the first curve. The final column of the table represents the square of the derivative. This value will be proportional to the variance of the load bus voltage, as will be shown in the following section.

$$\sigma_{V_t}^2 \sim \left(\frac{dV_t}{dP_D} \right)^2$$

1.2.8 Using Variance to Define a Stability Margin Threshold

As load increases and a system moves farther out on the PV nose curve, the variance of the load bus voltage (which is driven by the load noise) also increases. In order to quantify the bus voltage variance $\sigma_{V_t}^2$, the Delta Method may be used in order to compute the variance of the load bus voltage function. To show how to do so, a function $g(X)$ is linearized via the Taylor Series approximation. The linearization point is μ_X , which is the mean value of the random variable X .

$$g(X) \approx g(\mu_X) + g'(\mu_X)(X - \mu_X) \quad (1.50)$$

Next, the variance operator is applied to both sides of the expression.

$$\begin{aligned}\text{Var}(g(X)) &\approx \text{Var}(g(\mu_X) + g'(\mu_X)(X - \mu_X)) \\ &\approx g'(\mu_X)^2 \text{Var}(X)\end{aligned}\quad (1.51)$$

Therefore, we have that the variance of $g(X)$ is approximately equal to the variance of the random variable X weighted by the squared first derivative of the function g evaluated at the mean value of X .

$$\sigma_{g(X)}^2 \approx g'(\mu_X)^2 \sigma_X^2 \quad (1.52)$$

If we have knowledge of the load noise and the load mean, we can quantify $\sigma_{V_t}^2$ by taking the derivative of ??.

$$\sigma_{V_t}^2 \approx \left(\frac{dV_t}{dP_D} \Big|_{E[P_D]} \right)^2 \sigma_{P_D}^2 \quad (1.53)$$

The following two figures show this method in action. A two bus power system is simulated, and the load noise is increased proportionally to the increase in load. At each step, $\sigma_{P_D}^2$ and $E[P_D]$ are numerically calculated, and then $\sigma_{V_t}^2$ is analytically computed. For increasing load values (up to $P_D \approx 1.29$), we compute the variance with (1.53).

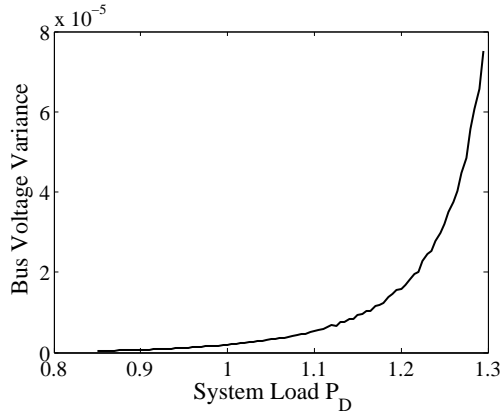


Figure 1.13: Bus Voltage Variance as Load Increases (Variance computed analytically)

The load can be increased even more (up to $P_D \approx 1.37$) in order to show the dramatic effects of increased loading on variance. Clearly, the variance approaches ∞ as the loading level approaches the nose curve.

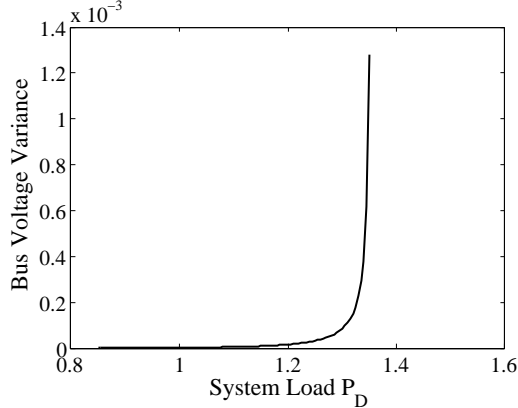


Figure 1.14: Bus Voltage Variance as Load Increases (Variance computed analytically)

One way of predicting the distance to static voltage collapse, which we leverage heavily in Chapter 3, is by drawing the nose curve for a system, defining a complex power stability margin on the curve which should not be exceeded, and then calculating the (steady state) bus voltage variance at this threshold. A full dynamical system model, as reviewed in section 3.2, is employed in computing this expected variance. If measured bus voltage variance exceeds this calculated variance value, then the complex power stability margin has been crossed (assuming perfect model and measurement data).

1.2.9 PV Curve Analysis: Increasing Reactive Power Injection

In order to show how much more useful variance, rather than voltage magnitude, is in assessing voltage stability, we formulate the following experiment. For the two bus system depicted in Figure 1.8, as load is increased, reactive power (via increasing shunt support) injection is also increased in order to keep voltage magnitude constant. The power factor of the constant power load is kept constant at 0.97 lagging.

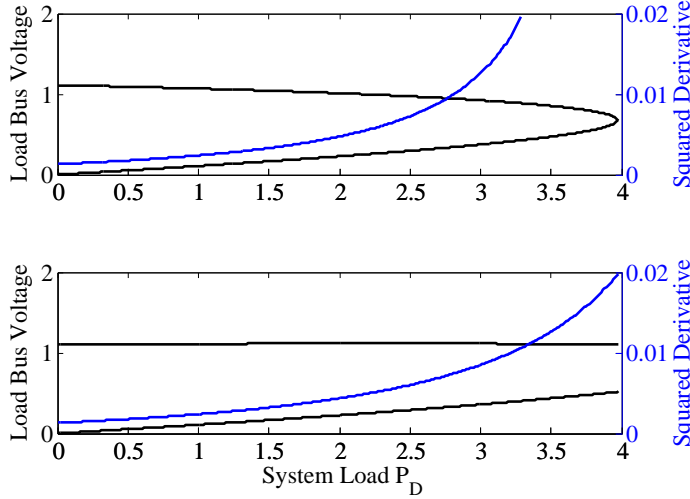


Figure 1.15: Load Bus Voltage Magnitude and PV Curve Derivative Squared as a Function of System Load ($\text{PF} = 0.97$ and $c = 1$). In the top plot, shunt support is non-existent. In the bottom plot, shunt support increases (from 0 to 1.75) to hold load bus voltage constant as load increases.

There are a host of other conceivable situations where bus voltage variance increases dramatically while bus voltage magnitude remains relatively fixed. For example, a tap changer or an auto-transformer can hold voltage magnitude high while the stability margin of the system diminishes. Additionally, a situation can arise where the power factor of a load swings high while the loading of the bus increases. This situation is shown in the following figure.

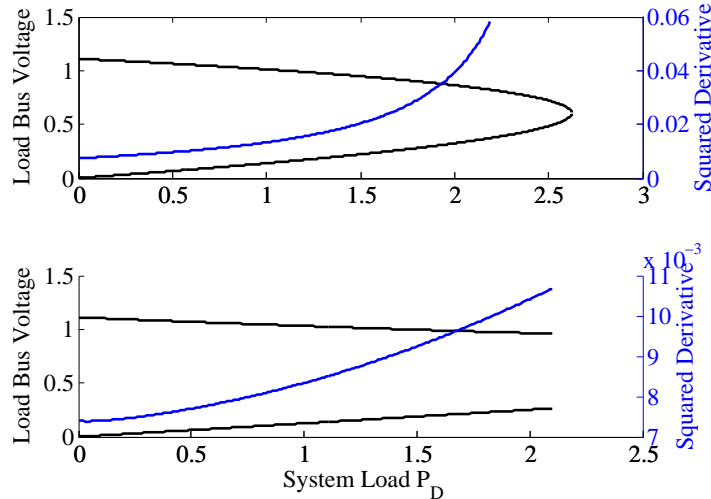


Figure 1.16: Load Bus Voltage Magnitude and PV Curve Derivative Squared as a Function of System Load ($B_s = 0$ and $c = 1$). In the top plot, power factor is fixed at 0.80. In the bottom plot, power factor approaches unity as load increases.

1.2.10 PV Curve Analysis: Variance as a Robust Stability Margin Threshold Indicator

In the previous subsection, we introduce the concept of the voltage stability margin for a constant power load. In [22], Dobson's research group presents the loading margin in the following way:

For a particular operating point, the amount of additional load in a specific pattern of load increase that would cause a voltage collapse is called the loading margin... Loading margin is an accurate measure of proximity to voltage collapse which takes full account of system limits and nonlinearities. (Greene *et al.* 262)

As discussed in 1.2.2, voltage collapse is a dynamic event which requires the full set of system DAEs to be understood. Since we are concerned with identifying the point of "static" voltage collapse in this project, we employ loading parameters, set points, and control settings, along the algebraic equations and system topology which link these quantities, in determining the location of a fold bifurcation (or MPTP). This method is validated in [12]. Although we use a full DAE system model to (1) estimate the system's algebraic variable covariance matrix and (2) validate the stability of the system with dynamic time domain simulations, the methods we employ for gauging the distance to voltage collapse do not consider the dynamics of the system. [12] acknowledges that even though dynamics can be disregarded when studying the point of fold bifurcation, analysis of an oscillatory Hopf bifurcation requires a full system model, and Hopf can occur before, during, or after the fold bifurcation.

As outlined in the previous subsection, variance measurements can be used in real time to determine proximity to a threshold. To compute this threshold, though, we base our continuation method on scaling the complex power load such that the power factor of the load does not change. For a two bus system, though, if power factor of the load does change while loading increases, **will the variance threshold still represent a valid, predefined stability margin?**

To investigate this question, we consider an example. We start by defining the following parameters for the system. Once again, these parameters are more representative of a large scale transmission system rather than a distribution system, and they have been tuned for a convenient bifurcation point.

$$R = 0.013$$

$$X = 0.13$$

$$\frac{B_{sh}}{2} = 0.5$$

$$B_s = 1.0$$

This operating paradigm, with a power factor of 0.90 lagging, has the following nose curve.

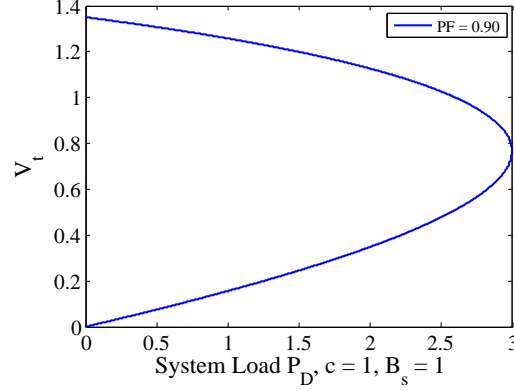


Figure 1.17: 2 Bus System Nose Curve for PF = 0.90

If the system is operating at $P_D = 2.5$, then $V_t = 1.027$ and $\beta = \tan(\cos^{-1}(PF))$. Let's now assume that the critical threshold (which the operator does not want to pass) is located at $P_D = 2.75$. This means that at the critical threshold, P_D can increase by 0.25 before collapse is reached ($3.0 - 2.75$). This corresponds to the following amount of complex power.

$$\begin{aligned} S &= 0.25 (S_{\text{Base}}) \\ &= 0.25(1 + j0.484) \\ &= 0.25 + j0.121 \end{aligned}$$

Therefore, we have defined the following stability margin.

$$\text{Stability Margin} \Rightarrow 0.25 + j0.121$$

If the stability margin is reached on the nose curve, the load bus voltage will be $V_t = 0.953$. The

derivative of the nose curve in Figure 1.17 at $P_D = 2.75$ has the following numerical value.

$$\frac{dV_t}{dP_D} = -0.3648$$

This is an important value since the bus voltage variance at the load is proportional to the square of this derivative value.

$$\sigma_{V_t}^2 \approx \left(\frac{dV_t}{dP_D} \Big|_{E[P_D]} \right)^2 \sigma_{P_D}^2 \quad (1.54)$$

According to the noise model which we are using (it shall be formally introduced in the next two chapters), $\sigma_{P_D}^2 = \mu_{P_D}^2 \sigma_n^2$, where μ_{P_D} is the average value (or operating point) of P_D , and σ_n is the standard deviation of the noise which is applied to the load (it can also be thought of as $\sigma_{P_D}^2$ when $\mu_{P_D} = 1$). For this example, we set $\sigma_n^2 = 1$ for simplicity. Obviously, the magnitude of the load scales the noise. Therefore, the bus voltage variance can be analytically calculated.

$$\sigma_{V_t}^2 = 1.007$$

We now perform the following experiment: the power factor of the load is raised to 0.95 (reactive demand drops low), and the load increases from $P_D = 2.5$ up to a value such that bus voltage variance hits 1.007. The load value at which this occurs has the following properties.

$$PF = 0.95$$

$$P_D = 3.1474$$

$$V_t = 0.977$$

$$\sigma_{V_t}^2 = 1.007$$

When the original system ($PF = 0.90$) experienced this sort of bus voltage variance, it had a stability margin of $0.25 + j0.121$. When power factor swings high and a BVV of $\sigma_{V_t}^2 = 1.007$ is experienced, the new stability margin is $0.2374 + j0.115$. Using this noise model, therefore, we find that the change in stability margin is small.

$$100 \times \left| \frac{[0.25 + j0.121] - [0.2374 + j0.115]}{[0.2374 + j0.115]} \right| = 5.3\%$$

For a drastically altered power factor, we find that the original stability margin is still an acceptable estimate of the distance to voltage collapse in this situation despite the fact that it is slightly too liberal. Intuitively, if power factor swings low, we will witness the opposite phenomena: our original stability margin estimate will be too conservative (a more probable situation and a more desirable problem). Assuming the power factor does not change by more than ± 0.05 in either direction though, the stability margin estimate will be a reliable figure.

The most important take away from this analysis, though, is that although power factor swings do not substantially change voltage stability and its associated margins margins, voltage magnitudes are effected severely. In the case of increasing power factor (due to dynamic reactive compensation or load changes), voltage my stay relatively constant while variance shifts dramatically. For this reason, real time stability monitoring using bus voltage mean values will not be nearly as successful as relying on the stability information encoded in the variance of the bus voltage. If loads do not change exactly as the operator predicts they will, mean values can be unreliable. This is a very important example for the following reason. In chapter 3, we define a stability margin in terms of a critical variance profile for a series of load buses in a load pocket. In doing so, the following question could be asked: can this critical profile just use voltage mean instead of voltage variance? We show that there is much system stability information encoded in the variance which the mean statistic, even when leveraged analytically, does not contain. If power factor, tap settings, or some of form of voltage regulation occurs without instantaneous operator knowledge, the system may appear to be stable based on mean measurements, while in fact it may not be. The variance of the voltage, however, provides useful information about proximity to voltage collapse even when voltage mean is not helpful.

1.2.11 Quantifying Load Noise with First and Second Order Delta Methods

As given by (1.53), we can quantify the bus voltage variance of a load bus if we have (1) an analytical expression for bus voltage magnitude as a function of load and (2) a value for load noise variance. The load noise may be an unknown parameter, so we must consider how it can be quantified. We present two ways for doing so. Assuming a PMU is able to measure the voltages and currents of loads connected to bus i , we can compute the load noise variance directly with (1.55). For clarity, $V_i(t)$ and $I_{L_i}(t)$ are the current and voltage serving the load at bus i at time t , and μ_{P_D} is the mean load

value.

$$\sigma_{P_D}^2 = \sum_{t=1}^T (\Re \{ V_i(t) I_{L_i}^*(t) \} - \mu_{P_D})^2 \quad (1.55)$$

This attempt represents a straightforward method for quantifying load noise. If we assume the bus voltage variance is known at a particular bus, though, we may invert the delta method and solve for load noise. Of course, the current model we are using assumes a two bus system with fixed generator voltage at the “from” bus. Rarely would such a situation arise, but we will still explore this method, as it can be generalized into a more realistic context. We start by inverting the delta method.

$$\sigma_{P_D}^2 \approx \frac{\sigma_{V_{tr}}^2}{\left(\frac{dV_t}{dP_D} \Big|_{E[P_D]} \right)^2} \quad (1.56)$$

Since this expression is based on the linearization of (??), we consider if the accuracy of the load variance calculation changes significantly when we incorporate the third term of the Taylor Series. A higher order (second order) Taylor Series approximation can be employed. This derivation outlined in Appendix D. Using the defined variables c_1 , c_2 , and c_3 , the final expression is given by (1.57).

$$\sigma_P^2 = \frac{-(c_2) \pm \sqrt{(c_2)^2 - 4c_1c_2}}{2c_1} \quad (1.57)$$

In order test the validity of this expression, a simple 2 bus system is simulated in the MATLAB toolbox PSAT. For a variety of load levels, an analytical solver (see Section 3.2) was used to compute the full covariance matrix for the entire system. After each solve, the expected mean and variance of the bus voltage and load demand are computed. In Figure (1.18), three quantities are contrasted: first order delta method load variance estimation, second order delta method load variance estimation, and expected load variance (according to the model we use to inject load noise).

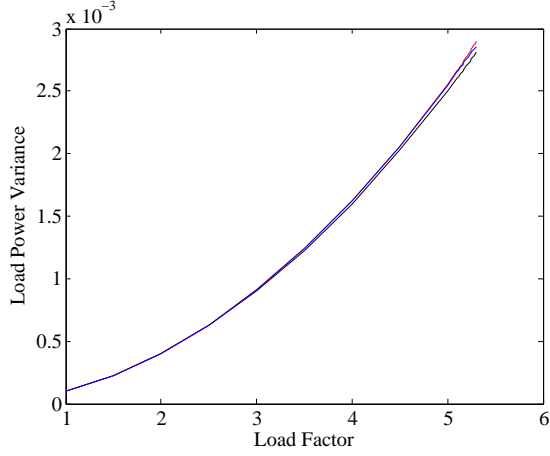


Figure 1.18: Load Noise Quantification. The top red line is the first order delta method estimation, the middle blue line is the second order delta method estimation (see equation (1.57)), and the bottom black line is the true load variance.

As can be seen in Figure 1.18, the first and second order delta methods yield almost identical approximations (right up to just before the bifurcation). A second order approximation, therefore, will not be used in any of the statistical calculations moving forward.

1.3 Critical Slowing Down

Across a variety of complex systems, there is increasing evidence that indicators of looming critical transitions are concealed in the statistics of state variable time series data [37]. This fact has been evidenced in many complex systems, including ecological networks, financial markets, the human brain, and power systems [37, 18]. Researchers have even found that human depression onset can be predicted by these same statistical properties [41]. Termed Critical Slowing Down (CSD) in the statistical physics literature [44], this phenomena is most heavily evidenced through elevated variance and autocorrelation [10]. When stressed, systems experiencing CSD require longer periods to recover from stochastic perturbations.

Real power systems are burdened with stochastic loads and an increasing level of renewable energy penetration. Consequently, researchers have begun to quantify the presence of CSD in large scale power system networks. Strong connections have been drawn between bifurcation theory and the elevation of certain statistics in voltage and current time series data [17, 19, 20, 18, 31, 9]. When approaching a transition, reference [9] has quantified increases in variance and autocorrelation in bus voltage. Similarly, reference [31] computes the power system state vector auto-correlation function to

gauge collapse probability. Finally, variance and autocorrelation are measured in an unstable power system in [18] across many state variables. The results indicate that variance of bus voltages and autocorrelation of line currents show the most useful signals of CSD. Current angles, voltage angles, generator rotor angles, and generator speeds did not yield strong CSD signs capable of indicating proximity to a bifurcation. Although many are useful indicators, not all variables in a complex system exhibit CSD sufficiently early enough to be useful EWSs [6]. For instance, reference [18] destabilized a simulated power system by over stressing all load buses. Signals were then collected from many nodes in this system, and certain nodes conclusively did not show early and strong CSD warning signs.

In order to estimate the time series statistics associated with an arbitrarily sized power system approaching a critical transition, the work completed in [18] is of particular interest. In this work, Ghanavati *et al.* develop and validate a semi-analytical method for calculating the state variable covariance matrix by solving the continuous Lyapunov equation for a dynamically modeled and stochastically forced power system. A series of linear transformations can be applied to the state variable covariance matrix in order to generate the algebraic covariance and autocorrelation matrices. From such calculations, the statistics associated with voltage and current phase and magnitude across all buses may be estimated.

1.4 Continuation Power Flow and the Holomorphically Embedded Load Flow Method

One classic approach to safeguarding a system from voltage instability comes through solving the Continuation Power Flow (CPF) problem. As clearly outlined in the seminal paper [1], CPF involves assigning a series of loading rates and power factor parameters to loads at PQ buses and generation rates (or participation factors) to the active power generation at PV buses. An iterative approach, based on a modified Newton-Raphson power flow solver, is used to draw the nose curves of system. In order to compute the critical bus voltage variances associated with a system approaching the loss of LTVS, we use a version of CPF which is analytically computed via the Holomorphic Embedded Load Flow Method (HELM).

As introduced in [40], iterative numerical solver techniques such as Gauss-Seidel and Newton-Raphson (NR) encounter a range of numerical issues when employed to solve a series of nonlinear

power flow equations. Unexpected divergence and undesired (low voltage) solutions are two common examples which are especially problematic when a power system is close to a saddle node bifurcation (as the low voltage solution and the high voltage solution become numerically similar). HELM is founded in complex analysis, and it was first developed in order to overcome these numerical difficulties. Based on how the germ of power series expressions are initialized, HELM will always compute the desired, high voltage power flow solution, and it will never fail to compute this solution if it exists [33]. Since HELM embeds a series of power balance equations into a holomorphic context, it uses a recursive, rather than an iterative, method for solving the power flow problem. No Jacobian matrix is needed to iterate towards a solution, so its speed is comparable to that of fast decoupled power flow methods [40].

Work done in section 5 of [39] provides an important foundation for how HELM can be used to solve for the static stability margins of a power system. In [39], it is shown how the holomorphic parameter s can be extrapolated in order to scale the loads in a system. After generating the holomorphic complex voltage functions, two strategies are introduced which approximately compute the maximum power transfer point of the system. The first, more exact, strategy tracks the mismatch of the known and the computed power injections of the system as s is increased. A bifurcation occurs when the mismatch suddenly becomes numerically significant (the holomorphic equations become invalid). The second strategy computes the zeros of the numerator of the Padé approximant for all of the holomorphic voltage functions. Although less accurate, this strategy is still shown to have less than a 1% error when implemented on a four bus system (assuming a sufficiently large number of recursive terms). This CPF method of increasing s , as introduced in [39], scales all loads at uniform rates, and it does not account for more than one single generator bus (the swing bus) in the system. As will be shown, we have derived a set of holomorphically embedded power balance equations which allow for the insertion of multiple voltage controlled buses and make room for the scaling of individual loads at different loading rates. This allows us to draw the PV nose curve very quickly and to exactly determine the bifurcation point of the system without any iterations or recursions.

1.5 Forward

1.5.1 Thesis Outline

In the preceding sections, we have thoroughly outlined the problems associated with gauging and maintaining Long Term Voltage Stability. In the following two chapters, we leverage our results and conclusions from this chapter in order to present a series of tools and methods for improving the LTVS of a system. In Chapter 4, we present a summary of our results and conclusions. Finally, we end by expressing several ideas for future work on these topics.

1.5.2 Key Innovations

The voltage collapse mitigation efforts of Chapter 3 focus on several key innovations. The first treats the holomorphic parameter s as a slowly varying stochastic variable (random walk) which scales load. Critical loading thresholds, or thresholds which the value of s should not surpass during its random walk, are identified through using an application of first passage processes. Finally, a full order dynamical system model is used to analytically calculate the algebraic variable covariance matrix of the system (given a fast acting stochastic excitation from load noise). Once the controller has taken action, we use a dynamical simulation with fast stochastic noise injections (an Ornstein-Uhlenbeck process) in order to validate the dynamical oscillatory, rotor and voltage stability of the system. We thus couple static algebraic voltage collapse analysis through HELM, first passage probability, statistical estimation (based on analysis of a full order system model) and dynamical simulation in order to develop and validate our controllers.

Chapter 2

Spectral Analysis of the Reduced Power Flow Jacobian

2.1 Introduction

As detailed in Chapter 1, prior research has shown that spectral decomposition of the reduced power flow Jacobian (RPFJ) can yield participation factors that describe the extent to which particular buses contribute to particular spectral components of a power system. Research has also shown that both variance and autocorrelation of time series voltage data tend to increase as a power system with stochastically fluctuating loads approaches certain critical transitions. This chapter presents evidence suggesting that a system’s participation factors predict the relative bus voltage variance values for all nodes in a system. As a result, these participation factors can be used to filter, weight, and combine real time PMU data from various locations dispersed throughout a power network in order to develop coherent measures of global voltage stability. This chapter does not seek to define these metrics; instead, we present a tool (spectral analysis of the RPFJ) which can be used to do so in future work. This paper first describes the method of computing the participation factors. Next, two potential uses of the participation factors are given: (1) predicting the relative bus voltage variance magnitudes, and (2) locating generators at which the autocorrelation of voltage measurements clearly indicate proximity to critical transitions. The methods are tested using both analytical and numerical results from a dynamic model of a 2383-bus test case.¹

¹Material in this chapter is duplicated from *Identifying System-Wide Early Warning Signs of Instability in Stochastic Power Systems* by S. Chevalier and P. Hines. Said paper was published at the 2016 IEEE PES General Meeting.

2.2 Mathematical Methods for Spectral Analysis

This section presents a method for using spectral decomposition of the RPFJ to identify and weight variables that will most clearly show evidence of CSD. (Further information on this spectral decomposition method can be found in).

The standard power flow Jacobian matrix, based on the linearization of steady state power flow equations, is given by (2.1). For an n bus system, we assume this $2n$ by $2n$ matrix has been altered such that it can iteratively solve the Newton-Raphson power flow problem.

$$\begin{bmatrix} \Delta\mathbf{P} \\ \Delta\mathbf{Q} \end{bmatrix} = \begin{bmatrix} J_{\mathbf{P}\theta} & J_{\mathbf{P}\mathbf{V}} \\ J_{\mathbf{Q}\theta} & J_{\mathbf{Q}\mathbf{V}} \end{bmatrix} \begin{bmatrix} \Delta\boldsymbol{\theta} \\ \Delta\mathbf{V} \end{bmatrix} \quad (2.1)$$

In order to perform V-Q sensitivity analysis (an important aspect of voltage stability analysis), we assume that the incremental change in real power $\Delta\mathbf{P}$ is equal to 0. In this way, we can study how incremental changes in injected reactive power affect system voltages. Setting $\Delta\mathbf{P} = \mathbf{0}$ and rearranging terms to remove $\Delta\boldsymbol{\theta}$, the expression for the reduced Jacobian is defined:

$$\Delta\mathbf{Q} = [J_{\mathbf{Q}\mathbf{V}} - J_{\mathbf{Q}\theta} J_{\mathbf{P}\theta}^{-1} J_{\mathbf{P}\mathbf{V}}] \Delta\mathbf{V} = [J_R] \Delta\mathbf{V} \quad (2.2)$$

Assuming we are dealing with a system which has a converging power flow solution (via the Newton-Raphson method), the matrix J_R can be assumed non singular and written as the product of its right eigenvector matrix R , its left eigenvector matrix L , and its diagonal eigenvalue matrix Λ , such that:

$$J_R = R\Lambda L \quad (2.3)$$

The left and right eigenvectors are orthonormalized such that, for the right eigenvector \mathbf{r}_i (column vector) and the left eigenvector \mathbf{l}_j (row vector), the Konecker delta function defines their relationship:

$$\mathbf{l}_j \mathbf{r}_i = \delta_{j,i} = \begin{cases} 1 & i = j \\ 0 & i \neq j \end{cases} \quad (2.4)$$

We begin by decomposing J_R using a simple similarity transform. The transform is substituted into

(2.2):

$$\begin{aligned}
\Delta \mathbf{Q} &= \\
&\left[\begin{array}{cccc} \mathbf{r}_1 & \mathbf{r}_2 & \cdots & \mathbf{r}_n \end{array} \right] \left[\begin{array}{cccc} \lambda_1 & 0 & \cdots & 0 \\ 0 & \lambda_2 & & \vdots \\ \vdots & & \ddots & 0 \\ 0 & \cdots & 0 & \lambda_n \end{array} \right] \left[\begin{array}{c} \mathbf{l}_1 \\ \mathbf{l}_2 \\ \vdots \\ \mathbf{l}_n \end{array} \right] \Delta \mathbf{V} \\
&= \left[\begin{array}{cccc} r_{1,1} & r_{2,1} & \cdots & r_{n,1} \\ r_{1,2} & r_{2,2} & & r_{n,2} \\ \vdots & & \ddots & \vdots \\ r_{1,n} & r_{2,n} & \cdots & r_{n,n} \end{array} \right] \left[\begin{array}{c} \lambda_1(\mathbf{l}_1 \cdot \Delta \mathbf{V}) \\ \lambda_2(\mathbf{l}_2 \cdot \Delta \mathbf{V}) \\ \vdots \\ \lambda_n(\mathbf{l}_n \cdot \Delta \mathbf{V}) \end{array} \right] \tag{2.5}
\end{aligned}$$

It becomes helpful to investigate how changing voltage affects the change in injected reactive power of a single bus (ΔQ_1 for example). This is shown in (2.6).

$$\begin{aligned}
\Delta Q_1 &= r_{1,1}\lambda_1(\mathbf{l}_1 \cdot \Delta \mathbf{V}) + r_{2,1}\lambda_2(\mathbf{l}_2 \cdot \Delta \mathbf{V}) + \\
&\quad \cdots + r_{n,1}\lambda_n(\mathbf{l}_n \cdot \Delta \mathbf{V}) \tag{2.6}
\end{aligned}$$

In order to determine how the reactive power at bus n is affected by the voltage at only bus n , we simply hold all other voltage magnitudes constant. If we choose $n = 1$, the voltage differential vector becomes $\Delta \mathbf{V} = [\Delta V_1 \ 0 \ \cdots \ 0]$. The equation for reactive power differential changes accordingly.

$$\Delta Q_1 = (\lambda_1 r_{1,1} l_{1,1} + \lambda_2 r_{2,1} l_{2,1} + \cdots + \lambda_n r_{n,1} l_{n,1}) \Delta V_1 \tag{2.7}$$

At this point, we can define and incorporate the participation factors. The indices in the following equation refer to the j^{th} row and the i^{th} column of the right eigenvector matrix R and the i^{th} row and the j^{th} column of the left eigenvector matrix L .

$$\rho_{i,j} = R_{j,i} L_{i,j} \tag{2.8}$$

Therefore, $\rho_{i,j}$ defines how j^{th} state is affected by the i^{th} eigenvalue. Clearly, individual reactive power states can be expressed as a superposition of eigenvalues of varying degrees of participation. If we compute the reactive power changes at each bus based on the voltage changes at each

corresponding local bus, we obtain the following set of equations.

$$\Delta Q_1 = (\lambda_1 \rho_{1,1} + \lambda_2 \rho_{2,1} + \cdots + \lambda_n \rho_{n,1}) \Delta V_1$$

$$\Delta Q_2 = (\lambda_1 \rho_{1,2} + \lambda_2 \rho_{2,2} + \cdots + \lambda_n \rho_{n,2}) \Delta V_2$$

⋮

$$\Delta Q_n = (\lambda_1 \rho_{1,n} + \lambda_2 \rho_{2,n} + \cdots + \lambda_n \rho_{n,n}) \Delta V_n$$

In these equations, a reactive power state is expressed as a superposition of eigenvalues. Conversely, we can also express each eigenvalue as a superposition of different states. The reason why such an expression is useful is shown through (2.12). Recognizing that $R = L^{-1}$, the following manipulations may be made.

$$\begin{aligned} \Delta \mathbf{Q} &= \\ \left[\begin{array}{cccc} \mathbf{r}_1 & \mathbf{r}_2 & \cdots & \mathbf{r}_n \end{array} \right] &\left[\begin{array}{cccc} \lambda_1 & 0 & \cdots & 0 \\ 0 & \lambda_2 & & \vdots \\ \vdots & & \ddots & 0 \\ 0 & \cdots & 0 & \lambda_n \end{array} \right] \left[\begin{array}{c} \mathbf{l}_1 \\ \mathbf{l}_2 \\ \vdots \\ \mathbf{l}_n \end{array} \right] \Delta \mathbf{V} \\ \left[\begin{array}{c} \mathbf{l}_1 \\ \mathbf{l}_2 \\ \vdots \\ \mathbf{l}_n \end{array} \right] \Delta \mathbf{Q} &= \left[\begin{array}{cccc} \lambda_1 & 0 & \cdots & 0 \\ 0 & \lambda_2 & & \vdots \\ \vdots & & \ddots & 0 \\ 0 & \cdots & 0 & \lambda_n \end{array} \right] \left[\begin{array}{c} \mathbf{l}_1 \\ \mathbf{l}_2 \\ \vdots \\ \mathbf{l}_n \end{array} \right] \Delta \mathbf{V} \end{aligned}$$

Now, we can isolate a single eigenvalue (λ_1 , for example).

$$\mathbf{l}_1 \Delta \mathbf{Q} = \lambda_1 \mathbf{l}_1 \Delta \mathbf{V} \quad (2.9)$$

$$l_{1,1} \Delta Q_1 + l_{1,2} \Delta Q_2 + \cdots + l_{1,n} \Delta Q_n = \quad (2.10)$$

$$\lambda_1 (l_{1,1} \Delta V_1 + l_{1,2} \Delta V_2 + \cdots + l_{1,n} \Delta V_n)$$

Clearly, the relationship between ΔQ and ΔV for the j^{th} isolated state (holding all else constant)

is given by the following expression.

$$\frac{q_{1,j} \Delta V_j}{q_{1,j} \Delta Q_j} = \frac{\Delta V_j}{\Delta Q_j} = \frac{1}{\lambda_j} \quad (2.11)$$

This is true for all states of a given eigenvalue. Therefore, the spectral component which will have the largest voltage variation for a given reactive power change will have the smallest eigenvalue. For this reason, the participation factors of this eigenvalue will be of great interest to study. The j^{th} eigenvalue can be written as a summation of n unique states. In this way, (2.12) shows how each state participates in the eigenvalue of a system.

$$\lambda_j = \lambda_j \rho_{j,1} + \lambda_j \rho_{j,2} + \cdots + \lambda_j \rho_{j,n} \quad (2.12)$$

There are many different ways to use the eigenvalues and eigenvectors of J_R . For instance, [14] suggest using the smallest eigenvalue of J_R to gauge proximity to bifurcation. Such stability analysis, though, is based solely on the decomposition of a model based static matrix and is highly limited in nature, as outlined by M. Pal in the discussion section of [14]. Instead, we propose that J_R can be leveraged as tool to interpret streams of PMU data. Detecting Critical Slowing Down in time series data is a purely data driven stability assessment, but it can be difficult to understand which nodes will show the strongest EWSs [18]. Therefore, the novel approach outlined in this chapter relies on using static decomposition results to weight and interpret incoming dynamic data.

2.3 Uses of Participation Factors: Experimental Results

This section outlines how the derived participation factors can be used to interpret real time PMU data. The system configuration and load noise assumptions are outlined in 2.3.1. 2.3.2 provides evidence for the participation factor's ability to predict relative variance strengths. Finally, 2.3.3 outlines how participation factors can be used to interpret autocorrelation signals.

2.3.1 Polish Test Case System Overview

In order to test our methods, we used analytically derived data from the 2383-bus dynamic Polish test system. This network contains 327 four-variable synchronous generators. Each generator is equipped with a three-variable turbine governor model for frequency control and a four-variable

exciter model (AVR) for voltage regulation. There are 322 shunt loads (all connected to generator buses) and 1503 active and reactive loads spread throughout the system. In order to push the system towards voltage collapse, we employed a simple uniform loading of all loads (except for those attached to generator buses). This method is justified in [24]. Half of the PQ bus loads are modeled as voltage controlled loads, while the other half are modeled as frequency controlled loads. Parameters controlling the voltage controlled loads are modeled after the Nordic Test System in [3], while parameters controlling the frequency controlled loads are modeled after the 39 bus test system described in [18].

The differential algebraic equations modeling the power system are given by:

$$\dot{\mathbf{x}} = \mathbf{f}(\mathbf{x}, \mathbf{y}) \quad (2.13)$$

$$\mathbf{0} = \mathbf{g}(\mathbf{x}, \mathbf{y}, \mathbf{u}) \quad (2.14)$$

where \mathbf{f} , \mathbf{g} represent the differential and algebraic equations governing the system, \mathbf{x} , \mathbf{y} are the differential and algebraic variables of these equations, and \mathbf{u} represents the stochastic load fluctuations. These load fluctuations \mathbf{u} follow a mean-reverting Ornstein-Uhlenbeck process:

$$\dot{\mathbf{u}} = -E\mathbf{u} + \boldsymbol{\xi} \quad (2.15)$$

where E is a diagonal matrix whose diagonal entries equal the inverse correlation times t_{corr}^{-1} of load fluctuations and $\boldsymbol{\xi}$ is a vector of zero-mean independent Gaussian random variables. A further description of our noise model can be found in Sec. II A of [18]. Also given in [18] is a method for analytically computing the covariance and correlation matrices for all state and algebraic variables. The method is shown to be highly accurate, and we have extended it to the 2383-bus Polish system. After thorough testing, we found the analytically calculated covariance and correlation matrices to be just as accurate on the large Polish system as they were on the small 39 bus system. The data presented in the following two sections use the analytically calculated results (as opposed to repeated, averaged dynamic simulation results).

In order to push the system towards a critical transition (voltage collapse), we set the system loading factor b , ranging from $b = 1$ up to $b = 1.92$. This loading factor would increase all PQ loads by a constant value (active power generation was increased by the same ratio). Voltage collapse would occur when the load factor increased past $b = 1.923$.

The concept of a limit-induced bifurcation is an important topic discussed in [27]. Power system limits, such as reactive power generation limits, are an important aspect of stability analysis, but for the Polish power system model, we have extended all limits such that the system can experience maximum loadability without the occurrence of a Hopf or limit-induced bifurcation. This is certainly a simplification, but it allows us to concentrate on the effects of pure voltage collapse.

2.3.2 Evidence for Bus Voltage Variance Prediction

As indicated by (2.11), the smallest eigenvalue of J_R corresponds to the spectral component which will yield the largest voltage variation for a given reactive power variation. When the participation factors corresponding to the smallest eigenvalue are plotted, they are shown to directly predict the relative bus voltage variance strengths. Fig. 2.1 shows two plots. The top plot corresponds to the participation factors for buses 200 through 500, and the bottom plot shows the true bus voltage variance, derived analytically, for buses 200 through 500. The remaining system buses are left out for the sake of clarity. Despite the fact that the participation factors are completely blind to the dynamics of the system, they are still quite successful at predicting the relative variance strengths.

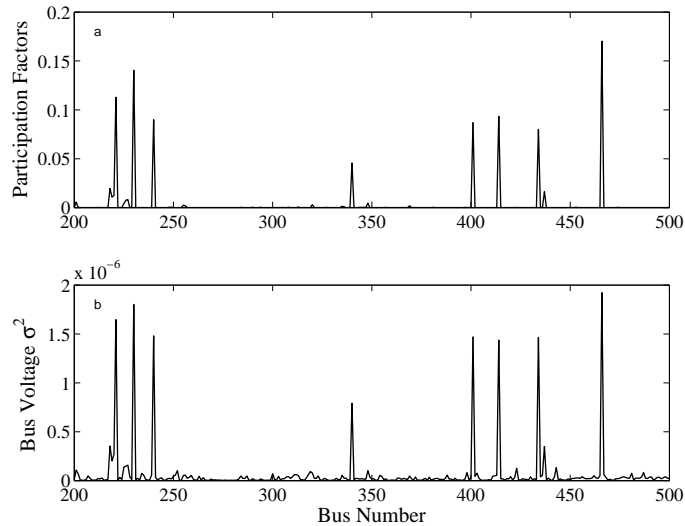


Figure 2.1: Shown are test results for buses 200 through 500 from the loaded 2383 bus system. Bus voltage variances at each node (panel (b)) are shown to have their relative magnitudes directly predicted by the participation factors of the smallest eigenvalue of the RPFJ (panel (a)).

As shown in reference [17], increasing voltage variance is due to buses which are operating lower on the PV curve. Therefore, participation factors of the smallest eigenvalue also identify the node voltages which, as the system is overloaded, begin to diverge away from 1 per unit in magnitude

most rapidly and drift towards 0. These are the nodes which are primarily responsible for non convergent power flow equations. Interestingly, as PQ buses in the system are increasingly loaded, the recalculated participation factors do not change drastically (for a uniform loading condition). This is equivalent to saying that the *spectral components* do not change significantly. This is a useful result, since real power flow models are only updated every few minutes.

As indicated previously, participation factors of the most unstable nodes serve as values indicating the relative bus voltage variance strengths. Therefore, as the system is increasingly loaded, the most unstable nodes will begin to have larger and larger participation factors as their relative variance strengths grow relative to other, more stable nodes. Fig. 2.2 shows an example of this for the 2383 bus system. As the system is loaded, the relative strength of the most unstable bus' participation increases almost linearly, but when the critical transition approaches, the participation begins to climb more steeply.

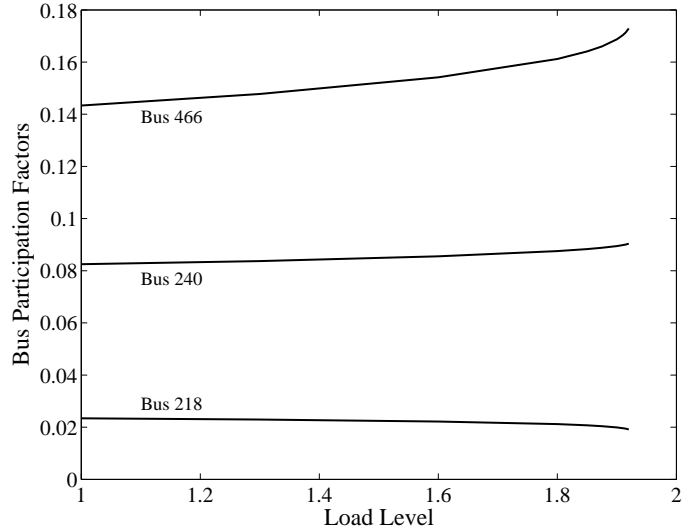


Figure 2.2: Depicted are the evolutions of three different nodal participation factors. As the system is increasingly loaded (right up to bifurcation), bus 466 (the most unstable bus) begins to see a sharp increase in participation to the instability. Bus 240 (the 5th most unstable bus) sees a very slight increase, while bus 218 (the 10th most unstable bus) begins to see a decrease.

2.3.3 Evidence for Locating Generators with Elevated Voltage Autocorrelation

CSD theory predicts that signals from a system approaching a critical transition will begin to show high auto-correlation ($R(\Delta t)$). This can be due to the system's reduced ability to respond to high frequency fluctuations [10], but the system also begins to return to the equilibrium state more slowly after perturbations [19]. In a power system, the system-wide autocorrelation increases are based in the increasingly unstable generator dynamics. These dynamics are driven by the load variances (since this is where the noise is being injected).

In Figure 2.1, there are clearly certain nodes which are experiencing relatively extreme variance increases. Despite the wide ranging indices, these nodes are all in fact separated by only a select few transmission lines. For this reason, the buses with indices between 220 and 466 which are showing the extremely high variance in fact represent a very weak load pocket. The participation factors are therefore very useful for identifying load pockets. Many of the buses connected to this pocket show high variance, and they are therefore driving the autocorrelation of the most proximal generators. By identifying the distance from the center of the load pocket to the closest generators, the autocorrelation of the output signals (voltage and current) of close generators can be scrutinized.

As explained in the caption of Figure 2.3, the traces of the plot represent the average voltage autocorrelation of different groups of generators for varying load levels. The autocorrelation uses a time lag of $\Delta t = 0.2\text{s}$, and the rational for this choice can be found in [19]. As shown in Fig. 2.1, the generators are grouped (and identified) by their proximity to the load pocket. Clearly, the closest generators show the largest average autocorrelation statistics. This is a very useful result.

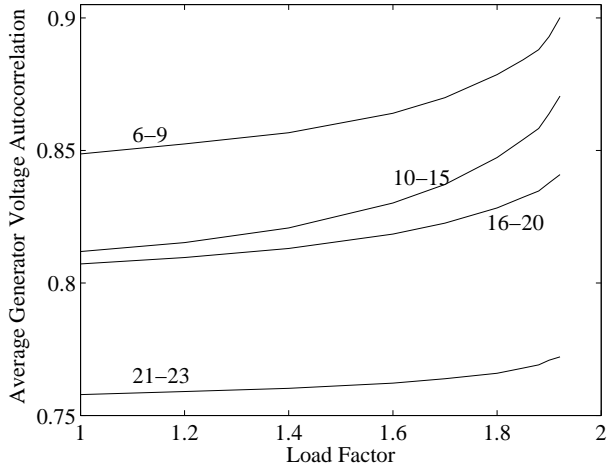


Figure 2.3: The four traces on this plot correspond to the voltage magnitude autocorrelation for different groups of generators over varying load levels. The top trace is all generators that exist between 6 and 9 transmission lines from the load pocket. The second group is all generators that exist between 10 and 15 transmission lines from the load pocket. The third group is all generators that exist between 16 and 20 transmission lines from the load pocket. And the fourth group is all generators that exist between 21 and 23 transmission lines from the load pocket.

2.4 Conclusions

This chapter presents evidence that participation factors from a spectral decomposition of the RPFJ can be used to design methods for combining synchrophasor measurements to produce system-wide indicators of instability in power systems. This method uses model-based information from the power flow Jacobian, which can be updated every few minutes through the SCADA network, along with high sample-rate voltage magnitude measurements, which can be collected from synchronized phasor measurement systems deployed throughout the system. We have shown that this combination of power flow results and dynamic real time data analysis can be used to develop system-wide stability metrics.

Chapter 3

Using PMU Statistics to Reduce the Probability of Voltage Collapse

3.1 Introduction

With the continued deployment of PMUs, high sample rate data is dramatically increasing the real time observability of power grids. As presented in Chapter 1, prior research has shown that information regarding the stability of the network is present in the statistics of this real time data. In this chapter, we show that bus voltage variance can be used as a stability margin control signal in order to reduce the probability of voltage collapse as load builds up. To accomplish this task, we manipulate the Holomorphic Embedded Load Flow Method (HELM) in order to apply it to the Continuation Power Flow (CPF) problem for a fast, analytical way of determining critical loading conditions. We then leverage a low order dynamical system model to compute the algebraic variable covariance matrix of a critically loaded system. Raw statistical data in a highly observable load pocket is monitored and tested against the analytically computed critical variances from the covariance matrix. Thus, we employ a data driven method for determining when the system has reached a stability limit. We then adapt HELM to build a reactive power controller which pushes the stability of the system back to an acceptable stability margin. The following sections present the methods used to build this controller along with the test results from its simulated implementation.

3.2 Analytically Computing the Algebraic Variable Covariance Matrices

To understand when a measured PMU statistic warrants control action, the operator should have some sort of predicted thresholds which should not be passed. This section outlines a method for leveraging a full DAE system model in order to analytically compute threshold statistics.

3.2.1 Power System Model Overview

In order to simulate and study an N bus power system, we rely on the standard generator and power flow DAE models used across industry and academia. Conveniently, these models are outlined in Chapters 17 and 18 of [28]. Based on the conventions presented in these chapters, we rely on a type 4 Synchronous Generator (SG) model, a type 1 Turbine Governor (TG) model, and type 2 Automatic Voltage Regulator (AVR) model. As reviewed in Section 2.3.1, the compact set of DAEs modeling the power systems we are simulating are given by equations (3.1) and (3.2).

$$\dot{\mathbf{x}} = \mathbf{f}(\mathbf{x}, \mathbf{y}) \quad (3.1)$$

$$\mathbf{0} = \mathbf{g}(\mathbf{x}, \mathbf{y}, \mathbf{u}) \quad (3.2)$$

where \mathbf{f} , \mathbf{g} represent the differential and algebraic equations governing the system, \mathbf{x} , \mathbf{y} are the differential and algebraic variables of these equations, and \mathbf{u} represents the stochastic load fluctuations. An overview of the differential and algebraic equations which comprise \mathbf{f} , \mathbf{g} is given in Appendix E.

3.2.2 State Variable Covariance Matrix

The process for deriving the approximate covariance matrix for this system is outlined in [18], but we derive it in more detail here. We begin by linearizing (2.14) using the first two terms of the multivariate Taylor Series Expansion.

$$0 = \mathbf{g}(\mathbf{x}, \mathbf{y}, \mathbf{u}) \Big|_{\mathbf{x}_0, \mathbf{y}_0, \mathbf{u}_0} + \frac{\partial \mathbf{g}}{\partial \mathbf{x}} \Delta \mathbf{x} + \frac{\partial \mathbf{g}}{\partial \mathbf{y}} \Delta \mathbf{y} + \frac{\partial \mathbf{g}}{\partial \mathbf{u}} \Delta \mathbf{u} \quad (3.3)$$

Because we are linearizing about the solution (root), the first term of (3.3) is zero. We can rearrange the expression and solve for $\Delta \mathbf{y}$. For notation's sake, we can also rewrite the partial derivatives with

the shorthand notation of \mathbf{g}_x , \mathbf{g}_y , and \mathbf{g}_u .

$$-\mathbf{g}_y \Delta \mathbf{y} = \mathbf{g}_x \Delta \mathbf{x} + \mathbf{g}_u \Delta \mathbf{u} \quad (3.4)$$

Now, $\Delta \mathbf{y}$ can be solved for explicitly, and the RHS of (3.4) can be written as an inner product.

$$\Delta \mathbf{y} = \begin{bmatrix} & \\ -\mathbf{g}_y^{-1} \mathbf{g}_x & -\mathbf{g}_y^{-1} \mathbf{g}_u \end{bmatrix} \begin{bmatrix} \Delta \mathbf{x} \\ \Delta \mathbf{u} \end{bmatrix} \quad (3.5)$$

We can also linearize (2.13) using the first two terms of the multivariate Taylor Series.

$$\dot{\mathbf{x}} = \mathbf{f}(\mathbf{x}, \mathbf{y}) \Big|_{\mathbf{x}_0, \mathbf{y}_0} + \mathbf{f}_x \Delta \mathbf{x} + \mathbf{f}_y \Delta \mathbf{y} \quad (3.6)$$

We can eliminate $\Delta \mathbf{y}$ by substituting in the expression of (3.5). We can also define $\Delta \dot{\mathbf{x}}$ on the LHS of (3.6) by subtracting $\mathbf{f}(\mathbf{x}, \mathbf{y}) \Big|_{\mathbf{x}_0, \mathbf{y}_0}$ on both sides (this serves as the incremental change of the derivative term).

$$\Delta \dot{\mathbf{x}} = \mathbf{f}_x \Delta \mathbf{x} + \mathbf{f}_y \begin{bmatrix} & \\ -\mathbf{g}_y^{-1} \mathbf{g}_x & -\mathbf{g}_y^{-1} \mathbf{g}_u \end{bmatrix} \begin{bmatrix} \Delta \mathbf{x} \\ \Delta \mathbf{u} \end{bmatrix} = \begin{bmatrix} & \\ \mathbf{f}_x - \mathbf{f}_y \mathbf{g}_y^{-1} \mathbf{g}_x & -\mathbf{f}_y \mathbf{g}_y^{-1} \mathbf{g}_u \end{bmatrix} \begin{bmatrix} \Delta \mathbf{x} \\ \Delta \mathbf{u} \end{bmatrix} \quad (3.7)$$

A similar linearization process can be performed on (2.15).

$$\dot{\mathbf{u}} = (-E \mathbf{u} \Big|_{\mathbf{u}_0} + I_n \boldsymbol{\xi}) + (-E \mathbf{u} + I_n \boldsymbol{\xi})' \Delta \mathbf{u} = (-E \mathbf{u} \Big|_{\mathbf{u}_0} + I_n \boldsymbol{\xi}) - E \Delta \mathbf{u} \quad (3.8)$$

Once again, we can define $\Delta \dot{\mathbf{u}}$ as the change, or sensitivity, of the derivative, and it can be calculated by pulling $E \mathbf{u} \Big|_{\mathbf{u}_0}$ onto the LHS of (3.8). Finally, we arrive at an expression for $\Delta \dot{\mathbf{u}}$.

$$\Delta \dot{\mathbf{u}} = -E \Delta \mathbf{u} + I_n \boldsymbol{\xi} \quad (3.9)$$

We can now combine (3.7) and (3.9) into one single equation which relates the sensitivity of the derivatives to the sensitivity of the original variables.

$$\begin{bmatrix} \Delta \dot{\mathbf{x}} \\ \Delta \dot{\mathbf{u}} \end{bmatrix} = \begin{bmatrix} & \\ \mathbf{f}_x - \mathbf{f}_y \mathbf{g}_y^{-1} \mathbf{g}_x & -\mathbf{f}_y \mathbf{g}_y^{-1} \mathbf{g}_u \\ 0 & -E \end{bmatrix} \begin{bmatrix} \Delta \mathbf{x} \\ \Delta \mathbf{u} \end{bmatrix} + \begin{bmatrix} 0 \\ I_n \end{bmatrix} \boldsymbol{\xi} \quad (3.10)$$

where n is the length of \mathbf{u} . By defining a new variable $\mathbf{z} = \begin{bmatrix} \Delta\mathbf{x} & \Delta\mathbf{u} \end{bmatrix}^\top$ and renaming the matrices, we can further simplify (3.10).

$$\dot{\mathbf{z}} = A\mathbf{z} + B\xi \quad (3.11)$$

The form of (3.11) can be exploited to (iteratively) solve for the covariance matrix of the variables in \mathbf{z} . The Lyapunov equation can be solved, where X is the covariance matrix and A and B are defined in (3.11). This relationship is given in [15].

$$AX + XA^\top + BB^\top = 0 \quad (3.12)$$

↓

$$A\sigma_{\mathbf{z}}^2 + \sigma_{\mathbf{z}}^2 A^\top = -BB^\top \quad (3.13)$$

3.2.3 Algebraic Covariance Matrix

The expression in (3.13) will yield the covariance matrix for \mathbf{z} , but the algebraic covariance matrix is still unknown. In order to analytically solve for $\sigma_{\mathbf{y}}^2$, we must exploit a transformation property of covariance matrices. Consider two vectors \mathbf{v}_1 and \mathbf{v}_2 which are related to each other through the linear transformation defined by matrix \mathbf{T} .

$$\mathbf{v}_2 = \mathbf{T}\mathbf{v}_1$$

If the covariance matrix of \mathbf{v}_1 exists and is known, then the covariance matrix of \mathbf{v}_2 can be computed via (3.14).

$$\sigma_{\mathbf{v}_2} = \mathbf{T}\sigma_{\mathbf{v}_1}\mathbf{T}^\top \quad (3.14)$$

We therefore must use the transformation found in (3.5) in order to transform $\sigma_{\mathbf{z}}^2$ into $\sigma_{\mathbf{y}}^2$.

$$\sigma_{\mathbf{y}}^2 = \begin{bmatrix} -\mathbf{g}_{\mathbf{y}}^{-1}\mathbf{g}_{\mathbf{x}} & -\mathbf{g}_{\mathbf{y}}^{-1}\mathbf{g}_{\mathbf{u}} \end{bmatrix} \sigma_{\mathbf{z}}^2 \begin{bmatrix} -\mathbf{g}_{\mathbf{y}}^{-1}\mathbf{g}_{\mathbf{x}} & -\mathbf{g}_{\mathbf{y}}^{-1}\mathbf{g}_{\mathbf{u}} \end{bmatrix}^\top \quad (3.15)$$

3.2.4 Autocorrelation and Cross-Correlation Matrices

With $\sigma_{\mathbf{z}}^2$ and $\sigma_{\mathbf{y}}^2$ known, equations from [15] can be used to solve for correlations. For instance, the full autocorrelation matrix is given by (3.16).

$$E[\mathbf{z}(t)\mathbf{z}^\top(s)] = e^{-A \cdot |\Delta t|} \sigma_{\mathbf{z}}^2 \quad \Delta t = (t - s) \quad (3.16)$$

By choosing a single variable and dividing by its variance, its normalized autocorrelation function can be calculated.

$$R_{z_i}(\Delta t) = E[\mathbf{z}_i(t)\mathbf{z}_i^\top(s)] / \sigma_{z_i}^2 \quad (3.17)$$

As is done in (3.15), the correlation matrix for \mathbf{z} can be transformed into the correlation matrix from just the algebraic variables.

$$E[\mathbf{y}(t)\mathbf{y}^\top(s)] = \begin{bmatrix} -\mathbf{g}_{\mathbf{y}}^{-1}\mathbf{g}_{\mathbf{x}} & -\mathbf{g}_{\mathbf{y}}^{-1}\mathbf{g}_{\mathbf{u}} \end{bmatrix} E[\mathbf{z}(t)\mathbf{z}^\top(s)] \begin{bmatrix} -\mathbf{g}_{\mathbf{y}}^{-1}\mathbf{g}_{\mathbf{x}} & -\mathbf{g}_{\mathbf{y}}^{-1}\mathbf{g}_{\mathbf{u}} \end{bmatrix}^\top \quad (3.18)$$

3.2.5 Extension to the Line Current Covariance Matrix

Expressions for the covariance of certain algebraic variables are derived in the previous subsection. These include \mathbf{V} and $\boldsymbol{\theta}$, but they do not include $\tilde{\mathbf{I}}$ (current magnitudes and phases). The derivation of the line current covariance matrix is found in Appendix F.

3.2.6 Load Noise Model

In modeling this dynamic power system, the noise applied to the loads is governed by a given by (2.15). For a given base load, we assume stochastic noise is injected into the loads in the following way:

$$\mathbf{P}(t) = \mathbf{P}_0(1 + \mathbf{u}(t)) \quad (3.19)$$

$$\mathbf{Q}(t) = \mathbf{Q}_0(1 + \mathbf{u}(t)) \quad (3.20)$$

where \mathbf{u} is a vector of random load fluctuations. We model these load fluctuations as an Ornstein-Uhlenbeck process (stationary, Gaussian, and Markovian). Since this is a mean reverting Gaussian process, the loads are constantly changing, but over time, the following observation is true:

$$E[\mathbf{P}(t)] = \mathbf{P}_0 \quad (3.21)$$

$$\mathbb{E} [\mathbf{Q}(t)] = \mathbf{Q}_0 \quad (3.22)$$

That is, the expected values of the loads over time remain fixed at the base load value. The derivative (or instantaneous change) in the fluctuations is given below.

$$\dot{\mathbf{u}} = -E\mathbf{u} + I_n \boldsymbol{\xi} \quad (3.23)$$

where I_n is simply the n by n identity matrix and E is a diagonal matrix of inverse time correlations.

$$E = \begin{bmatrix} t_{\text{corr}_1}^{-1} & 0 & \cdots & 0 \\ 0 & t_{\text{corr}_2}^{-1} & & \vdots \\ \vdots & & \ddots & 0 \\ 0 & \cdots & 0 & t_{\text{corr}_n}^{-1} \end{bmatrix} \quad (3.24)$$

We define the inverse time correlations like so: $\gamma = \frac{1}{t_{\text{corr}}}$. Also, $\boldsymbol{\xi}$ is a vector of independent Gaussian random variables. Each individual element ξ_i has the following properties:

$$\mathbb{E} [\xi_i(t)] = 0 \quad (3.25)$$

$$\mathbb{E} [\xi_i(t)\xi_j(s)] = \delta_{ij}\sigma_\xi^2\delta_I(t-s) \quad (3.26)$$

Clearly, each element ξ_i is zero mean, and it is uncorrelated with itself and with all other realizations at all other times. The intensity of the noise is given by the variance value σ_ξ^2 . This can be stated in the following manner:

$$\langle \xi_i(t_1)\xi_i(t_2) \rangle = \sigma_\xi^2\delta(t_1 - t_2) \quad (3.27)$$

Based on these assumptions, we can compute the (non-normalized) auto-correlation of the load fluctuations.

$$\langle u_i(t + \Delta t)u_i(t) \rangle = \frac{\sigma_\xi^2}{2\gamma}e^{-\gamma|\Delta t|} \quad (3.28)$$

If $\Delta t = 0$, the equation directly computes the variance of the load fluctuations.

$$\sigma_u^2 = \frac{\sigma_\xi^2}{2\gamma} \quad (3.29)$$

3.3 Adapting HELM to Solve CPF

As explained in Chapter 1, recent literature has leveraged tools from the field of complex analysis in order to develop non-iterative techniques to solve the power flow problem. As shown in the literature [4, 40, 39, 33], the Holomorphic Embedded Load Flow Method (HELM) accomplishes this task.

Functions of complex variables that are complex differentiable everywhere in a neighborhood around a point are said to be holomorphic about that point. Holomorphic functions can be uniquely expressed using a convergent Taylor series in the neighborhood of the point. (Subramanian 50)

Because of these properties, [42] indicates that a holomorphic function is in fact equal to its own (infinite) Taylor Series. The general process for solving the power flow problem, as outlined by each of these sources, has approximately five basic steps:

1. Embed the power flow (or power balance) equations in the complex plane, where the unknown complex voltages are converted into complex holomorphic functions.
2. Use the germ solution (all generation and loading is set to 0) along with a recursive technique in order to solve for the unknown power series coefficients of the holomorphic functions.
3. Transform the fully characterized holomorphic functions into Padé approximants.
4. Solve for the unknown complex voltage phasors by evaluating the Padé approximants. This is accomplished through setting the holomorphic parameter (which is typically s in the literature) equal to 1 and performing simple algebra.
5. Once the system-wide complex voltages are known, use the standard power flow equations to compute the power injections at each bus.

Although mathematically dense, the process itself is fairly straightforward yet highly rigorous. In order to explain how we manipulate HELM to solve the CPF problem, we first briefly review how the five steps listed above are used to solve the power flow problem. The entire procedure for using HELM to solve power flow is outlined in [39].

3.3.1 Using HELM to Solve the Power Flow Problem

In order to solve the power flow problem, we must develop appropriate power balance equations and then embed them with a complex parameter. We do this below for the PQ bus, the swing bus, and

the PV bus.

3.3.1.1 Load Bus Model

For all load buses in a system with N buses, the active and reactive power injections are known. Therefore, we begin by formulating the complex current injection at these buses.

$$I_i = \sum_{k=1}^N Y_{i,k} V_k \quad i \in \text{PQ} \quad (3.30)$$

We define the relationship between the current phasor, the bus voltage phasor, and the complex power injection as follows.

$$V_i (I_i)^* = S_i \quad \Rightarrow \quad I_i = \left(\frac{S_i}{V_i} \right)^* \quad (3.31)$$

↓

$$I_i = \sum_{k=1}^N Y_{i,k} V_k = \frac{S_i^*}{V_i^*} \quad (3.32)$$

The shunt elements in the diagonal matrix are removed, and a transformed Y bus matrix Y' is defined. We place these shunts into a new matrix Y_S , where the sum of shunts connecting bus i and ground are equal to y_i .

$$Y'_{i,j} = \begin{cases} Y_{i,j} - y_i & i = j \\ Y_{i,j} & i \neq j \end{cases} \quad (3.33)$$

$$Y_{S,i,j} = \begin{cases} y_i & i = j \\ 0 & i \neq j \end{cases} \quad (3.34)$$

Therefore, we can reconstruct the original Y bus matrix with Y' and Y_S .

$$Y = Y' + Y_S \quad (3.35)$$

Now we rewrite the current injection equation.

$$I_i^{\text{inj}} = \sum_{k=1}^N \left(Y'_{ik} V_k \right) + Y_{S,i,i} V_i = \frac{S_i^*}{V_i^*} \quad (3.36)$$

↓

$$\sum_{k=1}^N Y'_{ik} V_k = \frac{S_i^*}{V_i^*} - Y_{S,i,i} V_i \quad (3.37)$$

The voltage functions can now be embedded with a complex parameter s . Notice that the complex conjugate of s is taken in the denominator of 3.38. This is because for a holomorphic function, $(V(s))^* = V^*(s^*)$.

$$\sum_{k=1}^N Y'_{ik} V_k(s) = s \frac{S_i^*}{V_i^*(s^*)} - s Y_S V_i(s) \quad (3.38)$$

In general, we express the voltage $V(s)$ as a function of the complex parameter s according to the following power series.

$$V(s) = V[0] + V[1]s + V[2]s^2 + V[3]s^3 + \dots = \sum_{n=0}^{\infty} V[n] (s^n) \quad (3.39)$$

The coefficients $V[n]$ are undetermined complex numbers. In (3.38), if $s = 1$ is applied, we obtain the desired current injection equations. If $s = 0$, no load and no shunts are applied in the system, so the solution is trivial. This is known as the “germ” solution.

3.3.1.2 Swing Bus Model

At the swing bus generator, the voltage is held constant, and the phase is used as a reference.

$$V_r = V_r e^{j0}$$

The complex power injection is a free variable. We transform the swing bus voltage equation into a holomorphic function.

$$V_r(s) = 1 + (V_r - 1) s$$

3.3.1.3 Generator Bus Model

In [39], Subramanian introduces two models for generator buses (model I and model II), but both models are based in the same equations and yield virtually identical results. Therefore, only model I is presented below. We start by stating the complex power injection equation.

$$S_i = V_i I_i^* = V_i \sum_{k=1}^N Y_{i,k}^* V_k^* \quad (3.40)$$

At PV buses, the reactive power injection and the phase angle are both unknown. The voltage of the generator and the real power injection are both known though.

$$P_i = \Re(S_i) = \Re \left(V_i \sum_{k=1}^N Y_{i,k}^* V_k^* \right) \quad i \in \text{PV} \quad (3.41)$$

$$|V_i| = V_i^{\text{sp}} \quad i \in \text{PV} \quad (3.42)$$

We now rewrite the current injection equation with embedded complex parameter s :

$$\sum_{k=1}^N Y'_{i,k} V_k(s) = \frac{sP_i - jQ_i(s)}{V_i^*(s^*)} - sY_{S,i} V_i(s) \quad (3.43)$$

Of course, for a PV bus, $Q_i(s)$ is an additional (unknown) free variable. This variable is ultimately constrained by the set point voltage of the bus. The PV bus voltage can be embedded in the parameter s via the following chosen convention:

$$V_i(s)V_i^*(s^*) = 1 + s(|V_i^{\text{sp}}|^2 - 1) \quad (3.44)$$

At $s = 1$, we have simply the following.

$$V_i(1)V_i^*(1) = |V_i^{\text{sp}}|^2 \quad (3.45)$$

3.3.1.4 Model Summary

We have now formulated all necessary equations. Table 3.1 presents a summary. A similar version of this table may be found in [39].

	Original Power Flow Equations	Embedded Equations
$i \in \text{PQ}$	$\sum_{k=1}^N Y_{i,k} V_k = \frac{S_i^*}{V_i^*}$	$\sum_{k=1}^N Y'_{i,k} V_k(s) = s \frac{S_i^*}{V_i^*(s^*)} - sY_S V_i(s)$
$i \in \text{r}$	$V_i = V_r e^{j\theta}$	$V_r(s) = 1 + (V_r - 1)s$
$i \in \text{PV}$	$P_i = \Re \left(V_i \sum_{k=1}^N Y_{i,k}^* V_k^* \right)$ $ V_i = V_i^{\text{sp}}$	$\sum_{k=1}^N Y'_{i,k} V_k(s) = \frac{sP_i - jQ_i(s)}{V_i^*(s^*)} - sY_{S,i} V_i(s)$ $V_i(s)V_i^*(s^*) = 1 + s(V_i^{\text{sp}} ^2 - 1)$

Table 3.1: HELM Model Summary

3.3.1.5 Using the Derived Model to Solve Power Flow

The method for iteratively computing the unknown power series coefficients, which involves splitting each holomorphic function into real and imaginary parts, shall not be reproduced here, as it is dense and can be found in the literature. A similar method, which solves the CPF problem, shall be presented below.

At each bus i , once a sufficient (based on error tolerance) number of power series coefficients are known, $V_i(s) = \Re\{V_i(s)\} + j\Im\{V_i(s)\}$ can be quantified. Next, the holomorphic function at each bus can be converted into a Padé approximant. A Padé approximant is way for rationally approximating (by way of a rational function) a power series. If the Padé approximants converge at $s = 1$, then the system has a valid, high voltage solution. If they do not converge for any bus (all buses should diverge simultaneously), then the system is beyond the point of MPTP or the voltage collapse condition [40]. Assuming we have solved for N_c power series coefficients, we generate $A[n]$ and $B[n]$ in (3.46) to approximate the power series function. Although not necessary, we stipulate that N_c must be odd.

$$\sum_{n=0}^{N_c-1} V[n](s^n) = \frac{\sum_{n=0}^{\frac{N_c-1}{2}} A[n](s^n)}{\sum_{n=0}^{\frac{N_c-1}{2}} B[n](s^n)}, \quad N_c \text{ odd} \quad (3.46)$$

There are a variety of methods for determining the Padé approximants, as outlined in [39]. One of the most common methods is the so called direct (or matrix) method, and it was originally developed by Henri Padé. In order to show how to utilize this method, we explicitly show how it is developed. Initially, we multiply (3.46) by the denominator on the RHS. Again, we assume that $N_c > 1$ is odd.

$$\begin{aligned} & \left[B[0] + B[1]s + \cdots + B[\frac{N_c-1}{2}-1]s^{\frac{N_c-1}{2}-1} + B[\frac{N_c-1}{2}]s^{\frac{N_c-1}{2}} \right] \times \\ & [V[0] + V[1]s + \cdots + V[N_c-2]s^{N_c-2} + V[N_c-1]s^{N_c-1}] \\ & = A[0] + A[1]s + \cdots + A[\frac{N_c-1}{2}]s^{\frac{N_c-1}{2}} \end{aligned} \quad (3.47)$$

Next, we multiply the expression out and group coefficients attached to like values of $s^{\frac{N_c-1}{2}+1}$ to

s^{N_c-1} , as the coefficients attached to these power of s are equal to 0 on the RHS of (3.47).

$$\begin{aligned} B\left[\frac{N_c-1}{2}\right]V[1] + \cdots + B[1]V\left[\frac{N_c-1}{2}\right] + B[0]V\left[\frac{N_c-1}{2} + 1\right] &= 0 \\ \vdots &= \vdots \\ B\left[\frac{N_c-1}{2}\right]V\left[\frac{N_c-1}{2}\right] + \cdots + B[1]V[N_c - 2] + B[0]V[N_c - 1] &= 0 \end{aligned}$$

We have thus formulated a linear system of equations. There are a multitude of solutions to this problem, as it is formulated, so we choose to fix $B[0] = 1$. Now we have a linear system equation $Ax = b$ which may be solved by inverting matrix A .

$$\begin{bmatrix} V[1] & \cdots & V\left[\frac{N_c-1}{2}\right] \\ \vdots & \ddots & \vdots \\ V\left[\frac{N_c-1}{2}\right] & \cdots & V[N_c - 2] \end{bmatrix} \begin{bmatrix} B\left[\frac{N_c-1}{2}\right] \\ \vdots \\ B[1] \end{bmatrix} = \begin{bmatrix} V\left[\frac{N_c-1}{2} + 1\right] \\ \vdots \\ V[N_c - 1] \end{bmatrix} \quad (3.48)$$

\Downarrow

$$\begin{bmatrix} B\left[\frac{N_c-1}{2}\right] \\ \vdots \\ B[1] \end{bmatrix} = \begin{bmatrix} V[1] & \cdots & V\left[\frac{N_c-1}{2}\right] \\ \vdots & \ddots & \vdots \\ V\left[\frac{N_c-1}{2}\right] & \cdots & V[N_c - 2] \end{bmatrix}^{-1} \begin{bmatrix} V\left[\frac{N_c-1}{2} + 1\right] \\ \vdots \\ V[N_c - 1] \end{bmatrix} \quad (3.49)$$

Once this has been done, $B[1]$ through $B\left[\frac{N_c-1}{2}\right]$ are known. Solving for coefficients $A[0]$ through $A\left[\frac{N_c-1}{2}\right]$ is then trivial.

$$A[n] = \sum_{k=0}^n V[k]B[n-k] \quad (3.50)$$

The phasor voltage at bus i can then be calculated by evaluating the approximant at $s = 1$.

$$\tilde{V}_i = \frac{\sum_{n=0}^{\frac{N_c-1}{2}} A[n](s^n)}{\sum_{n=0}^{\frac{N_c-1}{2}} B[n](s^n)}|_{s=1} \quad (3.51)$$

Using the power flow equations of (1.16) and (1.17) then lets us calculate the complex power injections and fully solve the power flow problem. This concludes the overview of the five step process presented at the beginning of this section.

3.3.2 CPF via HELM

3.3.2.1 Using the Holomorphic Parameter s to Scale Loads

In [39], a method for scaling loads by increasing the holomorphic parameter s is introduced. As loads are scaled, the holomorphic functions directly compute the complex bus voltages at all buses in the system. Indeed, this is an extremely fast way to perform CPF and draw the nose curves for the system. In order to implement this method, the method for solving the base case power flow is no different than the method presented above, and only minor manipulations are made to the equations in Table 3.1. As it stands, though, the method has two major drawbacks. First, it scales all loads in the system uniformly (at the same rate). Loads cannot decrease, remain static or increase at variable rates. Second, the method does not account for multiple generator buses. As presented, the method relies on a single generator (swing) bus which is powering the entire system.

In order to solve these problems, we derive a new method for scaling loads from some base case solution. It allows for variable scaling rates in any (or no) direction, and it allows from multiple generators to be dispersed throughout the system. As loading (and losses) increase, generator active and reactive power injections must change too. In the conventional CPF problem, generation rates (or participation factors) are assigned to different generators to pick up excess load. This is not the approach we took. For mathematical simplicity, we instead solve the base case power flow solution and then fix the generator voltage phase angle. In this way, the complex voltage of the generator is fully characterized. As load increases at the load buses, the generators respond in the following way: generation increases quasi-proportionally to the “electrical distance” between the generator and the load. Electrically proximal generators respond with the most power generation increase while electrically distant generators respond with much smaller power generation increases. Although this is an undesirable assumption for a variety of CPF uses, our main focus of this chapter is to track the voltage statistics of a small load pocket with poor LTVS. In this situation, the power is fed from generators outside of the load pocket. If the rest of the system is voltage stable, we hypothesize that where the power is generated has a very small impact on the point of voltage collapse for an isolated load pocket. This shall be discussed further below. For discussion on adding generator participation factors into this problem, see the future work section of Chapter 4.

We now derive how this method may be implemented, which we refer to as “**CPF via HELM**”¹.

We start by noting that either the method presented above or the traditional Newton-Raphson

¹Much of the following derivation is novel, while some pieces have been borrowed from Chapter 4 of [39]

technique must be used to solve for the base case power flow solution. It does not matter which method is used to solve for the base case, since they will compute the same solution (assuming we are sufficiently far from a SN bifurcation).

3.3.2.2 CPF via HELM: PV and Swing Bus Model

The holomorphic voltage functions at the swing bus and at the generator buses are not a function of the holomorphic parameter s . We assume these voltages remain constant regardless of load increase. Because of this assumption, we clearly are not considering reactive power limitations on generators. For discussion on generator reactive power limitations, see the discussion in the future work section of Chapter 4. Table 3.2 summarizes the chosen embedded equations.

	Original Power Flow Equations	Embedded Equations
$i \in r$	$V_i = V_r e^{j\theta}$	$V_r(s) = V_r$
$i \in PV$	$P_i = \Re \left(V_i \sum_{k=1}^N Y_{i,k}^* V_k^* \right)$ $ V_i = V_i^{\text{sp}}$	$V_i(s) = V_i e^{j\theta_i}$

Table 3.2: PV and Swing Bus Model Summary for CPF Application

Since the phasor voltages at these buses are constant and known, we can define the power series coefficients directly.

$$V_i(s) = \begin{cases} V_i[n] &= V_i e^{j\theta_i} & n = 0 \\ V_i[n] &= 0 & n > 0 \end{cases} \quad i \in \{PV \cup r\} \quad (3.52)$$

3.3.2.3 CPF via HELM: PQ Bus Model

We now set out to alter the PQ bus equations given in 3.1 in the following way: loading rates are added to each load such that HELM can handle loads which increase at variable rates. Also, we use the Y bus matrix Y and disregard Y' and Y_S . These matrices are useful for determining the germ solution of the system which is necessary to solve power flow, but we assume we already have the base case power flow solution (in one way or another).

$$\sum_{k=1}^N Y_{i,k} V_k(s) = \frac{S_i^* + s k_i S_i^*}{V_i^*(s^*)} \quad i \in PQ \quad (3.53)$$

In this case, the parameter k_i is a loading rate parameter, and it can be positive, negative, or 0. It corresponds to the rate at which a bus will be loaded. If $k_i = 0$, the i^{th} load buses will not change its loading at all throughout the CPF. It would be trivial to add a second loading rate parameter in order to scale the active and reactive power components of the load separately, but we focus on the constant power factor case here. The other non-zero values of k are relative, specifying how quickly loads change relative to one another. The method of solving for the n^{th} unknown bus voltage power series coefficients is outlined in Appendix G.

3.3.2.4 Choosing the Number of Recursive Routines N_c

When choosing the number of recursive routines necessary to develop an accurate power series expression, two considerations must be made. The first is the accuracy of the power series. In general, as more terms are added to the power series, the holomorphic voltage function of (3.39) becomes more accurate. This, in theory, drives the mismatch vector to 0 as N_c increases.

$$\text{PQ Bus Mismatch Vector} \Rightarrow \begin{bmatrix} \Delta P_i \\ \Delta Q_i \end{bmatrix} = \begin{bmatrix} \left| P_i - V_i \sum_{k=1}^N V_k [G_{ik} \cos(\theta_{ik}) + B_{ik} \sin(\theta_{ik})] \right| \\ \left| Q_i - V_i \sum_{k=1}^N V_k [G_{ik} \sin(\theta_{ik}) - B_{ik} \cos(\theta_{ik})] \right| \end{bmatrix} \quad i \in \text{PQ}$$

As noted in [39] though, as the number of power series terms increase, the condition of the matrix in (3.48), the so called Padé matrix, begins to increase (especially if the higher order power series terms are tending towards 0). This matrix must be inverted in order to solve for the Padé approximants, so the accuracy of these approximants decreases as the condition of the Padé matrix increases. Therefore, when choosing the value of N_c , there is a tradeoff between power series accuracy and Padé matrix condition which must be considered.

3.3.2.5 Using a Holomorphic Function to Solve for a Critical Voltage

Now that the Continuation Power Flow method has been derived using HELM, the holomorphic functions can be used to predict the loading levels which will yield some critically low voltage (or any desired voltage) V_c . This useful derivation is given in Appendix H.

3.3.2.6 Using CPF via HELM to Estimate Voltage Collapse Loading Conditions

After using (4.89) to solve for the holomorphic bus voltage functions (with a sufficiently high number of power series terms), we can use the functions to directly calculate the system's point of fold bifurcation with a small degree of error (for a given loading scheme and loading rates). The functions are implicitly embedded with the knowledge of when the system reaches voltage collapse, so we can exploit this fact in order to determine the loading margin. We start by rewriting the factorized numerator.

$$\sum_{n=0}^{\frac{N-1}{2}} A[n] (s^n) = \prod_{n=0}^{\frac{N-1}{2}} (s - r_1) \quad (3.54)$$

It can be shown that the system will approximately diverge when s reaches the smallest, positive root of the numerator. We use this fact to estimate the loading margin of the system. Because the roots are often complex (with $\Re(r_1) \gg \Im(r_1)$), there is a small amount of error associated with this method. As the system approaches the bifurcation, though, the magnitude of this error shrinks considerably.

3.3.2.7 Testing CPF via HELM on the IEEE 39 Bus System

In order to validate the CPF via HELM method derived above, we consider the IEEE 39 Bus Test System shown in Figure (3.1).

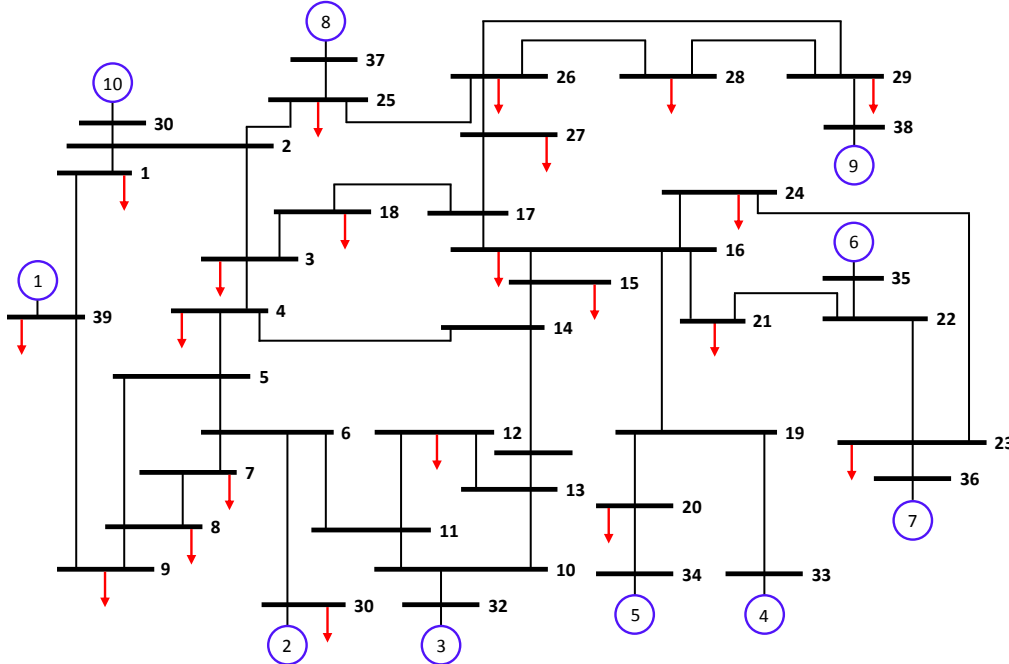


Figure 3.1: Topology of the IEEE 39 Bus System

We define the vector \mathbf{k} which is length 39. The elements of this vector contain the respective loading rates of the buses in the system. We set all elements of this vector equal to 0, except we give the load at buses 3, 4, 7, and 8 a loading rate of 1, and we give the load at bus 20 a loading rate of -0.2. These buses and rates are chosen simply to present a graphically clear example.

$$\mathbf{k}_i = \begin{cases} 1 & i \in \{3, 4, 7, 8\} \\ -0.2 & i = 20 \\ 0 & \text{otherwise} \end{cases} \quad (3.55)$$

As a reminder, the loads of the system scale in the following way, where S_i^0 is the base load at bus i .

$$S_i = S_i^0 + s\mathbf{k}_i S_i^0 \quad (3.56)$$

Accordingly, we run a base case power flow on the system, and then we calculate the bifurcation point based on (3.54). When $s \approx 2$, the system collapses. This corresponds to the loads at buses 3, 4, 7, and 8 tripling while the load at bus 20 reduces by 20%. All other loads remain static. In this example, we scale the holomorphic parameter s from 0 to 1.95 (just before voltage collapse) and compute the complex voltages of the system using (3.46). The voltage magnitudes of the system

are presented in Figure 3.2.

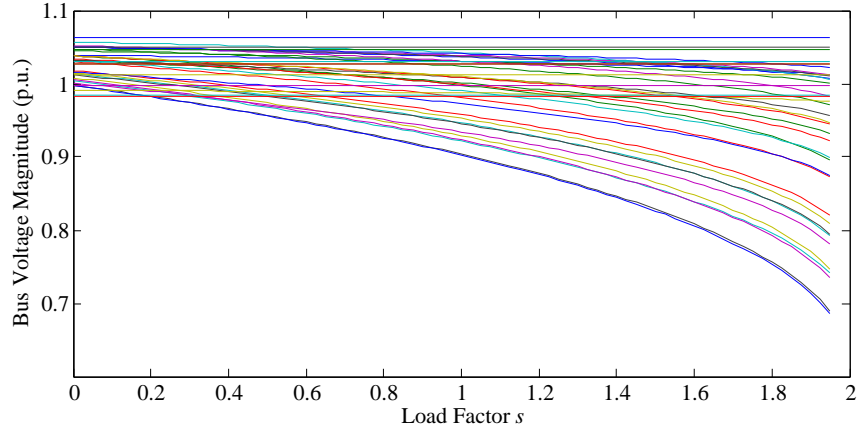


Figure 3.2: Bus Voltage Magnitudes of the 39 Bus System as Computed by (3.46). Clearly, the system is very close to reaching a state of static voltage collapse.

In order to visualize how loading rates affect the system as load is scaled, the active and reactive power injection of the system, for each value of s , is plotted. These results are shown in Figure (3.3). These injections are computed by the power flow equations (1.16) and (1.17) once (3.46) has been used to solve for the complex voltages. In other words, these injections are purely based on calculated voltage phasors and not on (3.56).

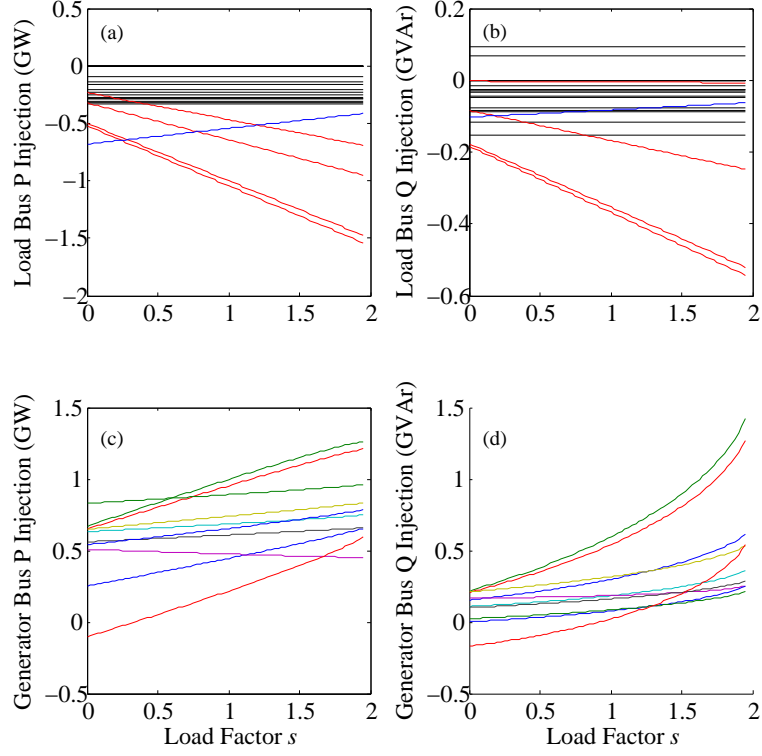


Figure 3.3: Complex Power Injections for load and generator buses of the 39 bus system. In panels (a) and (b), the black traces are the static loads ($\mathbf{k}_i = 0$), the red traces have a loading rate of 1, and the blue trace has a loading rate of -0.2. In panels (c) and (d), the generator injections are shown. Some of these injections are negative initially because many of the generator buses also have load which must be served. In panel (c), the purple trace is seen dropping as the loads are scaled. This is because this trace corresponds to the generator at bus 34. This bus is tied directly to the load at bus 20 which decreases as s increases.

In order to validate the results of Figure 3.3, we test HELM against Newton Raphson Power Flow.

The best way to do so is by following these steps.

1. Compute the holomorphic voltage functions at each load bus and generate the Padé approximants.
2. Increment s and solve for the system-wide complex voltages.
3. Use the power flow equations to compute the injections at each bus.
4. Alter the 39 bus system loading according to (3.56) and alter the generation schedule to match the power injections computed by HELM in step 3.
5. Run NRPF on the updated system and then use the power flow equations to calculate power injections at each bus.

6. Compare HELM and NRPF injection results.

The results of this process are presented in Figure (3.4). For each value of s , the absolute value of the complex power injection differences (as computed by HELM and as computed by NRPF) are plotted.

$$\Delta P_i = |P_i^{\text{HELM}} - P_i^{\text{NRPF}}| \quad (3.57)$$

$$\Delta Q_i = |Q_i^{\text{HELM}} - Q_i^{\text{NRPF}}| \quad (3.58)$$

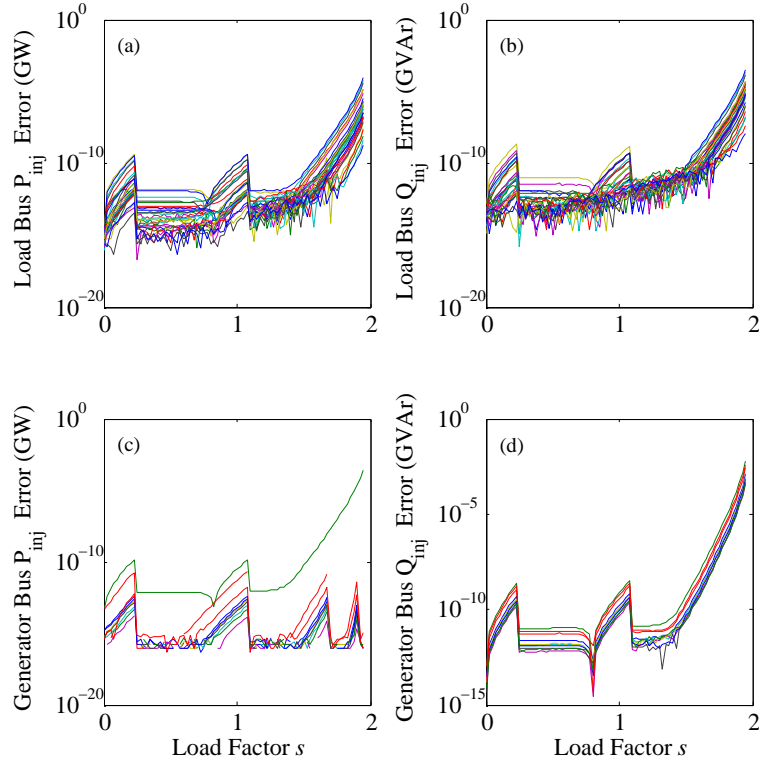


Figure 3.4: 39 Bus System Complex Power Injection Error as computed by (3.57) and (3.58). In each panel, the error is given in log scale. Much of the oscillatory behavior of the error is due to mismatch tolerance is PSAT (the toolbox which is being used for these simulations): if the infinity norm of the mismatch vector is too large, an extra NR iteration is required, ultimately driving down the error between HELM and NRPF. As the system approaches bifurcation, the error becomes numerically significant.

This method was also tested in the 2383 bus Polish power system, and findings were very similar. Based on these results, we conclude that the CPF via HELM method is able to very accurately compute load bus phasor voltages for a given level of load increase. Moving forward, we take three assumptions for granted (for a given system with a given set of loading rates).

1. CPF via HELM is a valid method for determining how voltage phasors in system change as load increases.
2. Equation (4.97) is a valid method for analytically computing what sort of load level is necessary in order for a particular bus to reach a particular voltage magnitude.
3. Equation (3.54) is a valid method for determining the load level which will cause a system to reach static voltage collapse.

3.4 Defining a Probabilistic Loading Margin Based on Escape Probability

Let us assume that the base complex power load at bus i is S_i^0 . When CPF is performed with HELM, the value s_c is the voltage collapse loading parameter (it will be applied to all buses) and k_i is the normalized rate at which the load is increasing. Therefore, S_i^c is the load at bus i associated with system-wide voltage collapse. For a two bus system (generator and load), we have the following expression:

$$S_i^c = S_i^0 + s_c k_i S_i^0$$

For the base loading condition, we have that $s = 0$, and for the collapse condition, we have that $s = s_c$. Therefore, for each plausible loading scheme, we want to determine the probability that s could increase to a level such that it violates s_c . In order to do this, we must model how the load increase might occur over a time frame of several minutes.

3.4.1 Employing the Ornstein-Uhlenbeck Process to Model $s(t)$

We would now like to model the load factor $s(t)$ using an Ornstein-Uhlenbeck process. We assume that $s(t)$ increases from a base level which it continually reverts to (over a short period of time).

$$s(t) = s_0(1 + u(t)) \quad (3.59)$$

where $u(t)$ is a random fluctuation. We model this load fluctuation in the same way as we model the load noise: as an Ornstein-Uhlenbeck process (stationary, Gaussian, and Markovian). Since this is a mean reverting Gaussian process, the loads are constantly changing, but over time, the following observation is true:

$$\mathbb{E}[s(t)] = s_0 \quad (3.60)$$

That is, the expected values of the loads over time remain fixed at the base load value. The derivative (or instantaneous change) in the fluctuations is given below.

$$\dot{u}(t) = -\frac{u(t)}{t_{\text{corr}}} + \xi \quad (3.61)$$

We define the inverse time correlation like so: $\gamma = \frac{1}{t_{\text{corr}}}$. The variable ξ is an independent Gaussian random variable with the following properties.

$$\mathbb{E}[\xi(t)] = 0 \quad (3.62)$$

$$\mathbb{E}[\xi_i(t)\xi_i(s)] = \sigma_\xi^2 \delta_I(t-s) \quad (3.63)$$

Clearly, ξ is zero mean, and it is uncorrelated with itself at all times. The intensity of the noise is given by the variance value σ_ξ^2 . Based on these assumptions, we can compute the (non-normalized) auto-correlation of the load fluctuation.

$$\langle u(t + \Delta t)u(t) \rangle = \frac{\sigma_\xi^2}{2\gamma} e^{-\gamma|\Delta t|} \quad (3.64)$$

If $\Delta t = 0$, the equation directly computes the variance of the load fluctuations.

$$\sigma_u^2 = \frac{\sigma_\xi^2}{2\gamma} \quad (3.65)$$

In order to computationally generate ξ values, we can use MATLAB's "randn" function. This command pulls data points from a zero-mean Gaussian distribution which has a variance (and standard deviation) of 1. The standard deviation of the noise can be found by rearranging the equation for load fluctuation variance and taking the square root of both sides.

$$\sigma_\xi = \sqrt{2\gamma}\sigma_u \quad (3.66)$$

If we model this process via time domain simulation and we extend time to infinity, then we can model the probability density function of the Ornstein-Uhlenbeck process [43].

$$f_u(s) = \sqrt{\frac{\gamma}{\pi\sigma_\xi^2}} e^{-\frac{\gamma(s-s_0)^2}{\sigma_\xi^2}} \quad (3.67)$$

Therefore, we can also compute the CDF:

$$\begin{aligned} F_u(s) &= \frac{1}{2} \left[1 + \operatorname{erf} \left(\frac{s - s_0}{\sqrt{2}\sqrt{\frac{\sigma_\xi^2}{2\gamma}}} \right) \right] \\ &= \frac{1}{2} \left[1 + \operatorname{erf} \left(\frac{s - s_0}{\frac{\sigma_\xi}{\sqrt{\gamma}}} \right) \right] \end{aligned} \quad (3.68)$$

Therefore, for a given noise standard deviation and a time correlation parameter, we can compute the amount of probability that corresponds to $s(t)$ exceeding s_c .

$$P(s \geq s_c) = F_u(s_c) = \frac{1}{2} \left[1 + \operatorname{erf} \left(\frac{s - s_0}{\frac{\sigma_\xi}{\sqrt{\gamma}}} \right) \right] \quad (3.69)$$

3.4.2 Survival Probability

Employing this process is helpful for determining the long term ($t \rightarrow \infty$) distribution of $s(t)$, but we must remember that s_c is a critical threshold. If it is surpassed, the system catastrophically fails. Therefore, the area of the PDF exceeding s_c in the CDF given by (3.69) is meaningless. In order to rigorously compute the probability that a load will increase beyond a threshold during a given time period, we must consider the survival probability of the system. The problem may also be formulated by asking the following question: if a system is performing a random walk, what is the time to the first-passage of a particular threshold? Such considerations are rigorously outlined in [34].

We start by considering a particle which has full range of motion. This particle performs a Gaussian Random Walk with each step, and its mean position is x_0 . We model its concentration with the following Gaussian distribution. It is both a function of position x and the amount of time t for which the random walk occurs.

$$c(x, t) = \frac{1}{\sqrt{4\pi Dt}} e^{-\frac{(x-x_0)^2}{4Dt}} \quad (3.70)$$

The distribution answers the following question: for a given amount of time t , what is the concentration of the amount of time spent at position x ? The distribution depends of the diffusion coefficient parameter D . The diffusion coefficient can be defined statistically in the following way.

$$D = \frac{(\Delta x)^2}{2(\Delta t)} = \frac{\sigma_x^2}{2(\Delta t)} \quad (3.71)$$

This may be interpreted as the rate at which the variance changes over different time intervals². We now consider the situation where we encounter a so called “absorbing boundary condition”. In this situation, if the particle reaches this boundary, it is absorbed and the system fails. We place this boundary at the origin.

$$c(x=0, t) = 0 \quad (3.72)$$

The particle’s concentration at the origin, and anything beyond this point, is 0. In order to solve for the particle’s new distribution, we employ the following trick proposed in [34]: if the particle in question has mean position x_0 , then we place a second (image) particle at $-x_0$. We model both concentrations below, where c_p is the original particle, and c_i is the image particle.

$$c_p(x, t) = \frac{1}{\sqrt{4\pi Dt}} e^{-\frac{(x-x_0)^2}{4Dt}} \quad (3.73)$$

$$c_i(x, t) = \frac{1}{\sqrt{4\pi Dt}} e^{-\frac{(x+x_0)^2}{4Dt}} \quad (3.74)$$

Taking the difference of these two distributions will yield the (un-normalized) distribution of the original particle given the boundary condition of (3.72).

$$c_b(x, t) = \frac{1}{\sqrt{4\pi Dt}} \left[e^{-\frac{(x-x_0)^2}{4Dt}} - e^{-\frac{(x+x_0)^2}{4Dt}} \right] \quad x \geq 0 \quad (3.75)$$

²For instance, a small time interval will have a small diffusion since the distribution will necessarily be tighter. Longer time intervals will have larger diffusion (up to a limit), as the distribution will be more spread out.

As presented in [34], we may make a small approximation to the expression $c_b(x, t)$ and then compute the first passage probability. The algebraic approximation is as follows:

$$e^{\frac{xx_0}{2Dt}} - e^{-\frac{xx_0}{2Dt}} \approx \frac{xx_0}{Dt} \quad (3.76)$$

This is a strong assumption for $xx_0 < Dt$. In other words, the derived survival probability will have a lower and lower validity as probability of survival decreases. Employing this probability, we can compute $F(0, t)$: the first passage probability (with respect to the origin). It is simply the positive derivative of the concentration distribution c_b at the origin times D . Computing this derivative analytically requires the appropriation made above.

$$F(0, t) = \left| D \frac{\partial c_b(x, t)}{\partial t} \right|_{x=0} = \frac{1}{\sqrt{4\pi Dt^3}} e^{-\frac{x_0^2}{4Dt}} \quad (3.77)$$

If we integrate this probability up to a particular time, we compute the probability that the threshold will be exceeded. Of course, if time is extended to infinity, the probability converges to one.

$$\int_0^t F(0, t') dt' = 1 \quad t \rightarrow \infty \quad (3.78)$$

Intuitively, the survival probability, $S(t)$, is one minus the integral of the first passage probability.

$$\begin{aligned} S(t) &= 1 - \int_0^t F(0, t') dt' = 1 \quad t \rightarrow \infty \\ &= \text{erf}\left(\frac{x_0}{\sqrt{4Dt}}\right) \end{aligned} \quad (3.79)$$

Where erf is the error function, D is the diffusion parameter, x_0 is the origin of the particle, and t is the desired time elapsed. This function assumes the threshold is placed at the origin, $x = 0$ and that the particle's original position is somewhere to the right of the origin $x_0 > 0$.

3.4.3 Modeling the Diffusion Coefficient for Consistent Stability Margin Calculations

In order to achieve consistent stability margin calculations, we must consider how the load factors change as load increases. For example, assume we are dealing with a system which has a load pocket with an aggregate apparent power load of S_0 . We then say that the likelihood of load increasing or

decreasing from S_0 over t minutes is directly related to the diffusion coefficient D . We scale all the loads in the system such that the aggregate apparent power loading increases from S_0 to $S_0 + s_c S_0$. We define the following aggregate apparent power collapse loading.

$$S_c = S_0 + s_c S_0 \quad (3.80)$$

As an aside, we note that scaling apparent power and scaling complex power is mathematically equivalent (assuming a positive load increase and lagging power factors).

$$\tilde{S}_c = \tilde{S}_0 + s_c \tilde{S}_0 \quad \Rightarrow \quad |\tilde{S}_c| = S_c \quad (3.81)$$

We may now compute the survival probability (which is a function of the distance between the operating point and s_c).

$$\begin{aligned} S(t) &= \operatorname{erf}\left(\frac{|s_c - s_0|}{\sqrt{4Dt}}\right) \\ &= \operatorname{erf}\left(\frac{s_c}{\sqrt{4Dt}}\right) \end{aligned} \quad (3.82)$$

Assume now that the load increases from S_0 to $S_0 + s_i S_0$. This will not change the aggregate apparent power collapse loading condition. The system is simply closer to a collapse condition.

$$S_c = S_0 + s_i S_0 + (s_c - s_i) S_0 \quad (3.83)$$

In order to determine the new survival probability, we again look at the distance between the operating point and s_c .

$$S(t) = \operatorname{erf}\left(\frac{s_c - s_i}{\sqrt{4Dt}}\right) \quad (3.84)$$

We must ensure, though, that s is set up to consistently scale the same base load value. In other words, $s = 1$ always corresponds to a 100% increase in base load. If this is not the case, then the operator specified diffusion coefficient D will become invalid. When load has increased to $S_0 + s_i S_0$ and we want to scale it though CPF, we inevitably have to do the following:

$$S = [S_0 + s_i S_0] + s (S_0 + s_i S_0) \quad (3.85)$$

We reach collapse when s hits a value s_c .

$$S_c = [S_0 + s_i S_0] + s_c (S_0 + s_i S_0) \quad (3.86)$$

In this case, s has increased from 0 to s_c , but this does NOT represent an $(s_c * 100)\%$ increase in original base load S_0 though. Therefore, we must transform the load factor such that it is always scaling S_0 .

$$s_c (S_0 + s_i S_0) = [s_c (1 + s_i)] S_0 \quad (3.87)$$

Therefore, we can compute the following survival probability.

$$S(t) = \operatorname{erf} \left(\frac{s_c (1 + s_i)}{\sqrt{4Dt}} \right) \quad (3.88)$$

In order to quantify s_i , we rearrange the equation which computes the aggregate loading of the load pocket S .

$$S = S_0 + s_i S_0 \quad (3.89)$$

\Downarrow

$$s_i = \frac{S - S_0}{S_0} \quad (3.90)$$

Therefore, when the survival probability is being computed, (3.91) is used in order to attempt to preserve the validity of the input parameter D .

$$S(t) = \operatorname{erf} \left(\frac{s_c \left(1 + \frac{S - S_0}{S_0} \right)}{\sqrt{4Dt}} \right) \quad (3.91)$$

This process can also be completed for arbitrary values of s . Say the system is operating at $s = 0$, and we want to know the survival probability of some future operating point where the load (or loads) has been scaled by s_m . We simply use the difference between s_c and s_m (where $s_c > s_m$).

$$S(t) = \operatorname{erf} \left(\frac{(s_c - s_m) \left(1 + \frac{S - S_0}{S_0} \right)}{\sqrt{4Dt}} \right) \quad (3.92)$$

3.5 Using HELM to Compute Optimal Control Action

Aside from using CPF via HELM to gauge proximity to voltage collapse, it can also be reformulated in order to calculate optimal reactive power injection. When every bus in a power system is operating on the high side of the nose curve, the system is voltage stable. For any voltage stable system, the injection of additional reactive power causes voltage magnitude to increase [14]. Therefore, HELM can be formulated such that the loading rates are equal to 0 at all buses besides condenser bus C .

$$\mathbf{k}_i = \begin{cases} 1 & i \in C \\ 0 & \text{otherwise} \end{cases} \quad (3.93)$$

In this way, once HELM has been formulated, (4.97) can be used to calculate the maximum amount of reactive power injection (to give the system maximum stability) without violating an upper limit on voltage magnitude (such as 1.075 pu). This allows us to compute the optimal amount of reactive power injection. In a real world setting, pushing voltage at a bus up to some maximum threshold may not be wise control action, because if load decreases, voltage will spike. For the sake of our experiments, though, the load is monotonically increasing, so over-voltage protection is not an important consideration.

3.6 Controller Overview

In order to test the validity of using bus voltage variance in order to determine when control action is necessary, we designed, implemented and tested three controllers. The flowchart overview of these controllers are presented in Figures 3.5, 3.6, and 3.7, and they are designed to be implemented in a load pocket with a high degree of observability. We define the term load pocket as a group or cluster of interconnected buses with no internal generation and high load levels. Having a high degree of observability in a load pocket is achieved either through (1) deployment of PMUs at each bus in the load pocket, or through (2) optimal placements of PMUs combined with network math which has the potential to transform sparse system measurements into a full set of system measurements. Such a process is outlined in [45]. We assume a high degree of stability outside of the load pocket in question. This assumption allows for the loads outside of the load pocket to increase and decrease without having a major effect on the statistics of the load pocket. The controllers rely on having full control over a reactive power resource such as a Synchronous Condenser (SC) inside the load

pocket.

To be clear, the following three controllers take steady state control action. In the case of the first two controllers, we (1) perturb the load load level, (2) run a 60 second time domain simulation, and then (3) perform steady state control action, if necessary, based on a “snap shot” of the time domain simulation results. A similar process is followed for the third controller.

Controller 1

Controller 1, as shown in Figure 3.5, relies on variance and mean statistics in order to determine if either a stability or voltage magnitude violation has occurred. In this experiment, we assume the loads in a load pocket of interest increase together monotonically, but we run CPF for a variety of normalized loading rates to ensure that we account for a variety of different contingencies. The loading rates can be chosen using operator knowledge of how certain loads jointly change over time. Since we are dealing with a fictitious system, we generated our loading rates (found in Table 3.3) by generating a vector of rates (from 0.90 to 1.10) and then assigning each rate to a bus in the load pocket. Next, the vector was rotated by one index, and these new rates were assigned to each bus. This process was repeated until each bus was assigned each loading rate at least once. Of course, there are an infinite number of other loading rates schemes which could have been applied to the buses, each with a different bifurcation point. This particular method assumes the loads will all increase at approximately an equal rate, but some might increase slightly faster or slower than others. Each loading rate scheme engenders a new critical variance profile to account for these conceivable differences.

After running HELM and determining the distance to voltage collapse (the distance from $s = 0$ to $s = s_c$), the loads are mathematically scaled according by the product of their assigned loading rate and s_m , where $0 \leq s_m < s_c$. The value of s_m is computed by setting (3.92) equal to the desired minimum acceptable survival probability (as specified by the operator). The represents the edge of the desired probabilistic threshold; if s increases beyond s_m , then the probability of voltage collapse becomes too severe. After scaling the loads according to this factor, we use the method presented in Section 3.2 in order to determine the algebraic covariance matrix for the system. Doing so requires dynamic models and updated state variables for the entire system. The diagonal elements of this matrix contain what we have termed “critical variances”, meaning that if the variance measurements of the system match this profile, then there is a high probability that the system is on the predefined probabilistic voltage collapse threshold. In this case, control action should be

taken, as the probability of voltage collapse is too high. Every 60 seconds, the bus voltage variance is measured for the buses in the load pocket. At any bus, if the measured variance is larger than the critical variance, then a violation has occurred. Similarly, if at any bus, the bus voltage mean has dipped below a certain critical threshold, a violation has occurred. If no violation has occurred, PMU data is continuously monitored and tested. When new state estimated data are available, the critical variances can be updated. This update may not be necessary, though, unless the system has changed drastically. Otherwise, the critical variance profiles will change only slightly. If a violation has occurred, the controller uses (3.93) to calculate the maximum amount of reactive power that can be injected at the SC bus without causing an over-voltage violation.

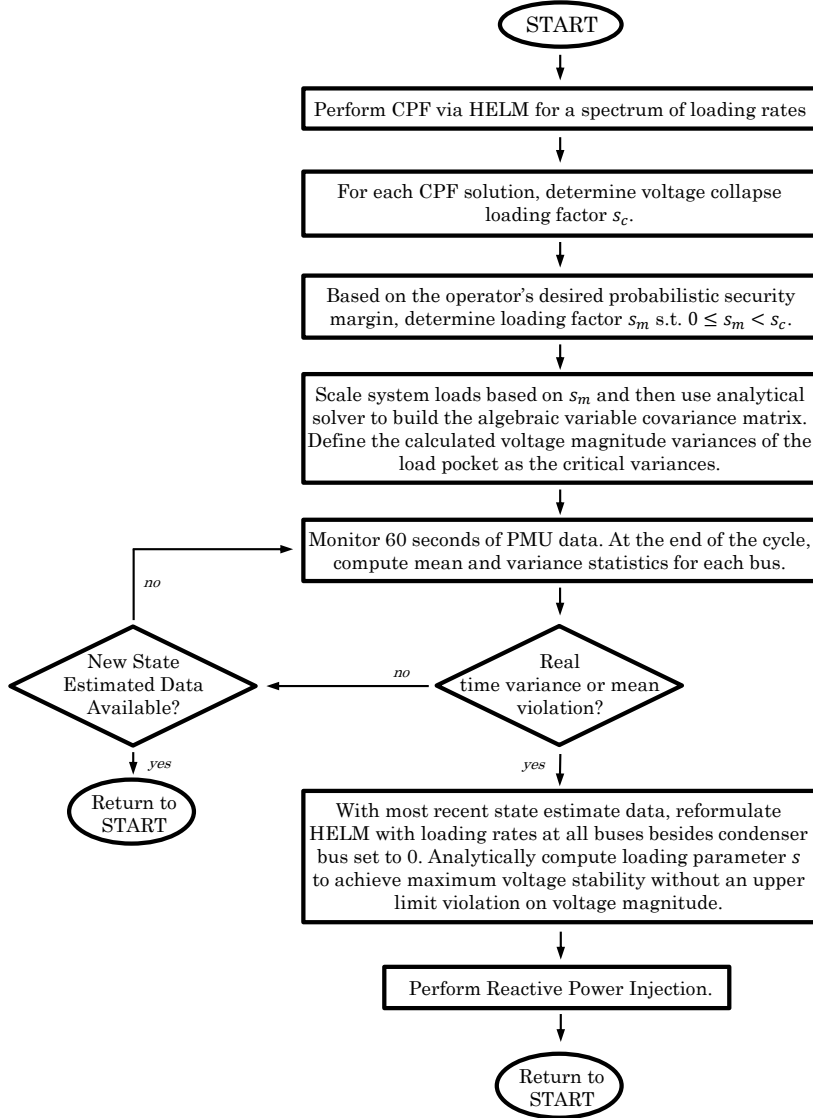


Figure 3.5: Controller 1: Flowchart Overview of the Variance and Mean Based Controller. When determining if a violation has been made, both the mean and the variance of the bus voltage data are considered.

Controller 2

Controller 2, as shown in Figure 3.6, relies on mean statistics in order to determine if a voltage magnitude violation has occurred. If the mean of the bus voltage of any bus inside the load pocket, over a 60 second period, is less than a critical value, then a violation has occurred. In this case, the

controller again uses (3.93) to calculate the maximum amount of reactive power that can be injected at the SC bus without causing an over-voltage violation. In this way, controller 1 and controller 2 take the same sort of control action when a violation occurs. The primary difference between the controllers is in determining *if* a violation has occurred.

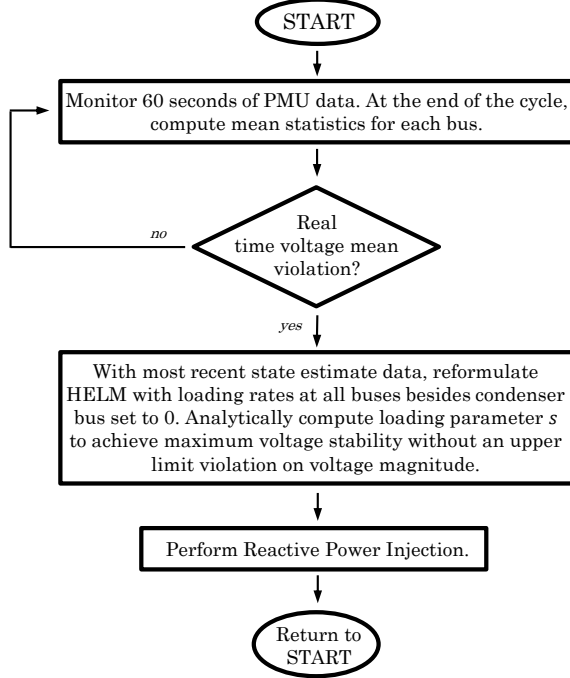


Figure 3.6: Controller 2: Flowchart Overview of the Mean Based Controller. When determining if a violation has been made, only the mean of the bus voltage data is considered.

Controller 3

Controller 3, as shown in Figure 3.7, simply holds the SC bus at a constant voltage of 1 per unit. Whenever the load is increased or perturbed in one way or another, HELM is formulated to calculate the amount the reactive power injection at the SC must be increased by in order to hold its bus voltage constant. This sort of procedure is consistent with typical reactive power control at SC buses.

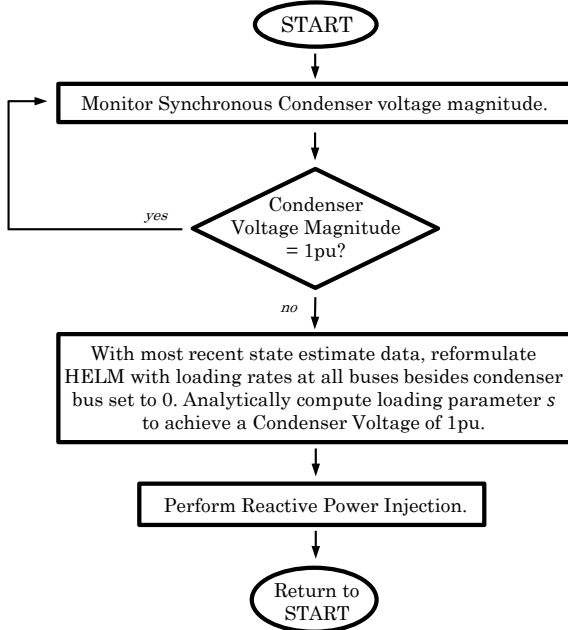


Figure 3.7: Controller 3: Flowchart Overview of the Controller Based on Synchronous Condenser Regulation. This controller does not consider the statistics of the buses inside the load pocket. Instead, it simply injects enough reactive power to hold the condenser at 1 p.u. at all times.

3.7 Test Results

In this section, we present results from various experimental trials. In Section 3.7.1, we test all three controllers on a load pocket in the 39 Bus system and contrast their effectiveness. In Section 3.7.2, we demonstrate how active power control (or battery management of some sort) in a system which has run out of reactive power control options can be driven by variance signals. And in Section 3.7.3, we briefly demonstrate the effectiveness of each controller on a large 2383 bus test case.

3.7.1 IEEE 39 Bus System: Reactive Power Controller Tests

3.7.1.1 System and Experiment Set Up

In this experiment, a load pocket is identified in the 39 bus test system, and a condenser bus is added in the center of the load pocket. Identical transmission lines tie the SC bus to the buses 3, 4, 15, and 16. The parameters of this line are set slightly lower than the average R, X, and B values

across all 46 transmission lines in the system to ensure strong, yet realistic, voltage support. This configuration is shown in Figure 3.8. In this system, reactive power limitations on generators are not considered, and the SC bus can inject as much reactive power as the controller requests. We assume full observability of the load pocket, such that 30Hz PMU data for each of the seven buses is available after each time domain simulation.

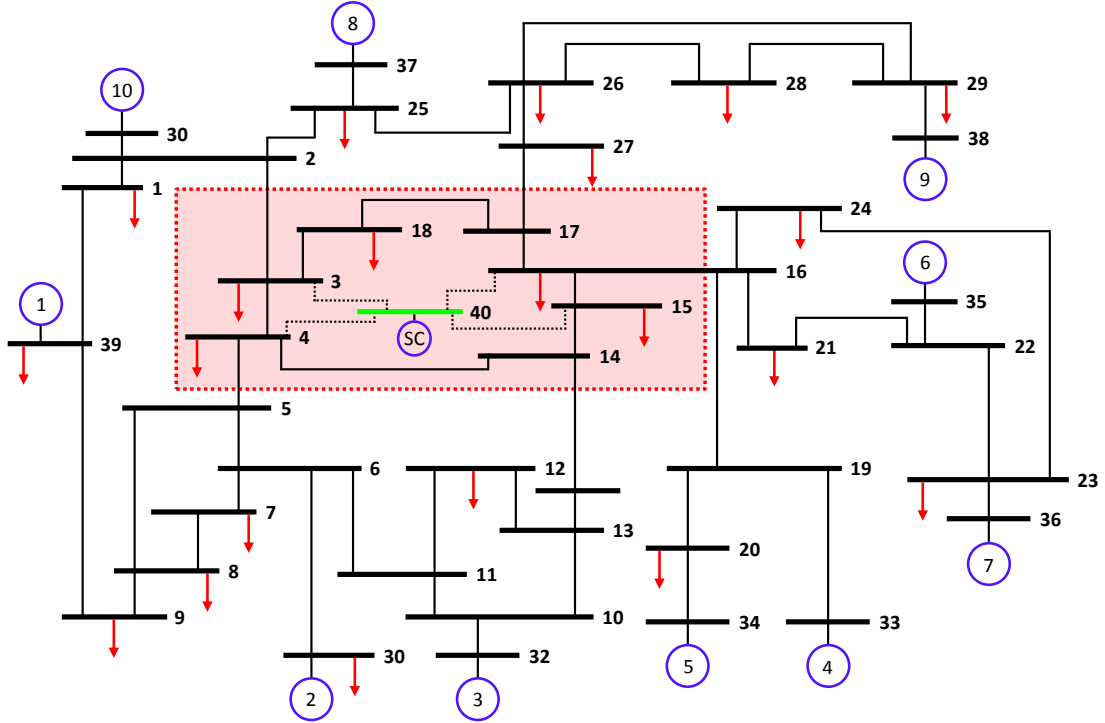


Figure 3.8: IEEE 39 Bus System with Load Pocket Identified (Buses 3, 4, 14 15, 16, 17, and 18) and Synchronous Condenser Bus Added (Bus 40)

This network contains 10 four variable synchronous generators. Each generator is equipped with a three-variable turbine governor model for frequency control and a four-variable exciter model (AVR) for voltage regulation. In order to test the controllers, the following inputs must be defined by the operator. For each variable, we indicate what we used for experimental purposes.

1. **Load Pocket Buses:** We define buses 3, 4, 14 15, 16, 17, and 18 as the load pocket of interest.
2. **Synchronous Condenser Bus:** We define bus 40 at the SC bus. It is tied to buses 3, 4, 15 and 16.
3. **Minimum Critical Voltage:** What is the lowest allowable bus voltage magnitude? We define this as 0.92 p.u.

4. **Maximum Critical Voltage:** What is the largest allowable bus voltage magnitude? We define this as 1.08 p.u.
5. **Run Time:** How long should PMU data be collected before it is processed? We buffer data for 60 seconds, perform processing, and then make control decisions.
6. **HELM Recursive Routines:** Since HELM is recursive in nature, the operator must prescribe how many recursions, or power series terms, are required in order to solve HELM. We set $n = 23$ in order to achieve an extremely high level of accuracy, but such a large value is not necessary. In order to avoid loss of accuracy associated with poor conditioning of the Padé matrix, as discussed earlier in this chapter, we built safeguards into our code which disregard power series terms which are either too large or too small. This prevents poor matrix conditioning.
7. **Load Noise:** The operator must prescribe the standard deviation of the fast noise associated with each load in the system if the loads were all scaled to unity. We use the noise model described in Section 3.2.6 where the standard deviation of the load noise grows linearly with the size of the load, and active and reactive power at a bus fluctuate in unison. For this experiment, we set noise intensity $\sigma_\xi = 0.01$ for each load in the system. This value acts as an input for two important processes: (1) our dynamic time domain simulations and (2) our analytical covariance matrix solver.
8. **Load Variation Time Period:** This is the variable t in the denominator of (3.92), and it corresponds to the time (in minutes) for which we wish to calculate survival probability. We use the value of $t = 5$ minutes since real time load forecasting occurs every 5 minutes or so, and we wish to determine the probability that the load increases to a level which causes static voltage collapse during this period.
9. **Diffusion Coefficient:** This is the variable D in the denominator of (3.92), and it corresponds to the variance of the base load values (with high frequency load variations filtered out) over a period of minutes t . We set this value to $D = 0.0001$. An operator must set this parameter based on prior experience with load variability over a time period t .
10. **Maximum Allowable Probability of Collapse:** If a system is operating at its current state, this is the maximum allowable probability of collapse which operators will tolerate. It corresponds to one minus the survival probability of (3.92). If this value is exceeded, control

action must be taken (only Controller 1 considers this metric). We set this value to $PC = 0.001$ which corresponds to a 0.1% probability of voltage collapse over a 5 minute period. This is fairly tight security. Jointly, our chosen values of PC , t , and D collectively correspond to a 0.1% chance of the aggregate load pocket load increasing by 10% over a 5 minute period. This is a conservative scenario, since 10% load forecasting error is very high and would correspond to a very rapid load build up.

11. Load Rates: In order to gauge proximity to voltage collapse, the operator must have an idea of how the loads in the load pocket are going to increase in order to define the vector \mathbf{k} (see (3.93) for example). For the sake of this experiment, we assume the loads in the pocket are all increasing monotonically and approximately uniformly, but in case the loads increase at slightly different rates (as we have set up in our experiment), we use a matrix of loading rates to cover a small range of different possibilities. For example, in the load pocket of the 39 bus system, there are $n = 5$ buses which contain loads. Therefore, we come up with $n + 1$ loading rate schemes (LRSs).

	LRS1	LRS2	LRS3	LRS4	LRS5	LRS6
Bus 3	1	0.90	1.10	1.05	1.00	0.95
Bus 4	1	0.95	0.90	1.10	1.05	1.00
Bus 15	1	1.00	0.95	0.90	1.10	1.05
Bus 16	1	1.05	1.00	0.95	0.90	1.10
Bus 18	1	1.10	1.05	1.00	0.95	0.90

Table 3.3: Unitless Loading Rate Profiles. Each row corresponds to a particular bus, while each column corresponds to a different plausible load increase situation. By generating these different loading rates schemes, we are able to generate a variety of critical variance threshold profiles. After generating this table, the loading rates are normalized (not shown) such that aggregate load pocket load increases by the same amount for each scheme as the holomorphic parameter s is scaled.

The previous list of variable definitions correspond to operator input parameters. We also make assumptions about how the loads change which the operator is blind to. We start each experiment with the same base load values. After each minute, we perturb the load in the following way³ at bus i :

$$P_i(t+1) = \alpha P_i(t) \quad (3.94)$$

$$Q_i(t+1) = \beta Q_i(t) \quad (3.95)$$

³It is important to understand that load increases are affected by the slowly varying parameters α and β , while the noise associated with load fluctuations from time step to time step is 0 mean and quickly varying.

In our experiment, the slowly varying parameters α and β are modeled by Gaussian distributions and have the following associated statistics.

$$E[\alpha] = E[\beta] = 1.01 \quad (3.96)$$

$$\sigma_\alpha = \sigma_\beta = 0.001 \quad (3.97)$$

Therefore, after each minute, the loads in the load pocket increase by approximately 1%. Since the standard deviation of α and β is tight, the power factor of each load remains relatively fixed. In the case of Controller 1 and Controller 2, the load is increased, a time domain simulation is run, and then measurements are processed. If there is a violation, control action is taken. In the case of Controller 3, when the load is increased, we assume the controller can instantly adjust reactive power injection in order to hold it constant.

3.7.1.2 Simulation Processes

In order to clarify our simulation processes and methods, we present Table 3.4.

Process	Method
Power Flow Solutions	Newton Raphson Routine in PSAT
Dynamic Simulations	Time Domain Simulation in PSAT using PSAT's dynamic models (see Appendix E)
CPF via HELM	Custom algebraic routine which relies on PSAT's base case power flow solution
Reactive Power Control	Custom routine which alters the reactive power injection in PSAT's system datafile
Covariance Matrix Solver	Custom algebraic routine which relies on PSAT's dynamic system model and PSAT's pre-calculated Jacobians

Table 3.4: Simulation Processes and Methods

3.7.1.3 Test Results

In order to test each controller's effectiveness and ability to respond to measured PMU data, we ran 10 simulations with identical system and experimental parameters for each controller (30 simulations total, with each simulation taking approximately 1.5 hours). In each case, the experiment was terminated either when a NR-power flow failed to converge after a ~1% load increase or when a

bifurcation was reached during a time domain simulation (this could occur because of a Hopf or a SN bifurcation). Table 3.5 summarizes the simulation results. The success of each controller, in one sense, can be based on how large the load (which is given as the aggregate load pocket load) is able to grow before bifurcation occurs.

	Initial Load	Largest Load	Smallest Load	Average Load
Controller 1	$61.9 + j15.3$	$99.0 + j24.5$	$96.5 + j23.8$	$97.9 + j24.1$
Controller 2	$61.9 + j15.3$	$95.8 + j23.8$	$89.9 + j22.4$	$93.1 + j23.0$
Controller 3	$61.9 + j15.3$	$92.3 + j22.9$	$90.0 + j22.2$	$91.1 + j22.5$

Table 3.5: Initial, Largest, Smallest, and Average Load Level Reached before Bifurcation for Controllers 1, 2, and 3 over all 10 Simulations. Load Values, which are calculated as the aggregate of the load in the load pocket, are all given in p.u. with a 100MVA Base.

Clearly, Controller 1 is able to deter bifurcation most successfully. To quantify the success of each controller, we compare how much the aggregate load (in terms of apparent power) was able to increase from the base load condition to the average bifurcation point.

	Initial Load (p.u.)	Average Bifurcation Load (p.u.)	Percent Increase (%)
Controller 1	63.8	100.8	58.0
Controller 2	63.8	95.9	50.3
Controller 3	63.8	93.8	47.0

Table 3.6: Average Percent Increase in Apparent Power Loading for Controllers 1, 2, and 3 Over the 10 Simulations. Load Values are all given in p.u. with a 100MVA Base.

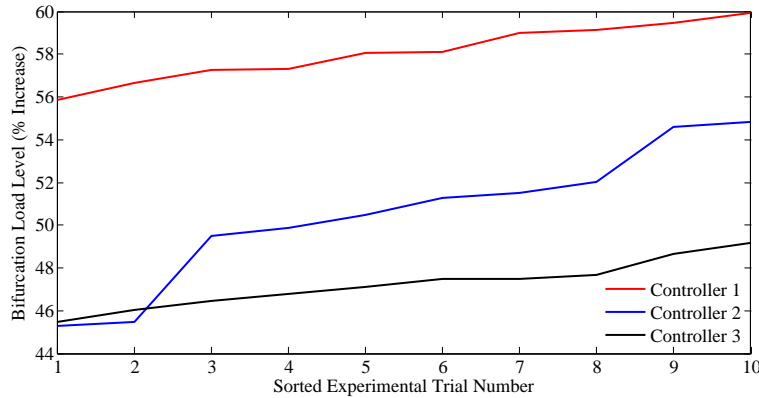


Figure 3.9: Bifurcation Load Level for Each Controller Across 10 Trials. The percent increase is given as an aggregate apparent power ratio from the base case to the bifurcation case. For graphical clarity, the experimental trials results are sorted for each controller such that the traces are monotonically increasing.

Although the percentages in Table 3.6 and Figure 3.9 are highly dependent upon the base loading condition of the system, for our configuration, Controller 1 is able to outperform Controller 2 and Controller 3 across all trials. To understand why this is so, we present several other sets of results. Figures 3.10, 3.11, and 3.12 show the average load pocket voltage magnitude mean and voltage magnitude variance as load increases for the three controllers. In these figures, the statistics are collected from time domain simulations which are run directly *after* the loads have been increased according to (3.94) and (3.95). This means Controller 1 and Controller 2 will not have taken action yet (since they need to sense a violation before taking control action), but Controller 3 will have (since it holds voltage magnitude at the condenser constant at all times).

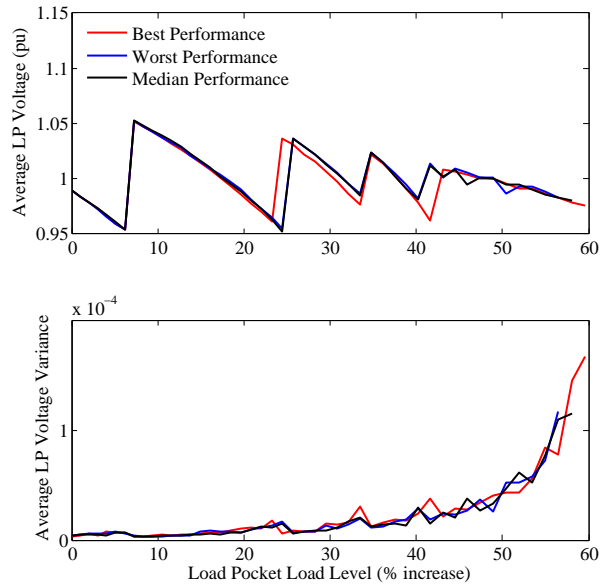


Figure 3.10: Voltage Magnitude and Variance for Controller 1 as Load Increases. Show are traces for three simulations: the simulation which allows load to increase the most, the least, and the median amount.

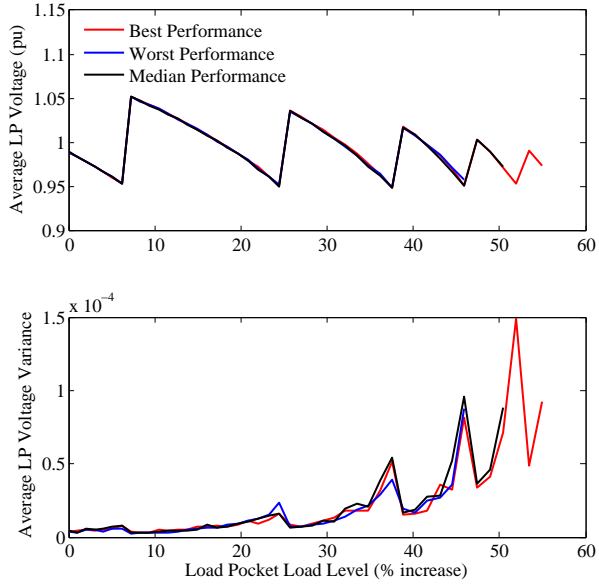


Figure 3.11: Voltage Magnitude and Variance for Controller 2 as Load Increases. Shown are traces for three simulations: the simulation which allows load to increase the most, the least, and the median amount.

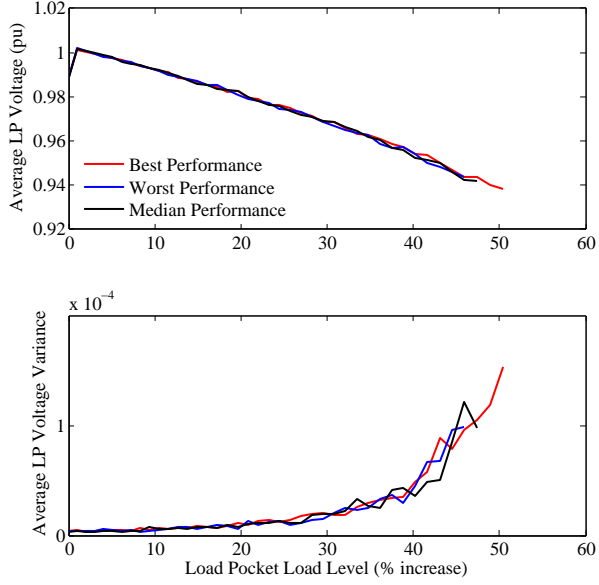


Figure 3.12: Voltage Magnitude and Variance for Controller 3 as Load Increases. Show are traces for three simulations: the simulation which allows load to increase the most, the least, and the median amount.

In Figure 3.10, control action is primarily due to voltage magnitude violations initially, but as load and reactive support increase, control action is taken in response to variance signals. For this

reason, voltage variance measurements increase approximately monotonically. In contrast, Figure 3.11 shows that the system is taking control action in response to voltage magnitude violations only. For this reason, voltage variance measurements are constantly spiking up and down as the system gets extremely close to the stability threshold. The average voltage magnitude in 3.12 is monotonically decreasing. The nose curve has a very gentle slope to it, even right before bifurcation, because control action is taken directly after load increase each time the load changes. The nose curve alone makes the system appear stable, but the bus voltage variance in the bottom frame tells a different story. Of course, bus voltage variance is used to determine if a stability margin has been crossed. For each controller, we plot the probability of collapse for a representative trial (as opposed to three trials). In each case, we plot the probability of system collapse directly *after* control action has been taken for all three controllers.

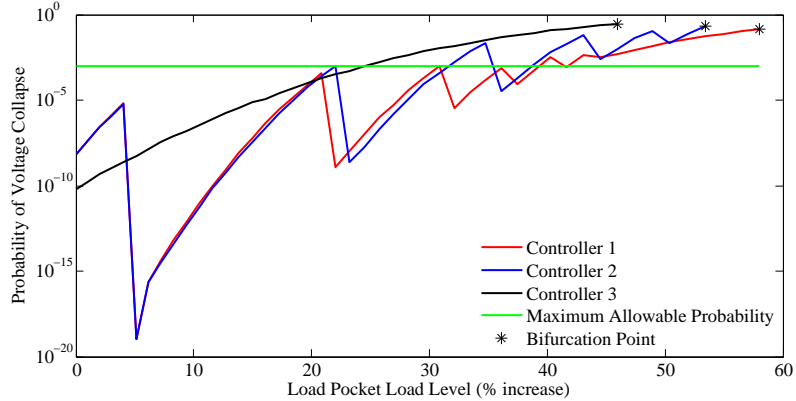


Figure 3.13: Probability of Voltage Collapse in the 39 Bus System. For each controller, the probability of voltage collapse is shown as the system iterates forward and load level increases. For determining probability of collapse, we abandon the various loading rate schemes presented in Table 3.3 and simply use the first column (uniform loading rates).

Controller 3 has a steady increase in probability of collapse until the system bifurcates. Controllers 1 and 2 track with each other for the first 19 iterations (21% increase), but Controller 1 takes actions sooner than Controller 2 does at this iteration. As can be seen, each time Controller 1 approaches the green threshold, it takes action to push the system back below this margin. It does this until it can do so no longer. Once this is the case, the system takes continuous control action at each iteration. Of course, the probability of voltage collapse is directly tied to the amount that the holomorphic parameter s can increase and thus scale each load. Figure 3.14 shows, for each controller, how much s can increase at each operating point before the system crosses the

maximum allowable probabilistic threshold (panel (a)) and how much s can increase at each operating point before the system reaches a state of static voltage collapse (panel (b)).

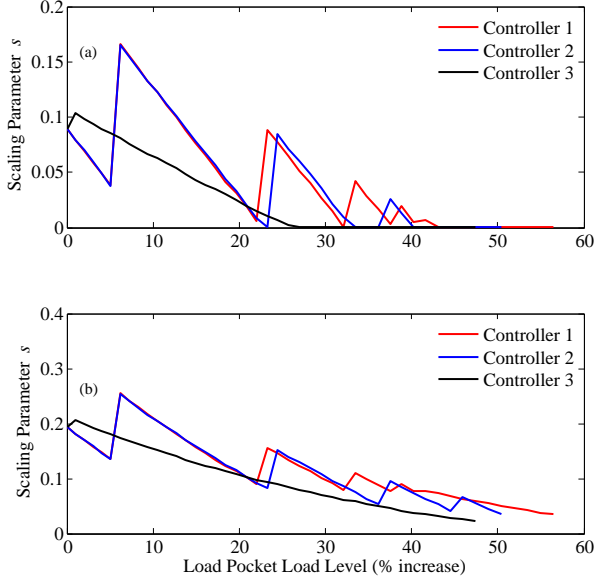


Figure 3.14: 39 Bus System Distance to Voltage Collapse and Distance to Probabilistic Margin as Load Increases. Panel (a) shows how much the holomorphic parameter s can increase for each system until the probabilistic threshold diminishes to 0. Panel (b) shows how much the holomorphic parameter s can increase for each system until the system reaches static voltage collapse.

Panel (b) clearly shows that Controller 1 is able to hold the system away from the voltage collapse point ($s = 0$) most successfully, thus increasing the lifespan of the system. This is due to the continuous control action taken by the controller, as determined by the variance violations. Controller 2, on the other hand, takes no control action beyond load increase = 46% since no voltage magnitude violations occur.

What is surprising about this plot is that the three systems bifurcate at different distances from $s = 0$. One may expect the systems to bifurcate in the time domain simulation after s reaches some critically low, consistent value. This is not necessarily the case, though, for two primary reasons. First, the time domain simulation may bifurcate due to a maximum power transfer point being reached (static voltage collapse), but it may also bifurcate because dynamic stability of the system is lost. Dynamic instability is strongly associated with increased power flows out of the generators, so as system loading increases, the probability of dynamic instability also increases. Second, the

holomorphic parameter s continuously scales the base load.

$$P + jQ = (P_0 + jQ_0) + s(P_0 + jQ_0) \quad (3.98)$$

As load increases, though, the noise associated with the load also increases. Therefore, in a time domain simulation, loads in a system with a high value of s will potentially fluctuate to larger values than loads in a system with a small value of s . This makes the probability of bifurcation higher, even if both systems are operating at the same stability margin.

3.7.2 IEEE 39 Bus System: Using Variance to Manage Active Power Injection

As shown very clearly by the red trace in Figure 3.13, there comes a point in the operation of the system (around load increase = 42%) when the injection of additional reactive power cannot push the system back into the region of stability which the operator may desire for it to be operating in. In this situation, deploying active power resources, such as battery power management or distributed load control of some sort, may be of great interest to the operator. In order to show the usefulness of such measures, we add an active power resource (such as a battery) to the SC bus. This is shown in Figure 3.15. When the battery discharges, it shall alleviate the active power flows on the surrounding transmission lines.

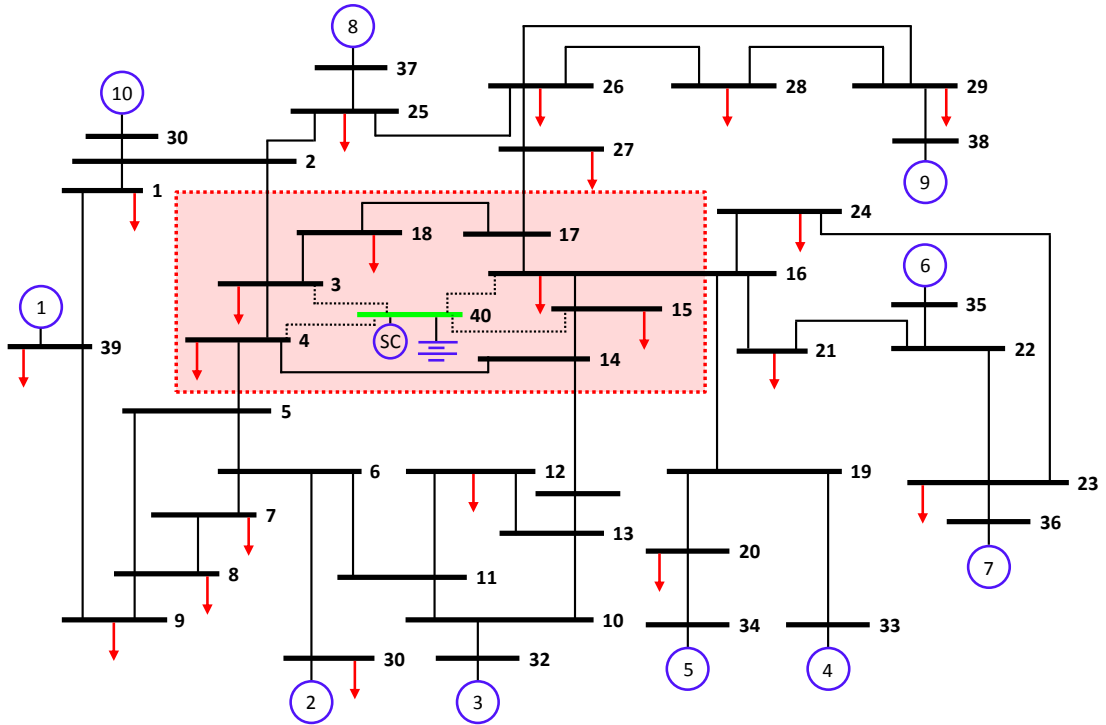


Figure 3.15: IEEE 39 Bus System with Synchronous Condenser Bus and Battery Resource Added

One way for controlling the battery in real time is through jointly monitoring bus voltage variance and bus voltage magnitude statistics. Essentially, the effectiveness of reactive power injection diminishes when bus voltage variance is high (it has crossed the probabilistic threshold) and bus voltage magnitude is also high. In this way, when these two conditions are met, we trigger active power injection.

We show the value of active power control in the following experiment. We use the same system configuration and parameters as described in Section 3.7.1, except a battery is added to bus 40. Controller 1 is used to stabilize the system until reactive power injection can no longer maintain the stability of the system (such that the probability of voltage collapse is less than 0.01%). High variances and high bus voltage magnitudes trigger active power control. For the sake of this experiment, we inject active power in the same way that reactive power is injected: we inject as much as possible without any bus in the system exceeding an upper threshold on voltage magnitude (1.08 p.u.).

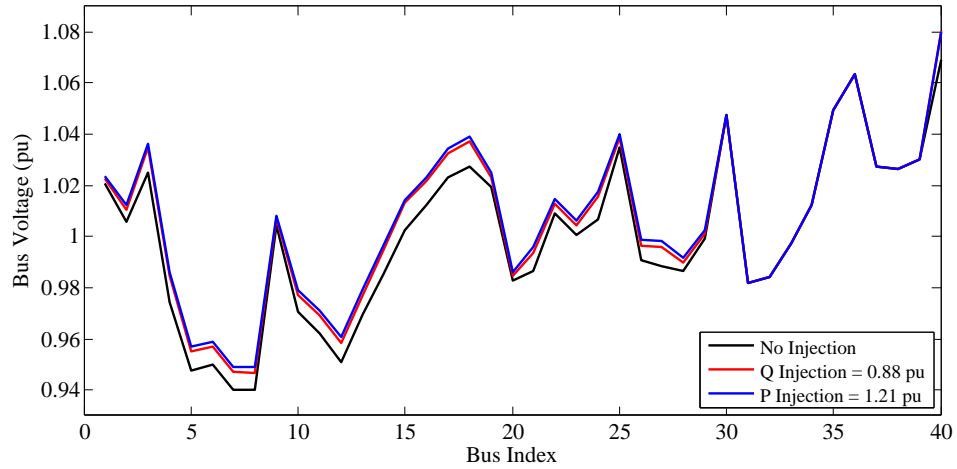


Figure 3.16: Voltage Profile of 39 Bus System While Operating at the Stability Threshold. After a load increase, the black trace shows the system voltage profile if no control action is taken. The blue trace shows the voltage profile if active power is injected, and the red trace shows the voltage profile if reactive power is injected. In each case where action is taken, the maximum amount of power (P or Q) is injected such that no bus exceeds the upper threshold on voltage magnitude.

Injecting active power and reactive power clearly have quite similar affects on the voltage profile of the system. The injections, though, shift the nose curve of the system in very different ways.

Injecting more reactive power causes the nose curve to shift “up and out” as shown by the red and blue nose curves of Figure 1.12. Injecting active power, on the other hand, lessens the effective power factor of the nose curve and causes the nose to shift downwards. When the system is experiencing such a critical loading condition, this is the more effective method of stabilizing the system. This is shown explicitly by Figure 3.17 through a plot of the probability of voltage collapse for various injections.

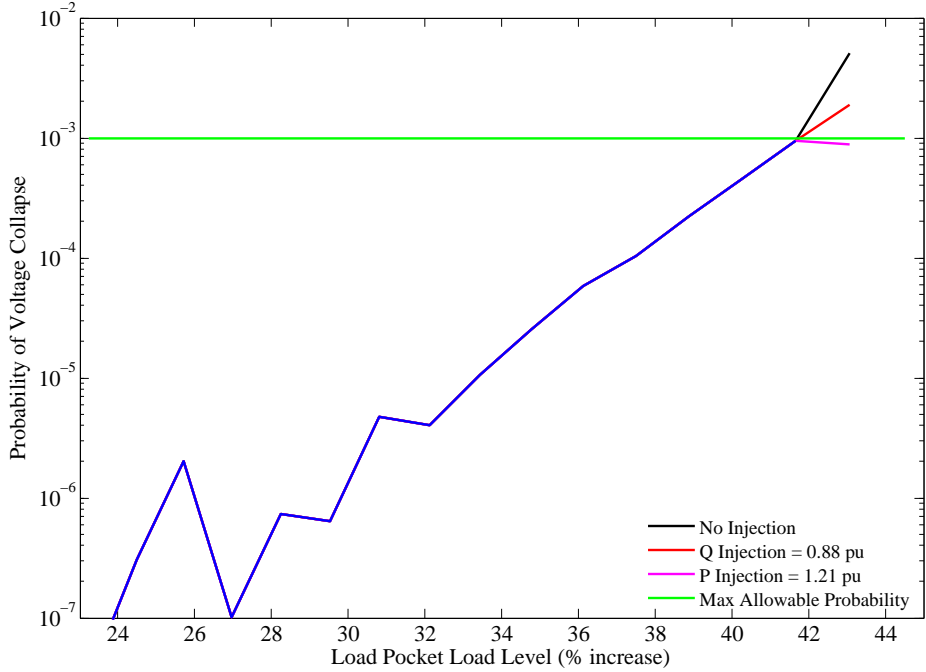


Figure 3.17: Probability of Collapse on the 39 Bus System for Various Injections. For graphical clarity, the first 21 iterations (or load increases) are not shown in this plot (probability of collapse is very low). When load increase reaches 41.5%, reactive power injections are unable to stabilize the system. The high voltage variances (which cross the critical threshold) coupled with very high bus voltage magnitudes trigger active power injection. The back trace shows what will happen to the probability of collapse if no control action is taken. The red trace shows how the system will stabilize if the maximum amount of reactive power is injected into the system. Finally, the magenta trace shows that an active power injection will stabilize the system adequately.

Taking no control action will cause the probability of collapse to rise to a value of 0.05%, while injecting reactive power will cause the probability to rise to 0.19%. Both of these values surpass the maximum allowable probability of 0.1%. Injecting active power will cause the probability of collapse to drop to 0.088%. This provides a sufficient margin of voltage stability. We must note that 1.21 p.u. of active power in a system with a 100MVA base translates to 121 MW of power. This is an enormous amount of power (the state of Vermont, for comparison, has an aggregate peak load of approximately 1000MW).

3.7.3 Polish 2383 Bus System

In order to further validate the usefulness of employing variance as an actionable control signal, we test it on a load pocket of the 2383 bus Polish system. At the start of the experiment, we push the system right to the brink of collapse. We then show that a voltage magnitude violation never even

occurs before the system collapses.

3.7.3.1 System and Experiment Set Up

The topology of the Polish system is shown in Figure 3.18.

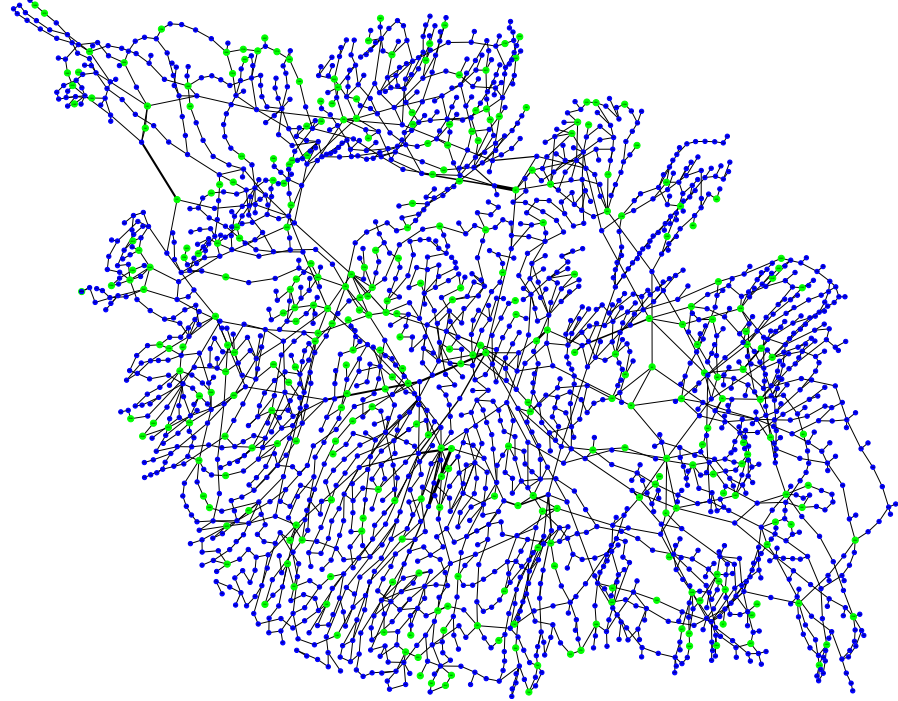


Figure 3.18: Topology of the Polish System. Load buses are shown in blue while voltage controlled generator buses are shown in green. The sizes of the colored bus circles are not drawn to scale, but the thickness of the lines is relative to the apparent power flows of the base case power flow solution.

Once again, we identify a load pocket in the system and apply these methods. The results from Chapter 2 can be used for this purpose rather nicely. For the base case power flow solution, participation factor analysis readily identify buses 466, 230, 221, 414, 240, 401, 340, 218, 434, 188, and 437 as problematic. Therefore, we define this cluster of nodes as a load pocket and test the effectiveness of Controller 1 at maintaining voltage stability in this system. The node cluster is located in the Southwest corner of the Polish system map, and an expanded view of the pocket can be found in Figure 3.19.

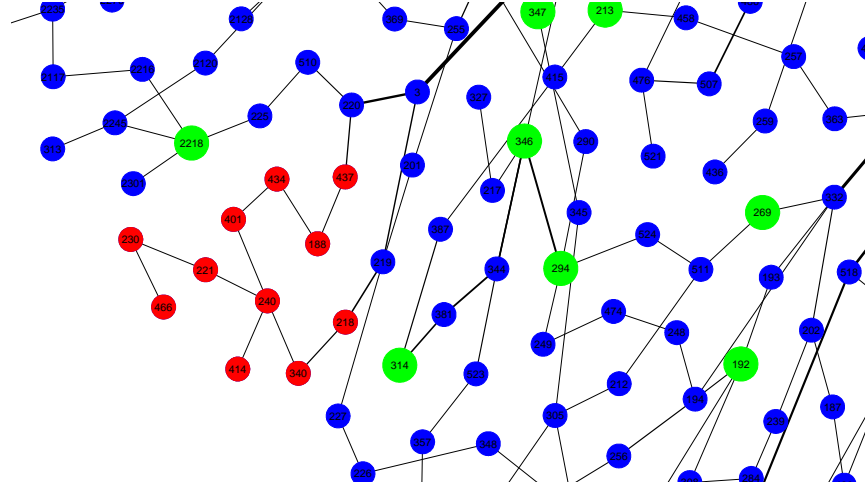


Figure 3.19: Polish System Load Pocket. Stable load buses are shown in blue, voltage controlled generator buses are shown in green, and unstable load pocket nodes are shown in red. There are 11 transmission lines between node 466 and the nearest voltage controller. The radial nature of the power distribution, along with relatively high line reactance in the load pocket, make for poor voltage stability within this area.

We then add a SC bus to the system in the center of the load pocket. Based on how we have connected its transmission lines, the SC has the ability to provide voltage support throughout the load pocket. Its connections are shown in Figure 3.20. Of course, we could have added a series of SC buses through the load pocket, or we could have placed the SC on an existing bus. All would be adequate methods for regulating voltage.

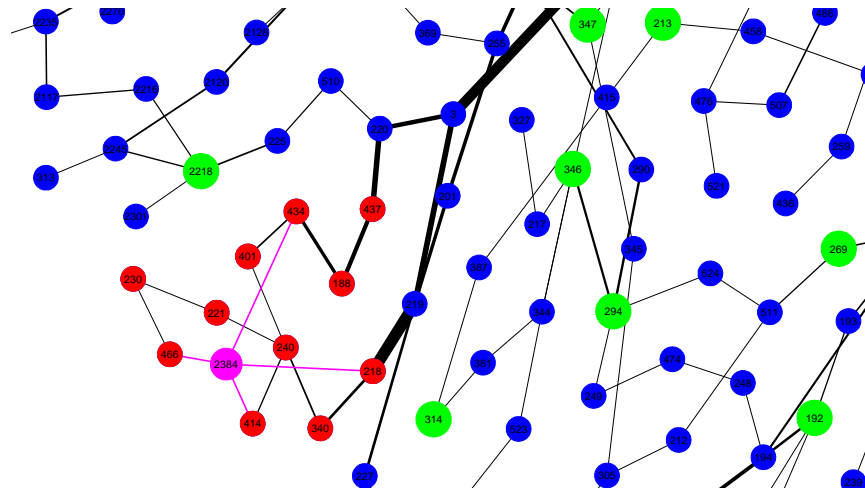


Figure 3.20: Polish System Load Pocket with SC Bus. Stable load buses are shown in blue, voltage controlled generator buses are shown in green, and unstable load pocket nodes are shown in red. The Synchronous Condenser and its transmission lines are shown in purple. The width of all transmission lines shows how the power is flowing in a heavily loaded situation.

In order to perform this experiment, we pushed the system right up to the brink of voltage instability⁴. We did this in order to limit the number of load increases necessary to reach static voltage collapse. We also decreased all complex power loads in the system by 10% in order to isolate the voltage instability to the load pocket region. As the load pocket was loaded, we applied switched shunt support at 12 buses scattered throughout the system, along with condenser support inside the load pocket, in order to maintain an acceptable voltage profile. With these given initial conditions, we test the effectiveness of Controller 1 and Controller 2 at maintaining LTVS in the system. Stability and magnitude parameters (diffusion coefficient, voltage magnitude limitations, etc.) which were used on the 39 bus system experiments, as outlined in 3.7.1.1, were also used in this experiment. Only the SC and load pocket bus indices have been updated. Table 3.7 presents the preliminary results of this experiment.

	Initial Aggregate Load (p.u.)	Max Aggregate Load (p.u.)	$ S $ Increase (%)
Controller 1	$4.805 + j0.507$	$5.053 + j0.533$	5.17
Controller 2	$4.805 + j0.507$	$4.947 + j0.523$	2.97

Table 3.7: Bifurcation Loading Statistics for Controllers 1 and 2. Load Values are all given in p.u. with a 100MVA Base.

Clearly, neither controller is able to allow a very substantial load increase, but this is primarily due to the fact that the experiment begins with the system on the verge of voltage collapse. What is substantial to note, though, is that Controller 2 never takes action over the course of the experiment, as there is never a voltage magnitude violation. Controller 1, on the other hand, takes control action after every load increase because the voltage variance is so high. Figure 3.21 shows the voltage magnitude profiles of all buses in the system (except for the added SC bus) corresponding to the initial loading condition and maximum allowable loading condition when the system is controlled by Controller 2. The bus voltage difference between these loading conditions is also shown.

⁴Due to computational expense of Polish System simulations, we only performed one trial of the experiment outlined in this section.

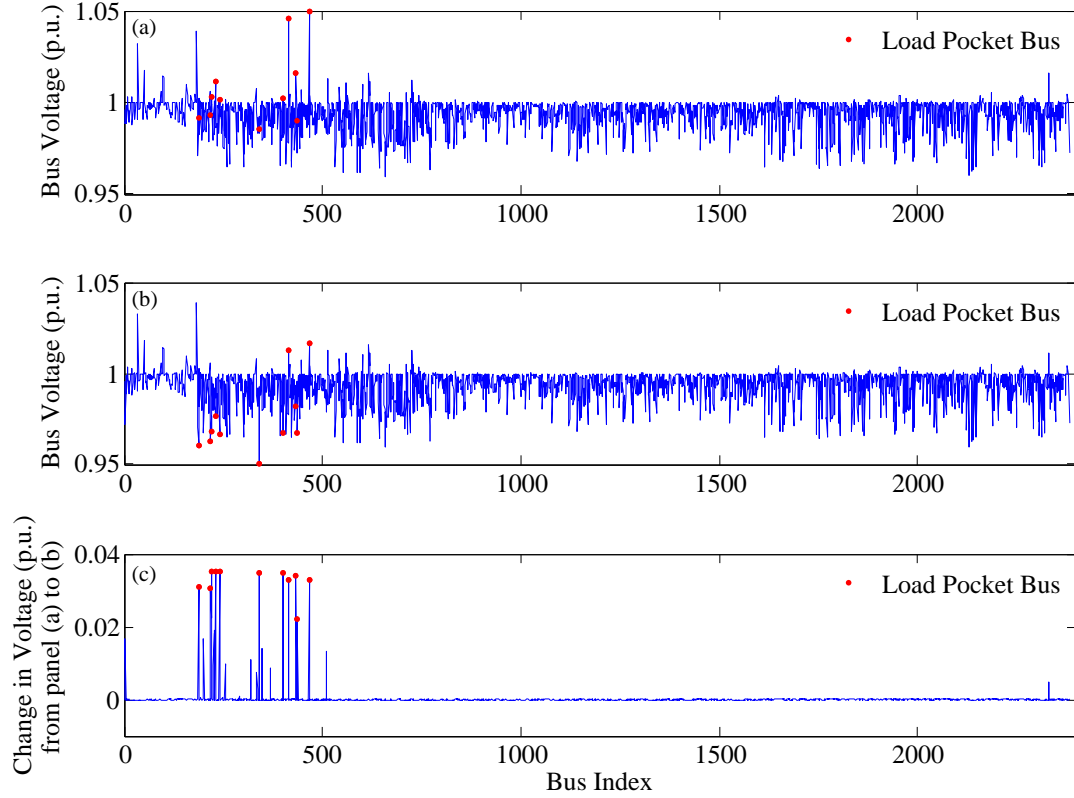


Figure 3.21: Polish System Voltage Profiles. Panel (a) presents the voltage magnitude profile for the Polish System under Initial Loading. Panel (b) presents the voltage magnitude profile for the Polish System when the load pocket has reached maximum loading (any increased loading will cause voltage collapse) when controlled by Controller 2. Finally, panel (c) presents the voltage difference between panels (a) and (b). Clearly, as the load pocket loading increases, load pocket voltages change most significantly. Buses tied to supporting lines also see a small change in voltage magnitude. In panel (b), it is significant to note that the lowest bus voltage in the system right before the bifurcation occurs is slightly above 0.95 p.u..

As load increases, Figure (3.22) presented the average load pocket voltage magnitude (panel (a)) and the average load pocket bus voltage variance (panel (b)). These statistics are collected from time domain simulations performed directly *after* load has been increased (and thus before control action has been applied).

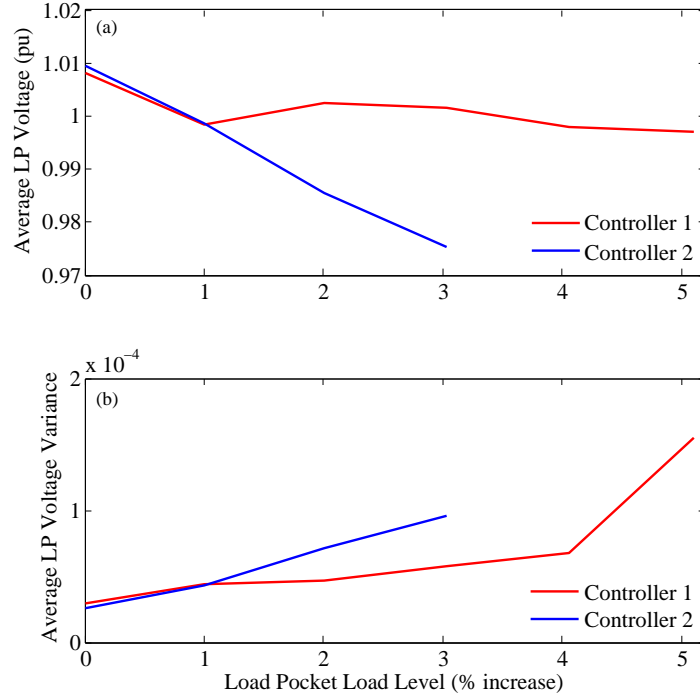


Figure 3.22: Polish System Average Voltage Magnitude and Variance for Controllers 1 and 2. Panel (a) compares the average bus voltage magnitudes. When the system is controlled by Controller 2, bus voltage magnitude is monotonically decreasing since control action is never taken. Continuous control action is taken by Controller 1, meaning bus voltage is regulated fairly well. Panel (b) shows that bus voltage variance increases are monotonic for both controllers. This is expected, since variance bus voltage variance gauges voltage stability, and it is not directly affected by the voltage magnitude.

Chapter 4

Conclusions

As reviewed in Section 1.5 and then demonstrated in Chapters 2 and 3, this thesis brings together a number technical innovations in order to gauge proximity to and then improve voltage stability through leveraging real time statistical data. Particularly, we incorporate and couple the following methods:

- Power flow Jacobian decomposition identifies locations of elevated stress
- Static algebraic voltage collapse analysis, through HELM, determines critical loading levels
- First passage probability estimates the system survival time (and thus the probability of voltage collapse)
- Statistical estimation, based on analysis of a full order system model, determines critical variance thresholds
- HELM is reformulated to determine how much control action should be taken to achieve system requirements
- Dynamical simulation is employed in order to validate system stability based on controller actions

Our approach represents an innovative and unique combination of these methods, and we hope to demonstrate the validity of combining distinct power system analysis techniques in order to develop effective control methods.

In Chapter 2, we successfully showed that the participation factors of the RPFJ can be used to locate regions of high voltage variance in a large power system. These participation factors, along with bus voltage variance, are blind to high voltage magnitudes which may give the illusion of voltage stability. These participation factors are then used in Chapter 3 to identify an unstable load pocket in the Polish Grid.

In Chapter 3, we test our method for using bus voltage variance as a control signal. As reactive support increase and the nose curve of the system rises, the variance controller (Controller 1) takes stabilizing action while the mean based controller (Controller 2) does not. Controller 3 simply holds the Condenser bus voltage constant at all times (it does not wait for a violation signal to adjust its reactive power output). Thus, Controller 1 allows the aggregate load pocket demand to increase 8% higher and 11% higher than the demand in the systems controlled by Controller 2 and Controller 3 (respectively) relative to the base loading condition. This effectively increases the “survival time” of the system. We also shown how Controller 1 can be used to control an active power resource. Active power injection may be necessary when both bus voltages magnitudes and variances are high, as the usefulness of reactive power injection will have diminished greatly in this case. In testing Controllers 1 and 2 on the Polish system, we find that Controller 2 takes no action before the system reaches collapse. Controller 1, on the other hand, takes continuous control action. Variance based control has been shown to be especially useful when the system is dangerously close to voltage collapse.

4.1 Future Work

There are a plethora of ways for improving the methods presented in this paper and further investigating LTVS. In the following three sections, we explain three such plausible improvements.

4.1.1 Generator Reactive Power Limits

In the analysis presented above, at no time did we consider the reactive power limitations on generators. We did not make these considerations because in Chapter 3, we were concerned with testing how variance can be used as a control action signal. Putting reactive power limitations on the generators does not invalidate these results. In order to add such limits, we can formulate CPF via HELM. As we begin to increase the holomorphic parameter s , the Padé approximant as given by (3.46) yields the system-wide complex voltages. As the nose curve of the system is drawn, the power flow equations can be evaluated at each generator bus. If reactive power at a generator must increase

beyond its limit, then the bus must be converted into a PQ bus. At this point, we simply reformulate the HELM equations and add a PQ bus into the system (which is the generator operating at its reactive power limit).

4.1.2 Generator Participation Factors

As indicated in Section 3.3.2, we formulate CPF via HELM by fixing the generator angles so that active power increases are proportional to the electrical distance between a load and a given generator. For voltage collapse analysis of a load pocket, this is an adequate assumption. In order to apply these methods for a full system, we must rigorously consider generator participation factors. These factors determine how much active power generation should increase at a given generator as system load increases.

In order to incorporate such factors, we consider the PV bus power balance equation (with the unaltered admittance matrix).

$$\sum_{k=1}^N Y_{i,k} V_k(s) = \frac{sP_i - jQ_i(s)}{V_i^*(s^*)} \quad i \in \text{PV} \quad (4.1)$$

As this equation stands, as s is scaled, the power generation at each generator will increase linearly. This will not do. We must modify the real power injection values for two reasons. First, the loads are not increasing at equal rates (some loads are not increasing at all). Second, we wish for the generators to respond with appropriate power dispatch relative to their sizes. Assuming all values loading rate value in the vector \mathbf{k} are known, we base the following participation factor calculations on the assumption that all generators will increase their output proportional to their size (and their size is proportional to the amount of real power they are currently injecting into the system). These factor can be derived using other assumptions, of course. In the original system, we have the following amount of power demand, where buses 1 through m are PQ buses, and buses $m + 1$ through n are generator buses (including the swing bus).

$$P_{\text{Load}}^{\text{Base}} = - \left(\Re(S_1^{\text{inj}}) + \Re(S_2^{\text{inj}}) + \cdots + \Re(S_n^{\text{inj}}) \right) = - \sum_{i=1}^m \Re(S_i^{\text{inj}})$$

As the loading parameter s is increased past 0, we have the following amount of increased load.

$$\begin{aligned} P_{\text{Load}}^{\text{Inc}} &= - \left(\Re(S_1^{\text{inj}}) + \Re(sk_1 S_1^{\text{inj}}) + \Re(S_2^{\text{inj}}) + \Re(sk_2 S_2^{\text{inj}}) + \cdots + \Re(S_m^{\text{inj}}) + \Re(sk_m S_m^{\text{inj}}) \right) \\ &= - \sum_{i=1}^m \Re(S_i^{\text{inj}}) - s \sum_{i=1}^m \Re(k_i S_i^{\text{inj}}) \quad s \in \Re \end{aligned}$$

This means the total load increases by the following amount.

$$\begin{aligned} P_{\text{Load}}^{\Delta} &= - \left(\Re(sk_1 S_1^{\text{inj}}) + \Re(sk_2 S_2^{\text{inj}}) + \cdots + \Re(sk_m S_m^{\text{inj}}) \right) \\ &= -s \sum_{i=1}^m \Re(k_i S_i^{\text{inj}}) \quad s \in \Re \end{aligned}$$

This means generation has to increase by the same amount. In order to determine how much each generator must produce, we begin by writing out the total amount of base load generation.

$$P_{\text{Gen}}^{\text{Base}} = P_{m+1}^{\text{Gen}} + P_{m+2}^{\text{Gen}} + \cdots + P_n^{\text{Gen}} = \sum_{i=m+1}^n P_i^{\text{Gen}}$$

The difference between the amount of power generated and the amount of power consumed is equal to the losses.

$$P_{\text{Loss}} = P_{\text{Gen}}^{\text{Base}} - P_{\text{Load}}^{\text{Base}}$$

Now, of course, the amount of generation must be increased by the amount that load is increased plus an additional proportional amount for increased losses (so that the swing bus does not pick up all of the added losses).

$$\begin{aligned} P_{\text{Gen}}^{\text{Inc}} &= (P_{n+1}^{\text{Gen}} + P_{n+2}^{\text{Gen}} + \cdots + P_n^{\text{Gen}}) + P_{\text{Load}}^{\Delta} + \left(\frac{P_{\text{Load}}^{\Delta}}{P_{\text{Gen}}^{\text{Base}}} \right) P_{\text{Loss}} \\ &= \sum_{i=m+1}^n P_i^{\text{Gen}} - s \sum_{i=1}^m \Re(k_i S_i^{\text{inj}}) + \frac{s \sum_{i=1}^m \Re(k_i S_i^{\text{inj}})}{\sum_{i=1}^m \Re(S_i^{\text{inj}})} \left(\sum_{i=m+1}^n P_i^{\text{Gen}} + \sum_{i=1}^m \Re(S_i^{\text{inj}}) \right) \end{aligned}$$

In this proportional scheme, if the load is increased by a factor of 2, the power generated to account for system losses is increased by the same proportional amount (a factor of 2). This is a relatively conventional assumption. Therefore, the amount by which generation must be increased is given by the following expression. For any given value of load factor s (which is a holomorphic parameter),

the following values can be computed simply.

$$\begin{aligned}
P_{\text{Gen}}^{\Delta} &= P_{\text{Load}}^{\Delta} + \left(\frac{P_{\text{Load}}^{\Delta}}{P_{\text{Load}}^{\text{Base}}} \right) P_{\text{Loss}} \\
&= -s \sum_{i=1}^m \Re(k_i S_i^{\text{inj}}) + \frac{s \sum_{i=1}^m \Re(k_i S_i^{\text{inj}})}{\sum_{i=1}^m \Re(S_i^{\text{inj}})} \left(\sum_{i=m+1}^n P_i^{\text{Gen}} + \sum_{i=1}^m \Re(S_i^{\text{inj}}) \right)
\end{aligned}$$

The task is to split up this generation value proportionally between the generators. We define a generation participation factor for each generator. This is defined for generator $m + 1$ through n .

$$\rho_i = \frac{P_i^{\text{Gen}}}{P_{\text{Gen}}^{\text{Base}}} = \frac{P_i^{\text{Gen}}}{\sum_{i=m+1}^n P_i^{\text{Gen}}} \quad (4.2)$$

The generator participation factors have the following property.

$$\sum_{i=m+1}^n \rho_i = 1$$

Therefore, we increase the generation at generator i by the following amount.

$$P_i^{\text{Inc}} = P_i^{\text{Gen}} + \rho_i P_{\text{Gen}}^{\Delta}$$

We now wish to incorporate this scheme into the original PV bus power balance equation.

$$\sum_{k=1}^N Y_{i,k} V_k(s) = \frac{\left(P_i^{\text{inj}} \right)_{\text{Base}} + \rho_i P_{\text{Gen}}^{\Delta} - j Q_i^{\text{inj}}(s)}{V_i^*(s^*)} \quad i \in \text{PV}$$

The value ρ_i is a static parameter which does not depend on the value of the holomorphic parameter s . It is now applied.

$$\sum_{k=1}^N Y_{ik} V_k(s) = \frac{\left(P_i^{\text{inj}} \right)_{\text{Base}} + \left(\frac{P_i^{\text{Gen}}}{\sum_{i=m+1}^n P_i^{\text{Gen}}} \right) P_{\text{Gen}}^{\Delta} - j Q_i^{\text{inj}}(s)}{V_i^*(s^*)} \quad i \in \text{PV}$$

The value P_{Gen}^{Δ} is dynamic parameter which depends on the current value of s . It is now applied.

$$\sum_{k=1}^N Y_{ik} V_k(s) = - \frac{\left(P_i^{\text{inj}} \right)_{\text{Base}} - s \left(\frac{P_i^{\text{Gen}}}{\sum_{i=m+1}^n P_i^{\text{Gen}}} \right) \left(\sum_{i=1}^m \Re(k_i S_i^{\text{inj}}) - \frac{\sum_{i=1}^m \Re(k_i S_i^{\text{inj}})}{\sum_{i=1}^m \Re(S_i^{\text{inj}})} \left(\sum_{i=m+1}^n P_i^{\text{Gen}} + \sum_{i=1}^m \Re(S_i^{\text{inj}}) \right) \right)}{V_i^*(s^*)} \quad i \in \text{PV}$$

Further derivation is not shown, but similar analysis as performed in Section 3.3.2 can bring this problem full circle and allow for generator participation factors to be inserted into the CPF via HELM solver. This will allow for the elimination of the fixed generator phase angle assumption.

4.1.3 Using Data Driven Covariance Matrices to Estimate the Jacobian Matrix

As explained in Section 1.2.5, there is range of literature which uses the static power flow Jacobian to gauge the LTVs and voltage collapse proximity. This Jacobian is only updated every five to ten minutes when state estimation data becomes available though. If a system has a high degree of observability, such that time series data is available at every bus for voltage magnitude, voltage phase, active power, and reactive power, then a numerical covariance matrices can be estimated. For variables X and Y , we can compute the variance and covariance terms with ease.

$$\text{Cov}(X, Y) = \frac{1}{N-1} \sum (X_i - \mu_x)(Y_i - \mu_y) \quad (4.3)$$

$$\text{Var}(X) = \frac{1}{N-1} \sum (X_i - \mu_x)^2 \quad (4.4)$$

Therefore, we can build the active and reactive power covariance matrix σ_{PQ} and the voltage magnitude and phase covariance matrix $\sigma_{\text{V}\theta}$. We now consider the relationship between complex power and voltage, given by (2.1):

$$\begin{bmatrix} \Delta \mathbf{P} \\ \Delta \mathbf{Q} \end{bmatrix} = \begin{bmatrix} J_{\mathbf{P}\theta} & J_{\mathbf{P}\mathbf{V}} \\ J_{\mathbf{Q}\theta} & J_{\mathbf{Q}\mathbf{V}} \end{bmatrix} \begin{bmatrix} \Delta \boldsymbol{\theta} \\ \Delta \mathbf{V} \end{bmatrix} \quad (4.5)$$

\Downarrow

$$\begin{bmatrix} \Delta \mathbf{P} \\ \Delta \mathbf{Q} \end{bmatrix} = [J] \begin{bmatrix} \Delta \boldsymbol{\theta} \\ \Delta \mathbf{V} \end{bmatrix}$$

The power flow Jacobian can be thought of as a linear transformation which relates complex voltage sensitivities to power injection sensitivities. As noted by (3.14), if such a linear transformation exists, and the covariance matrices of the variables can be quantified, then the power flow Jacobian can in fact relate the data driven covariance matrices.

$$\sigma_{\mathbf{PQ}} = J [\sigma_{\mathbf{V}\boldsymbol{\theta}}] J^\top$$

If the power flow Jacobian is the only unknown in this relationship, there are numerical methods (guided by a starting condition) which may be used to estimate the power flow Jacobian in real time. Such real time statistical analysis could be very useful in LTVS analysis by applying the methods outlined in Section 1.2.5.

Appendix A: Technical Notation

Phasor Current Injection at Bus i	I_i	$=$	$ I_i e^{j\phi_i}$
Phasor Voltage at Bus i	V_i	$=$	$ V_i e^{j\theta_i}$
Voltage Magnitude Bus i	V_i	$=$	$ V_i $
Current Magnitude Injection at Bus i	I_i	$=$	$ I_i $
Complex Current Across Line i, j	$I_{i,j}$	$=$	$ I_{i,j} e^{j\phi_{i,j}}$
Complex Power Load at Bus i	S_i^L	$=$	$P_i^L + jQ_i^L$
Complex Power Generation at Bus i	S_i^G	$=$	$P_i^G + jQ_i^G$
Complex Power Injection at Bus i	S_i	$=$	$S_i^G - S_i^L$
Real Power Injection at Bus i	P_i	$=$	$P_i^G - P_i^L$
Reactive Power Injection at Bus i	Q_i	$=$	$Q_i^G - Q_i^L$
Base Complex Power Injection	S_i^0	$=$	$P_i^0 + jQ_i^0$
Admittance Matrix Entry (Row i , Col k)	$Y_{i,k}$	$=$	$G_{i,k} + jB_{i,k}$
Admittance (Y Bus) Matrix	Y		
Load Bus Set	PQ	$=$	$\{1...m\}$
PV Bus Set	PV	$=$	$\{m + 1...n - 1\}$
Voltage Controlled Generator Bus Set	G	$=$	$\{m + 1...n\}$
Reference Bus ID	r		
Non-Reference Bus Set	\bar{r}		
Set of All Buses	\mathcal{N}	$=$	$1...N$
n^{th} Complex Power Series Coefficient	$V[n]$		
Number of Recursive Iterations	N_c		
Vector of Magnitudes	\mathbf{X}		
Vector of Phasors	$\tilde{\mathbf{X}}$		
Matrix "M"	M		

Appendix B: Common Abbreviations

AVR	Automatic Voltage Regulator
CPF	Continuation Power Flow
CSD	Critical Slowing Down
DAE	Differential-Algebraic Equations
EWS	Early Warning Signs
HELM	Holomorphically Embedded Load Flow Method
IEEE	The Institute of Electrical and Electronics Engineers
LHS	Left Hand Side
LP	Load Pocket
LTVS	Long Term Voltage Stability
MPTP	Maximum Power Transfer Point
NRPF	Newton Raphson Power Flow
PMU	Phasor Measurement Unit
PSAT	Power System Analysis Toolbox
RHS	Right Hand Side
RPFJ	Reduced Power Flow Jacobian
SC	Synchronous Condenser
SG	Synchronous Generator
TG	Turbine Governor
SN	Saddel-Node
VSI	Voltage Stability Index

Appendix C: Nose Curve

Derivation

We can analytically solve for the load bus voltage magnitude as a function of loading, power factor, line parameters, shunt support, and tap ratio. We begin by formulating the admittance matrix for the circuit presented in Figure 1.8. Note that since the transformer does not shift the phase of the voltage, the Y bus matrix is fully symmetric.

$$Y = \begin{bmatrix} Y_{ff} & Y_{ft} \\ Y_{tf} & Y_{tt} \end{bmatrix} = \begin{bmatrix} \frac{G+jB+j\frac{B_{sh}}{2}}{c^2} & \frac{-G-jB}{c} \\ \frac{-G-jB}{c} & G+jB+j\frac{B_{sh}}{2}+jB_s \end{bmatrix} \quad (4.6)$$

We apply the power flow equations (1.16) and (1.17) at the load bus only. Since the “from” bus is attached to a generator, we assume $\theta_f = 0$ and $V_f = 1$.

$$P_t = V_t^2 G + V_t \left[-\frac{G}{c} \cos(\theta_t) - \frac{B}{c} \sin(\theta_t) \right] \quad (4.7)$$

$$Q_t = -V_t^2 (B + \frac{B_{sh}}{2} + B_s) + V_t \left[-\frac{G}{c} \sin(\theta_t) + \frac{B}{c} \cos(\theta_t) \right] \quad (4.8)$$

Clearly, neither power injection expression depends on θ_f since $\theta_{tf} = \theta_t - \theta_f = \theta_t$. Since no power (real or reactive) is generated at the “to” bus, the injected power expressions are simply equal to the negative of the power consumed at this bus. Therefore, the following is true:

$$P_t^L = -\left(P_t^{\text{inj}}\right) = V_t \left[\frac{G \cos(\theta_t) + B \sin(\theta_t)}{c} \right] - V_t^2 G$$

$$Q_t^L = -\left(Q_t^{\text{inj}}\right) = V_t^2 (B + \frac{B_{sh}}{2} + B_s) + V_t \left[\frac{G \sin(\theta_t) - B \cos(\theta_t)}{c} \right]$$

Rearranging both sides yields the following expressions.

$$P_t^L + V_t^2 G = \frac{V_t}{c} G \cos(\theta_t) + \frac{V_t}{c} B \sin(\theta_t)$$

$$Q_t^L - V_t^2 (B + \frac{B_{sh}}{2} + B_s) = \frac{V_t}{c} G \sin(\theta_t) - \frac{V_t}{c} B \cos(\theta_t)$$

Also, we can write the complex power of the load in the following way, where $\beta = \tan(\vartheta)$ is a power factor parameter and ϑ is the phase shift between the load voltage and current ($\theta_v - \theta_i$).

$$S_t^L = P_D(1 + j\beta) \quad (4.9)$$

Ultimately, we wish to solve for V_t explicitly. To eliminate the nonlinear trigonometric terms, we square both expressions (θ_t can be eliminated through the identity $\sin^2 \theta + \cos^2 \theta = 1$). We also write the active and reactive load demand in terms of P_D and β .

$$(P_D + V_t^2 G)^2 = \left(\frac{V_t}{c} G \cos(\theta_t) + \frac{V_t}{c} B \sin(\theta_t) \right)^2 \quad (4.10)$$

$$\left(\beta P_D - V_t^2 (B + \frac{B_{sh}}{2} + B_s) \right)^2 = \left(\frac{V_t}{c} G \sin(\theta_t) - \frac{V_t}{c} B \cos(\theta_t) \right)^2 \quad (4.11)$$

Computing the square of each side yields the following expanded expressions.

$$\begin{aligned} P_D^2 + V_t^4 G^2 + 2P_D V_t^2 G &= \frac{V_t^2}{c^2} G^2 \cos^2(\theta_t) + \frac{V_t^2}{c^2} B^2 \sin^2(\theta_t) + 2 \frac{V_t^2}{c^2} BG \sin(\theta_t) \cos(\theta_t) \\ \beta^2 P_D^2 + V_t^4 (B + \frac{B_{sh}}{2} + B_s)^2 - 2\beta P_D V_t^2 (B + \frac{B_{sh}}{2} + B_s) &= \frac{V_t^2}{c^2} G^2 \sin^2(\theta_t) + \frac{V_t^2}{c^2} B^2 \cos^2(\theta_t) - 2 \frac{V_t^2}{c^2} BG \sin(\theta_t) \cos(\theta_t) \end{aligned}$$

Both of these equations can now be summed together. As shown, the final terms cancel out and the expression simplifies.

$$\begin{aligned} P_D^2 + V_t^4 G^2 + 2P_D V_t^2 G + \beta^2 P_D^2 + V_t^4 (B + \frac{B_{sh}}{2} + B_s)^2 - 2\beta P_D V_t^2 (B + \frac{B_{sh}}{2} + B_s) \\ = \frac{V_t^2}{c^2} G^2 \cos^2(\theta_t) + \frac{V_t^2}{c^2} B^2 \sin^2(\theta_t) + \frac{V_t^2}{c^2} G^2 \sin^2(\theta_t) + \frac{V_t^2}{c^2} B^2 \cos^2(\theta_t) \\ + 2 \frac{V_t^2}{c^2} BG \sin(\theta_t) \cos(\theta_t) - 2 \frac{V_t^2}{c^2} BG \sin(\theta_t) \cos(\theta_t) \\ = \frac{V_t^2}{c^2} G^2 (\cos^2(\theta_t) + \sin^2(\theta_t)) + \frac{V_t^2}{c^2} B^2 (\sin^2(\theta_t) + \cos^2(\theta_t)) \\ = \frac{V_t^2}{c^2} G^2 + \frac{V_t^2}{c^2} B^2 \\ = \frac{V_t^2}{c^2} (G^2 + B^2) \end{aligned}$$

We can bring all terms onto the left side of the equation and thus set the expression equal to 0. The equation is flipped around and like terms can be grouped.

$$\begin{aligned}
 0 &= P_D^2 + V_t^4 G^2 + 2P_D V_t^2 G + \beta^2 P_D^2 + V_t^4 \left(B + \frac{B_{sh}}{2} + B_s \right)^2 - 2\beta P_D V_t^2 \left(B + \frac{B_{sh}}{2} + B_s \right) - \frac{V_t^2}{c^2} (G^2 + B^2) \\
 &= V_t^4 \left[G^2 + \left(B + \frac{B_{sh}}{2} + B_s \right)^2 \right] + V_t^2 \left[2P_D G - 2\beta P_D \left(B + \frac{B_{sh}}{2} + B_s \right) - \frac{G^2 + B^2}{c^2} \right] + V_t^0 \left[P_D^2 + \beta^2 P_D^2 \right] \\
 &= V_t^4 [a] + V_t^2 [b] + V_t^0 [c]
 \end{aligned}$$

Since coefficients a , b , and c are known, the square root of the quadratic equation can be used to solve for the magnitude of the “to” bus voltage.

Appendix D: Quantifying Load Noise via Second Order Delta Method

We consider variable X and a function of this variable, $g(X)$, as is done in section 1.2.8.

$$\begin{aligned} g(X) &\approx g(\mu_X) + g'(\mu_X)(X - \mu_X) + \frac{g''(\mu_X)}{2}(X - \mu_X)^2 \\ &\approx g(\mu_X) + g'(\mu_X)X - g'(\mu_X)\mu_X + \frac{g''(\mu_X)}{2}(X^2 + \mu_X^2 - 2X\mu_X) \\ &\approx X \left(\left(\frac{g''(\mu_X)}{2} \right) X + (g'(\mu_X) - g''(\mu_X)\mu_X) \right) + \left(g(\mu_X) + \frac{g''(\mu_X)}{2}\mu_X^2 - g'(\mu_X)\mu_X \right) \end{aligned}$$

We can take the variance of both sides.

$$\begin{aligned} \text{Var}(g(X)) &\approx \text{Var}X \left(\left(\left(\frac{g''(\mu_X)}{2} \right) X + (g'(\mu_X) - g''(\mu_X)\mu_X) \right) + \left(g(\mu_X) + \frac{g''(\mu_X)}{2}\mu_X^2 - g'(\mu_X)\mu_X \right) \right) \\ &\approx \text{Var} \left(X \left(\left(\frac{g''(\mu_X)}{2} \right) X + (g'(\mu_X) - g''(\mu_X)\mu_X) \right) \right) \end{aligned}$$

The problem can now be reformulated.

$$\text{Var} \left(X \left(\left(\frac{g''(\mu_X)}{2} \right) X + (g'(\mu_X) - g''(\mu_X)\mu_X) \right) \right) = \text{Var}(X(aX + b))$$

Where we have made the following substitutions:

$$a = \left(\frac{g''(\mu_X)}{2} \right)$$

$$b = (g'(\mu_X) - g''(\mu_X)\mu_X)$$

We must remember that the expectation operator is a linear operator:

$$\mathbb{E}((aX + b)) = a\mathbb{E}(X) + b$$

We can now compute this variance:

$$\begin{aligned}\text{Var}(X(aX + b)) &= \mathbb{E}\left((X(aX + b))^2\right) - \mathbb{E}(X(aX + b))^2 \\ &= \mathbb{E}\left(X^2(a^2X^2 + b^2 + 2abX)\right) - \mathbb{E}(aX^2 + bX)^2 \\ &= \mathbb{E}(a^2X^4) + \mathbb{E}(b^2X^2) + \mathbb{E}(2abX^3) - (\mathbb{E}(X^2) + b\mathbb{E}(X))^2 \\ &= a^2\mathbb{E}(X^4) + b^2\mathbb{E}(X^2) + 2ab\mathbb{E}(X^3) - (\mathbb{E}(X^2) + b\mathbb{E}(X))^2\end{aligned}$$

Each of these can now be computed. Initially, we only know the following values: $\mathbb{E}(X)$ and $\text{Var}(X)$.

Using just these values, all of the moments of X can be determined (this is true for a Gaussian Distribution).

$$\mathbb{E}(X) = \mathbb{E}(X)$$

$$\mathbb{E}(X^2) = \mathbb{E}(X)^2 + \text{Var}(X)$$

$$\mathbb{E}(X^3) = \mathbb{E}(X)^3 + 3\mathbb{E}(X)\text{Var}(X)$$

$$\mathbb{E}(X^4) = \mathbb{E}(X)^4 + 6\mathbb{E}(X)^2\text{Var}(X) + 3\text{Var}(X)^2$$

This final expression for the variance is arrived at:

$$\begin{aligned}\text{Var}(X(aX + b)) &= a^2\left(\mathbb{E}(X)^4 + 6\mathbb{E}(X)^2\text{Var}(X) + 3\text{Var}(X)^2\right) \\ &\quad + b^2(\mathbb{E}(X)^2 + \text{Var}(X)) \\ &\quad + 2ab(\mathbb{E}(X)^3 + 3\mathbb{E}(X)\text{Var}(X)) \\ &\quad - (a(\mathbb{E}(X)^2 + \text{Var}(X)) + b\mathbb{E}(X))^2\end{aligned}$$

It shall now be shown how this can be used to quantify the noise of a load. In this expression, the variables a and b were defined in the following way:

$$a = \frac{g''(\mu_X)}{2}$$

$$b = g'(\mu_X) - g''(\mu_X)\mu_X$$

We can write these equations in terms of load power variance and bus voltage variance, where we have the function $V_t = g(P_D)$ (written using simplified notation). The base load value is μ_P and the variance of the load power is σ_P^2 . We redefine a and b

$$a = \frac{g''(\mu_P)}{2}$$

$$b = g'(\mu_P) - g''(\mu_P)\mu_P$$

With this clarification, we can move forward with the variance calculation.

$$\begin{aligned} \sigma_{V_t}^2 &= \text{Var}(P_D(aP_D + b)) \\ &= a^2(\mu_P^4 + 6\mu_P^2\sigma_P^2 + 3\sigma_P^4) + b^2(\mu_P^2 + \sigma_P^2) \\ &\quad + 2ab(\mu_P^3 + 3\mu_P\sigma_P^2) - (a(\mu_P^2 + \sigma_P^2) + b\mu_P)^2 \\ &= a^2\mu_P^4 + a^26\mu_P^2\sigma_P^2 + a^23\sigma_P^4 + b^2\mu_P^2 + b^2\sigma_P^2 \\ &\quad + 2ab\mu_P^3 + 6ab\mu_P\sigma_P^2 - (a\mu_P^2 + a\sigma_P^2 + b\mu_P)^2 \\ &= a^2\mu_P^4 + a^26\mu_P^2\sigma_P^2 + a^23\sigma_P^4 + b^2\mu_P^2 + b^2\sigma_P^2 \\ &\quad + 2ab\mu_P^3 + 6ab\mu_P\sigma_P^2 - a^2\mu_P^4 - a^2\sigma_P^4 - b^2\mu_P^2 \\ &\quad - 2a^2\mu_P^2\sigma_P^2 - 2a\sigma_P^2b\mu_P - 2ab\mu_P^3 \\ &= (2a^2)\sigma_P^4 + (a^26\mu_P^2 + b^2 + 6ab\mu_P - 2a^2\mu_P^2 - 2ab\mu_P)\sigma_P^2 \\ &\quad + (a^2\mu_P^4 + b^2\mu_P^2 + 2ab\mu_P^3 - a^2\mu_P^4 - b^2\mu_P^2 - 2ab\mu_P^3)\sigma_P^0 \end{aligned}$$

The voltage variance can be pulled to the other side.

$$\begin{aligned} 0 &= (2a^2)\sigma_P^4 + (a^26\mu_P^2 + b^2 + 6ab\mu_P - 2a^2\mu_P^2 - 2ab\mu_P)\sigma_P^2 \\ &\quad + (a^2\mu_P^4 + b^2\mu_P^2 + 2ab\mu_P^3 - a^2\mu_P^4 - b^2\mu_P^2 - 2ab\mu_P^3 - \sigma_{V_t}^2)\sigma_P^0 \\ &= (2a^2)\sigma_P^4 + (4a^2\mu_P^2 + b^2 + 4ab\mu_P)\sigma_P^2 + (-\sigma_{V_t}^2)\sigma_P^0 \end{aligned}$$

We employ the following symbols:

$$c_1 = (2a^2)$$

$$c_2 = (4a^2\mu_P^2 + b^2 + 4ab\mu_P)$$

$$c_3 = (-\sigma_V^2)$$

The quadratic formula can be used to solve for the variance of the load power

$$\sigma_P^2 = \frac{-(c_2) \pm \sqrt{(c_2)^2 - 4c_1c_2}}{2c_1} \quad (4.12)$$

Appendix E: Detailed Power System Model Overview

Algebraic Equations

A plethora of algebraic equations underlie the system \mathbf{g} . The most fundamental algebraic equations, though, are the power flow equations. Loads at each load bus are modeled by the two power flow equations of (1.16) and (1.17).

$$P_i = V_i \sum_{k=1}^N V_k [G_{i,k} \cos(\theta_{i,k}) + B_{i,k} \sin(\theta_{i,k})] \quad i \in \mathcal{N}$$

$$Q_i = V_i \sum_{k=1}^N V_k [G_{i,k} \sin(\theta_{i,k}) - B_{i,k} \cos(\theta_{i,k})] \quad i \in \mathcal{N}$$

The load magnitudes have a slight frequency dependence. The algebraic variable $\Delta\omega$, which is the frequency deviation at bus i , is computed as follows.

$$\Delta\omega = x_f + \frac{1}{2\pi f_n} \frac{1}{T_F} (\theta - \theta^0) \quad (4.13)$$

The variable x_f is a filter state variable (reviewed below). The variable $\Delta\omega$ is in turn used to calculate the active and reactive power demand at bus i .

$$p = p^0 (1 + \Delta\omega)^{\beta_p} \quad (4.14)$$

$$q = q^0 (1 + \Delta\omega)^{\beta_q} \quad (4.15)$$

Power injections at the generator bus are also modeled by the power flow equations, but many other algebraic equations are necessary to model the generator dynamics. We review the most fundamental

ones which incorporate the algebraic variables of \mathbf{y} . At generator bus i , the following two equations relate the bus voltage V and the q-axis and d-axis machine voltages (for notational simplicity, each given variable corresponds to the variable at bus i).¹

$$v_d = V \sin(\delta - \theta) \quad (4.16)$$

$$v_q = V \cos(\delta - \theta) \quad (4.17)$$

The variables v_d and v_q are then used to relate the q-axis and d-axis currents to the active and reactive powers of the machine.

$$p = v_d i_d + v_q i_q \quad (4.18)$$

$$q = v_q i_d - v_d i_q \quad (4.19)$$

The mechanical power and voltage reference algebraic variables are held at their respective set points.

$$0 = p_m^0 - p_m \quad (4.20)$$

$$0 = v_f^0 - v_f \quad (4.21)$$

Two algebraic equations are needed to relate the algebraic variables of the TG.

$$0 = p_m - p_m^{\text{syn}} \quad (4.22)$$

$$0 = \omega_{\text{ref}}^0 - \omega_{\text{ref}} \quad (4.23)$$

And finally, two more algebraic equations relate the algebraic variables of the AVR.

$$0 = v_f - v_f^{\text{syn}} \quad (4.24)$$

$$0 = v_{\text{ref}}^0 - v_{\text{ref}} \quad (4.25)$$

Of course, none of the active feedback equations are given, but we can now populate the vector \mathbf{y}

¹If the reader is unfamiliar with these models, variable definitions for these equations are presented in [28].

with all of the algebraic variables of the system, each of which is given above.

$$\mathbf{y} = \begin{bmatrix} \Delta\omega \\ \theta \\ \mathbf{V} \\ \mathbf{P} \\ \vdots \\ \mathbf{v}_{\text{ref}} \end{bmatrix} \quad (4.26)$$

Differential Equations

A series of 13 differential equations (reviewed below) are needed to model the generator and load dynamics. The equation governing the stochastic load fluctuation variable u is given by (2.15). The relationships between u and the simulated active/reactive load values are given by (3.19) and (3.20). This model is not defined in PSAT and therefore was added manually.

$$\dot{u} = -Eu + \xi \quad (4.27)$$

While u determines the noise of the loads due to stochastic demand, the load levels at each bus in the system are also given a slight frequency dependence, where T_F is a filter time constant (to reiterate, all variables incorporated in the following differential equations are defined in [28]).

$$\dot{x}_f = -\frac{\Delta\omega}{T_F} \quad (4.28)$$

The filter state variable x_f determines the frequency deviation $\Delta\omega$, as previously stated. Four differential equations model the SG dynamics. These equations relate the dynamics of the rotor angle, the rotor frequency, the q-axis transient voltage, and the d-axis transient voltage. It is important to remember that δ is the angle of the rotor with respect to a synchronously rotating

reference frame.

$$\dot{\delta} = \Omega_b (\omega - \omega_0) \quad (4.29)$$

$$\dot{\omega} = \frac{p_m - p_e - D(\omega - \omega_0)}{M} \quad (4.30)$$

$$\dot{e}'_q = \frac{-f_s e'_q - (x_d - x'_d) i_d + v_f^*}{T'_{d0}} \quad (4.31)$$

$$\dot{e}'_d = \frac{-e'_d + (x_q - x'_q) i_q}{T'_{q0}} \quad (4.32)$$

Three differential equations model the TG dynamics. These equations govern the feedback loop implementing droop frequency control.

$$\dot{x}_{g1} = \frac{p_{in} - x_{g1}}{T_s} \quad (4.33)$$

$$\dot{x}_{g2} = \frac{\left(1 - \frac{T_3}{T_c}\right) x_{g1} - x_{g2}}{T_c} \quad (4.34)$$

$$\dot{x}_{g3} = \frac{\left(1 - \frac{T_4}{T_5}\right) \left(x_{g2} + \frac{T_3}{T_c} x_{g1}\right) - x_{g3}}{T_5} \quad (4.35)$$

Four differential equations model the AVR dynamics. These equations govern the feedback loop implementing voltage control.

$$\dot{v}_m = \frac{V - v_m}{T_r} \quad (4.36)$$

$$\dot{v}_{r1} = \frac{K_a \left(v_{ref} - v_m - v_{r2} - \frac{K_f}{T_f} v_f\right) - v_{r1}}{T_a} \quad (4.37)$$

$$\dot{v}_{r2} = \frac{-\left(\frac{K_f}{T_f} v_f + v_{r2}\right)}{T_f} \quad (4.38)$$

$$\dot{v}_f = \frac{-(v_f (K_e + S_e(v_f)) - v_r)}{T_e} \quad (4.39)$$

We then populate the vector \mathbf{x} with all of the state variables of the system (except for u , which is

an independent input).

$$\mathbf{x} = \begin{bmatrix} \mathbf{x}_f \\ \boldsymbol{\delta} \\ \boldsymbol{\omega} \\ \mathbf{e}'_q \\ \vdots \\ \mathbf{v}_f \end{bmatrix} \quad (4.40)$$

Appendix F: Line Current Covariance Matrix

To compute the line current covariance matrix (which may be translated into a correlation matrix), we must begin with basic circuit analysis of the Pi Equivalent Circuit Model shown in Figure 1.1. Because all state variables are known and the system is fully characterized, we can use the voltage phasors and admittance values to solve for the current phasor $\tilde{I}_{t,f}$. Initially we use the voltage on the secondary side of the transformer \tilde{V}'_f which is then transformed into the voltage on the primary side \tilde{V}_f .

$$\tilde{I}_{f,t} = \left(\tilde{V}'_f \right) j \frac{B_{f,t}}{2} + \left(\tilde{V}'_f - \tilde{V}_t \right) |\tilde{y}_{f,t}| e^{j\phi_{f,t}} \quad (4.41)$$

\Downarrow

$$\tilde{I}_{f,t} = \left(\frac{\tilde{V}_f}{\tilde{c}} \right) j \frac{B_{f,t}}{2} + \left(\frac{\tilde{V}_f}{\tilde{c}} - \tilde{V}_t \right) |\tilde{y}_{f,t}| e^{j\phi_{f,t}}$$

The expression in (4.41) can rearranged such that the voltage terms are grouped separately.

$$\tilde{I}_{f,t} = \left(\frac{\tilde{V}_f}{\tilde{c}} \right) \left(j \frac{B_{f,t}}{2} + |\tilde{y}_{f,t}| e^{j\phi_{f,t}} \right) - \tilde{V}_t (|\tilde{y}_{f,t}| e^{j\phi_{f,t}}) \quad (4.42)$$

The expression in (4.42) can be written in terms of the expanded voltage phasors.

$$\tilde{I}_{f,t} = \left| \tilde{V}_f \right| e^{j\theta_f} \left(\frac{\left| \frac{B_{f,t}}{2} \right| e^{j\frac{\pi}{2}} + |\tilde{y}_{f,t}| e^{j\phi_{f,t}}}{\tilde{c}} \right) - \left| \tilde{V}_t \right| |\tilde{y}_{f,t}| e^{j(\theta_t + \phi_{f,t})} \quad (4.43)$$

Now we combine the admittance terms attached to $|\tilde{V}_f|$.

$$|\tilde{y}'| e^{j\phi'} = \frac{\left| \frac{B_{f,t}}{2} \right| e^{j\frac{\pi}{2}} + |\tilde{y}_{f,t}| e^{j\phi_{f,t}}}{|\tilde{c}| e^{j\Phi}} \quad (4.44)$$

Rewriting (4.43) yields a simplified expression.

$$\tilde{I}_{f,t} = \left| \tilde{V}_f \right| |\tilde{y}'| e^{j(\theta_f + \phi')} - \left| \tilde{V}_t \right| |\tilde{y}_{f,t}| e^{j(\theta_t + \phi_{f,t})} \quad (4.45)$$

Both sides of the current phasor expression can be divided by the angle associated with the first terms in equation (4.45).

$$\frac{\tilde{I}_{f,t}}{e^{j(\theta_f + \phi')}} = \left| \tilde{V}_f \right| |\tilde{y}'| - \left| \tilde{V}_t \right| |\tilde{y}_{f,t}| e^{j(\theta_t - \theta_f + \phi_{f,t} - \phi')} \quad (4.46)$$

Dividing by an angle simply shifts the phasor diagram of the current; it does not alter the current magnitude. In this case, we are investigating current magnitude variance, so we can shift the phasor all we want without affecting magnitude. We now define a new quantity $\tilde{I}'_{f,t}$. This value has the same magnitude as $\tilde{I}_{f,t}$ but a slightly shifted phase.

$$\tilde{I}'_{f,t} = \frac{\tilde{I}_{f,t}}{e^{j(\theta_f + \phi')}} \quad (4.47)$$

$$\left| \tilde{I}'_{f,t} \right| = \left| \tilde{I}_{f,t} \right| \quad (4.48)$$

An expression for $\tilde{I}'_{f,t}$ can now be written.

$$\tilde{I}'_{f,t} = \left| \tilde{V}_f \right| |\tilde{y}'| - \left| \tilde{V}_t \right| |\tilde{y}_{f,t}| e^{j(\theta_t - \theta_f + \phi_{f,t} - \phi')} \quad (4.49)$$

To gain a more intuitive sense for the problem, we can draw a triangle which relates the three separate terms in (4.49).

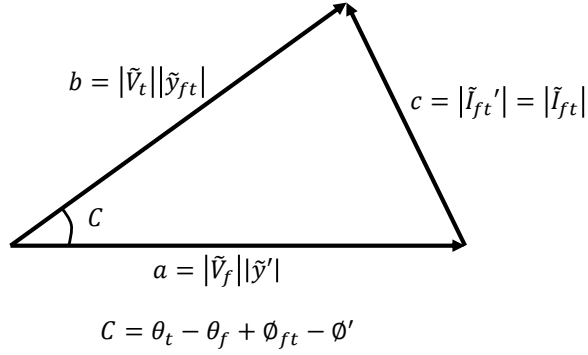


Figure 4.1: The relationship between the current vectors is shown. Three magnitudes and one angle are known. Clearly, the magnitude of the current depends on four dynamic variables: V_f , V_t , θ_f , and θ_t . The values of ϕ_{ft} and ϕ' are static.

In order to determine the change in current magnitude, we employ trigonometric identities which directly relate changes in V_f , V_t , θ_f , and θ_t to changes in $|\tilde{I}_{f,t}|$. The law of cosines can be employed for this purpose, as it relates three magnitudes and an angle of any sort of triangle. The law of cosines is given in (4.50), with magnitudes a , b , and c and angle C given in Figure (4.1).

$$c^2 = a^2 + b^2 - 2ab \cos C \quad (4.50)$$

Since the current magnitude is equal to the variable c in (4.50), we must take the implicit derivative of the function with respect to a , b , and C

$$\begin{aligned} \frac{\partial}{\partial a} c^2 &= 2c \frac{\partial c}{\partial a} = 2a - 2b \cos C \\ \frac{\partial c}{\partial a} &= \frac{a - b \cos C}{c} \end{aligned} \quad (4.51)$$

The same computation can be done for b

$$\begin{aligned} \frac{\partial}{\partial b} c^2 &= 2c \frac{\partial c}{\partial b} = 2b - 2a \cos C \\ \frac{\partial c}{\partial b} &= \frac{b - a \cos C}{c} \end{aligned} \quad (4.52)$$

And finally, this can be completed for angle C

$$\frac{\partial}{\partial C} c^2 = 2c \frac{\partial c}{\partial C} = 2ab \sin C$$

$$\frac{\partial c}{\partial C} = \frac{ab \sin C}{c} \quad (4.53)$$

All of these derivative equations can be extended to the current, voltage, and admittance values of the triangle in (4.1). Again, admittance values do not effectively change, so at all times, $|\tilde{y}'|$ and $|\tilde{y}_{ft}|$ are constant. This fact is reflected in the simplified derivative terms given below.

$$\frac{\partial |\tilde{I}_{f,t}|}{\partial |\tilde{V}_f|} = \frac{|\tilde{y}'| (\left| \tilde{V}_f \right| |\tilde{y}'| - \left| \tilde{V}_t \right| |\tilde{y}_{ft}| \cos(\theta_t - \theta_f + \phi_{f,t} - \phi'))}{\left| \tilde{I}_{f,t} \right|} \quad (4.54)$$

$$\frac{\partial |\tilde{I}_{f,t}|}{\partial |\tilde{V}_t|} = \frac{|\tilde{y}_{ft}| (\left| \tilde{V}_t \right| |\tilde{y}_{ft}| - \left| \tilde{V}_f \right| |\tilde{y}'| \cos(\theta_t - \theta_f + \phi_{f,t} - \phi'))}{\left| \tilde{I}_{f,t} \right|} \quad (4.55)$$

$$\frac{\partial |\tilde{I}_{f,t}|}{\partial \theta_f} = \frac{-\left| \tilde{V}_f \right| |\tilde{y}'| \left| \tilde{V}_t \right| |\tilde{y}_{ft}| \sin(\theta_t - \theta_f + \phi_{f,t} - \phi')}{\left| \tilde{I}_{f,t} \right|} \quad (4.56)$$

$$\frac{\partial |\tilde{I}_{f,t}|}{\partial \theta_t} = \frac{\left| \tilde{V}_f \right| |\tilde{y}'| \left| \tilde{V}_t \right| |\tilde{y}_{ft}| \sin(\theta_t - \theta_f + \phi_{f,t} - \phi')}{\left| \tilde{I}_{f,t} \right|} \quad (4.57)$$

As previously stated, the law of cosines gives an equation for the current magnitude.

$$|\tilde{I}_{f,t}|^2 = (\left| \tilde{V}_f \right| |\tilde{y}'|)^2 + (\left| \tilde{V}_t \right| |\tilde{y}_{ft}|)^2 - 2 (\left| \tilde{V}_f \right| |\tilde{y}'|) (\left| \tilde{V}_t \right| |\tilde{y}_{ft}|) \cos(\theta_t - \theta_f + \phi_{f,t} - \phi')$$

This expression can be square rooted and then written as a function h .

$$|\tilde{I}_{f,t}| = h(V_f, \theta_f, V_t, \theta_t) \quad (4.58)$$

Once again, the first two terms of the multivariate Taylor Series Expansion can be used to find the sensitivity of the current magnitude with respect to voltage magnitudes and voltage phases. We will linearize about the steady state operating point (i.e. $V_f, \theta_f, V_t, \theta_t$) and solve for the sensitivity of the current magnitude. Voltage and current magnitudes will now be written as true magnitudes instead of absolute values of phasors.

$$|\tilde{I}_{f,t}| = I_{f,t} \approx I_{f,t} \Big|_{V_f, \theta_f, V_t, \theta_t} + \frac{\partial I_{f,t}}{\partial V_f} \Delta V_f + \frac{\partial I_{f,t}}{\partial \theta_f} \Delta \theta_f + \frac{\partial I_{f,t}}{\partial V_t} \Delta V_t + \frac{\partial I_{f,t}}{\partial \theta_t} \Delta \theta_t \quad (4.59)$$

Now, the LHS can be perturbed, and $I_{f,t} \Big|_{V_f, \theta_f, V_t, \theta_t}$ can be subtracted from both sides to yield the current magnitude sensitivity. The partials also can be evaluated.

$$\begin{aligned}\Delta I_{f,t} &= \frac{V_f (y')^2 - V_t y' y_{f,t} \cos(\theta_t - \theta_f + \phi_{f,t} - \phi')}{I_{f,t}} \Delta V_f - \frac{V_f y' V_t y_{f,t} \sin(\theta_t - \theta_f + \phi_{f,t} - \phi')}{I_{f,t}} \Delta \theta_f \\ &\quad \frac{V_t (y_{f,t})^2 - V_f y_{f,t} y' \cos(\theta_t - \theta_f + \phi_{f,t} - \phi')}{I_{f,t}} \Delta V_t + \frac{V_f y' V_t y_{f,t} \sin(\theta_t - \theta_f + \phi_{f,t} - \phi')}{I_{f,t}} \Delta \theta_t\end{aligned}\quad (4.60)$$

Writing 4.60 as an inner product yields the following expression.

$$\Delta I_{f,t} = \begin{bmatrix} \frac{\partial I_{f,t}}{\partial V_f} & \frac{\partial I_{f,t}}{\partial \theta_f} & \frac{\partial I_{f,t}}{\partial V_t} & \frac{\partial I_{f,t}}{\partial \theta_t} \end{bmatrix} \begin{bmatrix} \Delta V_f \\ \Delta \theta_f \\ \Delta V_t \\ \Delta \theta_t \end{bmatrix} \quad (4.61)$$

As expressed in (4.26), the algebraic variables contained in \mathbf{y} contain all necessary values of V and θ , so the change in the algebraic variables will be equivalent to $\Delta \mathbf{y}$. Using the function h defined in (4.58) along with $\Delta \mathbf{y}$, the current differential can be written more compactly:

$$\Delta I_{f,t} = \begin{bmatrix} h_{V_f} & h_{\theta_f} & h_{V_t} & h_{\theta_t} \end{bmatrix} [\Delta \mathbf{y}] \quad (4.62)$$

Finally, we vectorize the expression in (4.62) and generalize for the entire system.

$$\Delta \mathbf{I}_{f,t} = \begin{bmatrix} \mathbf{h}_{V_f} & \mathbf{h}_{\theta_f} & \mathbf{h}_{V_t} & \mathbf{h}_{\theta_t} \end{bmatrix} [\Delta \mathbf{y}] \quad (4.63)$$

Assuming we have already solved for the covariance matrices $\sigma_{\mathbf{z}}^2$ and $\sigma_{\mathbf{y}}^2$, then we can use a transformation based on (4.62) to solve for $\sigma_{\mathbf{I}_{f,t}}^2$.

$$\sigma_{\mathbf{I}_{f,t}}^2 = \left[\mathbf{h}_{V_f} \quad \mathbf{h}_{\theta_f} \quad \mathbf{h}_{V_t} \quad \mathbf{h}_{\theta_t} \right] \sigma_{\mathbf{y}}^2 \left[\mathbf{h}_{V_f} \quad \mathbf{h}_{\theta_f} \quad \mathbf{h}_{V_t} \quad \mathbf{h}_{\theta_t} \right]^{\top} \quad (4.64)$$

Appendix G: Solving CPF via HELM with Configurable Loading Rates

We first restate the embedded power flow equation which is applied at each load bus.

$$\sum_{k=1}^N Y_{i,k} V_k(s) = \frac{S_i^* + s k_i S_i^*}{V_i^*(s^*)} \quad i\epsilon \text{PQ} \quad (4.65)$$

Again, the parameter k_i is a loading rate parameter, and it can be positive, negative, or 0. It corresponds the rate at which a bus will be loaded. We demonstrate the usefulness of this updated PQ bus equation by first calculating its germ ($s = 0$) solution.

$$\begin{aligned} \sum_{k=1}^N Y_{i,k} (V_k[0] + 0V_k[1] + 0^2 V_k[2] + \dots) &= \frac{S_i^* + 0 k_i S_i^*}{(V_i[0] + 0V_i[1] + 0^2 V_i[2] + \dots)^*} \quad i\epsilon \text{PQ} \\ &\Downarrow \\ \sum_{k=1}^N Y_{i,k} V_k[0] &= \frac{S_i^*}{V_i^*[0]} \quad i\epsilon \text{PQ} \end{aligned} \quad (4.66)$$

Assuming we have already used HELM to solve the power flow problem, these base case loading voltages are already known and we can solve for the $s = 0$ loading condition coefficients. This condition corresponds to the base case with no additional loading. In order to solve for the proceeding

coefficients, we set $W[s] = \frac{1}{V[s]}$ and we expand the notation.

$$\begin{aligned} \sum_{k=1}^N Y_{i,k} (V_k[0] + V_k[1]s + V_k[2]s^2 + \dots) &= S_i^* (W_i^*[0] + sW_i^*[1] + s^2W_i^*[2] \dots) \\ &\quad + sk_i S_i^* (W_i^*[0] + sW_i^*[1] + s^2W_i^*[2] \dots) \end{aligned} \quad (4.67)$$

We now equate the like coefficients of s^n .

$$\sum_{k=1}^N Y_{i,k} V_k[0] = S_i^* W_i^*[0] \quad (4.68)$$

$$\sum_{k=1}^N Y_{i,k} V_k[1] = S_i^* W_i^*[1] + k_i S_i^* W_i^*[0] \quad (4.69)$$

$$\sum_{k=1}^N Y_{i,k} V_k[2] = S_i^* W_i^*[2] + k_i S_i^* W_i^*[1] \quad (4.70)$$

⋮

These expressions (aside from the germ solution) can be generalized in the following way.

$$\sum_{k=1}^N Y_{i,k} V_k[n] = S_i^* W_i^*[n] + k_i S_i^* W_i^*[n-1] \quad n > 0 \quad (4.71)$$

This expression is problematic, as $V[n]$ depends on both $W[n-1]$ and $W[n]$, and $W[n]$ depends on $V[n]$. To solve this problem, we first bring the term multiplied by $W[n]$ to the LHS of (4.71).

$$\sum_{k=1}^N Y_{i,k} V_k[n] - S_i^* W_i^*[n] = k_i S_i^* W_i^*[n-1] \quad n > 0 \quad (4.72)$$

Next, we solve for the coefficients of $W(s) = \frac{1}{V(s)}$ in the following way. We first multiply through by $V(s)$.

$$\begin{aligned} 1 &= W(s)V(s) \\ &= [W[0] + sW[1] + s^2W[2] + \dots] [V[0] + sV[1] + s^2V[2] + \dots] \\ &= W[0]V[0] + (W[0]V[1] + W[1]V[0])s + (W[0]V[2] + W[1]V[1] + W[2]V[0])s^2 + \dots \end{aligned} \quad (4.73)$$

We equate coefficients with like powers of s on the LHS and the RHS of (4.73).

$$\begin{aligned} W[0]V[0] = 1 &\Rightarrow W[0] = \frac{1}{V[0]} \\ W[0]V[1] + W[1]V[0] = 0 &\Rightarrow W[1] = -\frac{W[0]V[1]}{V[0]} \\ W[0]V[2] + W[1]V[1] + W[2]V[0] = 0 &\Rightarrow W[2] = -\frac{W[0]V[2] + W[1]V[1]}{V[0]} \end{aligned}$$

This pattern can be generalized for $n > 0$.

$$W[n] = -\frac{\sum_{k=0}^{n-1} W[k]V[n-k]}{V[0]} \quad n \geq 1 \quad (4.74)$$

We plug (4.74) into (4.72).

$$\begin{aligned} \sum_{k=1}^N Y_{i,k} V_k[n] + S_i^* \left(\frac{\sum_{k=0}^{n-1} W_i[k]V_i[n-k]}{V_i[0]} \right)^* &= k_i S_i^* W_i^*[n-1] \quad n > 0 \\ \Downarrow \\ \sum_{k=1}^N Y_{i,k} V_k[n] + S_i^* \left(\frac{W_i[0]V_i[n] + W_i[1]V_i[n-1] + \cdots + W_i[n-1]V_i[1]}{V_i[0]} \right)^* &= k_i S_i^* W_i^*[n-1] \quad n > 0 \\ \Downarrow \\ \sum_{k=1}^N Y_{i,k} V_k[n] + S_i^* \left(V_i[n] \frac{W_i[0]}{V_i[0]} + \frac{W_i[1]V_i[n-1] + \cdots + W_i[n-1]V_i[1]}{V_i[0]} \right)^* &= k_i S_i^* W_i^*[n-1] \quad n > 0 \\ \Downarrow \\ \sum_{k=1}^N Y_{i,k} V_k[n] + (V_i[n])^* S_i^* \left(\frac{W_i[0]}{V_i[0]} \right)^* + S_i^* \left(\frac{W_i[1]V_i[n-1] + \cdots + W_i[n-1]V_i[1]}{V_i[0]} \right)^* &= k_i S_i^* W_i^*[n-1] \quad n > 0 \end{aligned} \quad (4.75)$$

We can make the following (generalized) simplification:

$$\frac{W_i[1]V_i[n-1] + \cdots + W_i[n-1]V_i[1]}{V_i[0]} = \frac{\sum_{k=1}^{n-1} W_i[k]V_i[n-k]}{V_i[0]} \quad (4.76)$$

We can substitute the simplification of (4.76) into (4.75).

$$\begin{aligned}
& \sum_{k=1}^N Y_{i,k} V_k[n] + (V_i[n])^* S_i^* \left(\frac{W_i[0]}{V_i[0]} \right)^* + S_i^* \left(\frac{\sum_{k=1}^{n-1} W_i[k] V_i[n-k]}{V_i[0]} \right)^* = k_i S_i^* W_i^*[n-1] \quad n > 0 \\
& \Downarrow \\
& \sum_{k=1}^N Y_{i,k} V_k[n] + (V_i[n])^* S_i^* \left(\frac{W_i[0]}{V_i[0]} \right)^* = k_i S_i^* W_i^*[n-1] - S_i^* \left(\frac{\sum_{k=1}^{n-1} W_i[k] V_i[n-k]}{V_i[0]} \right)^* \quad n > 0 \quad (4.77)
\end{aligned}$$

In order to solve this problem, we set up a linear system of equations where the unknown value is always the n^{th} voltage coefficient. In (4.77), there are two unknown coefficient values at each recursive step: $V_k[n]$ and $V_i[n]$. Because the complex conjugate of $V_i[n]$ is taken though, we must break the equation voltage coefficients into real and imaginary parts. This is done for the LHS of (4.77).

$$\begin{aligned}
\sum_{k=1}^N Y_{i,k} V_k[n] + (V_i[n])^* S_i^* \left(\frac{W_i[0]}{V_i[0]} \right)^* &= \sum_{k=1}^N (G_{i,k} + jB_{i,k}) (\Re \{V_k[n]\} + j\Im \{V_k[n]\}) + (V_i[n])^* S_i^* \left(\frac{W_i[0]}{V_i[0]} \right)^* \\
&= \sum_{k=1}^N (G_{i,k} \Re \{V_k[n]\} + jB_{i,k} \Re \{V_k[n]\} - B_{i,k} \Im \{V_k[n]\} + jG_{i,k} \Im \{V_k[n]\}) \\
&\quad + (V_i[n])^* S_i^* \left(\frac{W_i[0]}{V_i[0]} \right)^* \\
&= \sum_{k=1}^N ([G_{i,k} \Re \{V_k[n]\} - B_{i,k} \Im \{V_k[n]\}] + j [B_{i,k} \Re \{V_k[n]\} + G_{i,k} \Im \{V_k[n]\}]) \\
&\quad + (V_i[n])^* S_i^* \left(\frac{W_i[0]}{V_i[0]} \right)^*
\end{aligned}$$

We make the following observation concerning the final LHS term of (4.77).

$$(V_i[n])^* S_i^* \left(\frac{W_i[0]}{V_i[0]} \right)^* = \Re \left(V_i[n]^* S_i^* \left(\frac{W_i[0]}{V_i[0]} \right)^* \right) + j\Im \left(V_i[n]^* S_i^* \left(\frac{W_i[0]}{V_i[0]} \right)^* \right)$$

Now we can restate (4.77) with the LHS being broken up into real and imaginary components.

$$\begin{aligned}
& \sum_{k=1}^N ([G_{i,k} \Re \{V_k[n]\} - B_{i,k} \Im \{V_k[n]\}] + j [B_{i,k} \Re \{V_k[n]\} + G_{i,k} \Im \{V_k[n]\}]) \\
& \quad + \Re \left(V_i[n]^* S_i^* \left(\frac{W_i[0]}{V_i[0]} \right)^* \right) + j\Im \left(V_i[n]^* S_i^* \left(\frac{W_i[0]}{V_i[0]} \right)^* \right) \\
&= k_i S_i^* W_i^*[n-1] - S_i^* \left(\frac{\sum_{k=1}^{n-1} W_i[k] V_i[n-k]}{V_i[0]} \right)^* \quad n > 0
\end{aligned}$$

This expression is split into real and imaginary components by splitting up the RHS.

$$\begin{aligned}
& \sum_{k=1}^N \left([G_{i,k} \Re \{V_k[n]\} - B_{i,k} \Im \{V_k[n]\}] \right) + \Re \left(V_i[n]^* S_i^* \left(\frac{W_i[0]}{V_i[0]} \right)^* \right) \\
&= \Re(k_i S_i^* W_i^*[n-1]) - \Re \left(S_i^* \left(\frac{\sum_{k=1}^{n-1} W_i[k] V_i[n-k]}{V_i[0]} \right)^* \right) \quad n > 0 \\
& \sum_{k=1}^N \left([B_{i,k} \Re \{V_k[n]\} + G_{i,k} \Im \{V_k[n]\}] \right) + \Im \left(V_i[n]^* S_i^* \left(\frac{W_i[0]}{V_i[0]} \right)^* \right) \\
&= \Im(k_i S_i^* W_i^*[n-1]) - \Im \left(S_i^* \left(\frac{\sum_{k=1}^{n-1} W_i[k] V_i[n-k]}{V_i[0]} \right)^* \right) \quad n > 0
\end{aligned}$$

We pull out the complex conjugate operators on the LHS of the expressions.

$$\begin{aligned}
& \sum_{k=1}^N ([G_{i,k} \Re \{V_k[n]\} - B_{i,k} \Im \{V_k[n]\}]) + \Re \left(V_i[n] S_i \frac{W_i[0]}{V_i[0]} \right) \\
&= \Re(k_i S_i^* W_i^*[n-1]) - \Re \left(S_i^* \left(\frac{\sum_{k=1}^{n-1} W_i[k] V_i[n-k]}{V_i[0]} \right)^* \right) \quad n > 0 \\
& \sum_{k=1}^N ([B_{i,k} \Re \{V_k[n]\} + G_{i,k} \Im \{V_k[n]\}]) - \Im \left(V_i[n] S_i \frac{W_i[0]}{V_i[0]} \right) \\
&= \Im(k_i S_i^* W_i^*[n-1]) - \Im \left(S_i^* \left(\frac{\sum_{k=1}^{n-1} W_i[k] V_i[n-k]}{V_i[0]} \right)^* \right) \quad n > 0
\end{aligned}$$

We must manipulate the rightmost quantity on the LHS of the previous expressions in order to isolate $\Re(V_i[n])$ and $\Im(V_i[n])$ from $\Re \left(V_i[n] S_i \frac{W_i[0]}{V_i[0]} \right)$ and $\Im \left(V_i[n] S_i \frac{W_i[0]}{V_i[0]} \right)$ respectively. Ultimately, we wish to solve for the quantities $\Re(V[n])$ and $\Im(V[n])$, and this cannot be achieved until these quantities are isolated. We do so by leveraging the following property of complex algebra. Say we have complex values a and b . These can be expressed via rectangular, or Cartesian, coordinates.

$$a = x + jy$$

$$b = w + jz$$

We now take the real and imaginary components of their arithmetic product.

$$a \cdot b = (x + jy) \cdot (w + jz) = wx - yz + jyw + jzx$$

↓

$$\begin{aligned} \Re((x + jy) \cdot (w + jz)) &= wx - yz \\ &= \Re(a)\Re(b) - \Im(a)\Im(b) \end{aligned}$$

$$\begin{aligned} \Im((x + jy) \cdot (w + jz)) &= yw + zx \\ &= \Re(a)\Im(b) + \Re(b)\Im(a) \end{aligned}$$

We may apply this fact to the quantity in question.

$$\Re\left(V_i[n]S_i \frac{W_i[0]}{V_i[0]}\right) = \Re(V_i[n]) \Re\left(S_i \left(\frac{W_i[0]}{V_i[0]}\right)\right) - \Im(V_i[n]) \Im\left(S_i \left(\frac{W_i[0]}{V_i[0]}\right)\right)$$

$$\Im\left(V_i[n]S_i \frac{W_i[0]}{V_i[0]}\right) = \Im(V_i[n]) \Re\left(S_i \left(\frac{W_i[0]}{V_i[0]}\right)\right) + \Re(V_i[n]) \Im\left(S_i \left(\frac{W_i[0]}{V_i[0]}\right)\right)$$

↓

$$\begin{aligned} \sum_{k=1}^N ([G_{ik}\Re\{V_k[n]\} - B_{ik}\Im\{V_k[n]\}] + \Re(V_i[n]) \Re\left(S_i \left(\frac{W_i[0]}{V_i[0]}\right)\right) - \Im(V_i[n]) \Im\left(S_i \left(\frac{W_i[0]}{V_i[0]}\right)\right)) \\ = \Re(k_i S_i^* W_i^*[n-1]) - \Re\left(S_i^* \left(\frac{\sum_{k=1}^{n-1} W_i[k] V_i[n-k]}{V_i[0]}\right)^*\right) \quad n > 0 \end{aligned} \quad (4.78)$$

$$\begin{aligned} \sum_{k=1}^N ([B_{ik}\Re\{V_k[n]\} + G_{ik}\Im\{V_k[n]\}] - \Im(V_i[n]) \Re\left(S_i \left(\frac{W_i[0]}{V_i[0]}\right)\right) - \Re(V_i[n]) \Im\left(S_i \left(\frac{W_i[0]}{V_i[0]}\right)\right)) \\ = \Im(k_i S_i^* W_i^*[n-1]) - \Im\left(S_i^* \left(\frac{\sum_{k=1}^{n-1} W_i[k] V_i[n-k]}{V_i[0]}\right)^*\right) \quad n > 0 \end{aligned} \quad (4.79)$$

Now, the only unknown quantities are the n^{th} voltage coefficients. To gain some intuition, we formulate the problem with matrix notation. We start by defining the rectangular voltage vector

\mathbf{V}_R which has length $2m$, where $PQ = \{1...m\}$.

$$\mathbf{V}_R = \begin{bmatrix} \Re(V_1[n]) \\ \Im(V_1[n]) \\ \vdots \\ \Re(V_m[n]) \\ \Im(V_m[n]) \end{bmatrix} \quad (4.80)$$

Next, we define the altered $2m$ by $2m$ rectangular admittance matrix Y_R . It has the following member elements.

$$Y_{R_{i,j}} = \begin{cases} \Re(Y_{\frac{i+1}{2}, \frac{j+1}{2}}) & i, j \text{ odd} \\ -\Im(Y_{\frac{i+1}{2}, \frac{j}{2}}) & i \text{ odd, } j \text{ even} \\ \Im(Y_{\frac{i}{2}, \frac{j+1}{2}}) & i \text{ even, } j \text{ odd} \\ \Re(Y_{\frac{i}{2}, \frac{j}{2}}) & i = i, j \text{ even} \end{cases} \quad (4.81)$$

A sample of this matrix can be expanded and shown explicitly.

$$Y_R = \begin{bmatrix} \ddots & & & \ddots \\ & G_{i,j} & -B_{i,j} & \\ & B_{i,j} & G_{i,j} & \\ \ddots & & & \ddots \end{bmatrix} \quad (4.82)$$

In order to write the vectorized power balance expression for the entire system, we employ these matrices along with the vectors generated from generalizing (4.78) and (4.79) for every load bus in

the entire system (1 through m).

$$\begin{aligned}
Y_R \tilde{\mathbf{V}}_R + & \left[\begin{array}{c} \Re(V_1[n]) \Re\left(S_1\left(\frac{W_1[0]}{V_1[0]}\right)\right) \\ -\Im(V_1[n]) \Re\left(S_1\left(\frac{W_1[0]}{V_1[0]}\right)\right) \\ \vdots \\ \Re(V_m[n]) \Re\left(S_m\left(\frac{W_m[0]}{V_m[0]}\right)\right) \\ -\Im(V_m[n]) \Re\left(S_m\left(\frac{W_m[0]}{V_m[0]}\right)\right) \end{array} \right] - \left[\begin{array}{c} \Im(V_1[n]) \Im\left(S_1\left(\frac{W_1[0]}{V_1[0]}\right)\right) \\ \Re(V_1[n]) \Im\left(S_1\left(\frac{W_1[0]}{V_1[0]}\right)\right) \\ \vdots \\ \Im(V_m[n]) \Im\left(S_m\left(\frac{W_m[0]}{V_m[0]}\right)\right) \\ \Re(V_m[n]) \Im\left(S_m\left(\frac{W_m[0]}{V_m[0]}\right)\right) \end{array} \right] \\
= & \left[\begin{array}{c} \Re(k_1 S_1^* W_1^*[n-1]) \\ \Im(k_1 S_1^* W_1^*[n-1]) \\ \vdots \\ \Re(k_m S_m^* W_m^*[n-1]) \\ \Im(k_m S_m^* W_m^*[n-1]) \end{array} \right] - \left[\begin{array}{c} \Re\left(S_1^* \left(\frac{\sum_{k=1}^{n-1} W_1[k] V_1[n-k]}{V_1[0]} \right)^*\right) \\ \Im\left(S_1^* \left(\frac{\sum_{k=1}^{n-1} W_1[k] V_1[n-k]}{V_1[0]} \right)^*\right) \\ \vdots \\ \Re\left(S_m^* \left(\frac{\sum_{k=1}^{n-1} W_m[k] V_m[n-k]}{V_m[0]} \right)^*\right) \\ \Im\left(S_m^* \left(\frac{\sum_{k=1}^{n-1} W_m[k] V_m[n-k]}{V_m[0]} \right)^*\right) \end{array} \right] \tag{4.83}
\end{aligned}$$

We rewrite the LHS of (4.83) in a more compact form in order to show how the unknown coefficient

values can be combined into one single vector.

$$\begin{aligned}
& Y_R + \begin{bmatrix} \Re(S_1(\frac{W_1[0]}{V_1[0]})) & -\Im(S_1(\frac{W_1[0]}{V_1[0]})) & \cdots & 0 & 0 \\ -\Im(S_1(\frac{W_1[0]}{V_1[0]})) & \Re(S_1(\frac{W_1[0]}{V_1[0]})) & \cdots & 0 & 0 \\ 0 & 0 & \ddots & \vdots & \vdots \\ \vdots & \vdots & & 0 & 0 \\ 0 & 0 & \cdots & \Re(S_m(\frac{W_m[0]}{V_m[0]})) & -\Im(S_m(\frac{W_m[0]}{V_m[0]})) \\ 0 & 0 & \cdots & -\Im(S_m(\frac{W_m[0]}{V_m[0]})) & -\Re(S_m(\frac{W_m[0]}{V_m[0]})) \end{bmatrix} \tilde{\mathbf{v}}_R \\
& = \begin{bmatrix} \Re(k_1 S_1^* W_1^*[n-1]) \\ \Im(k_1 S_1^* W_1^*[n-1]) \\ \vdots \\ \Re(k_m S_m^* W_m^*[n-1]) \\ \Im(k_m S_m^* W_m^*[n-1]) \end{bmatrix} - \begin{bmatrix} \Re \left(S_1^* \left(\frac{\sum_{k=1}^{n-1} W_1[k] V_1[n-k]}{V_1[0]} \right)^* \right) \\ \Im \left(S_1^* \left(\frac{\sum_{k=1}^{n-1} W_1[k] V_1[n-k]}{V_1[0]} \right)^* \right) \\ \vdots \\ \Re \left(S_m^* \left(\frac{\sum_{k=1}^{n-1} W_m[k] V_m[n-k]}{V_m[0]} \right)^* \right) \\ \Im \left(S_m^* \left(\frac{\sum_{k=1}^{n-1} W_m[k] V_m[n-k]}{V_m[0]} \right)^* \right) \end{bmatrix} \quad (4.84)
\end{aligned}$$

In order to actually solve this linear system, the matrices on the LHS of (4.84) are combined into one rectangular admittance matrix. We call this new matrix Y'_R . It has the following member elements.

$$Y'_{R,i,j} = \begin{cases} \Re(Y_{\frac{i+1}{2}, \frac{j+1}{2}}) & i, j \text{ odd, } i \neq j \\ \Re(Y_{\frac{i+1}{2}, \frac{j+1}{2}}) + \Re\left(S_{\frac{i+1}{2}}\left(\frac{W_{\frac{i+1}{2}}[0]}{V_{\frac{i+1}{2}}[0]}\right)\right) & i, j \text{ odd, } i = j \\ -\Im(Y_{\frac{i+1}{2}, \frac{j}{2}}) & i \text{ odd, } j \text{ even, } i+1 \neq j \\ -\Im(Y_{\frac{i+1}{2}, \frac{j}{2}}) - \Im\left(S_{\frac{j}{2}}\left(\frac{W_{\frac{j}{2}}[0]}{V_{\frac{j}{2}}[0]}\right)\right) & i \text{ odd, } j \text{ even, } i+1 = j \\ \Im(Y_{\frac{i}{2}, \frac{j+1}{2}}) & i \text{ even, } j \text{ odd, } j+1 \neq i \\ \Im(Y_{\frac{i}{2}, \frac{j+1}{2}}) - \Im\left(S_{\frac{i}{2}}\left(\frac{W_{\frac{i}{2}}[0]}{V_{\frac{i}{2}}[0]}\right)\right) & i \text{ even, } j \text{ odd, } j+1 = i \\ \Re(Y_{\frac{i}{2}, \frac{j}{2}}) & i, j \text{ even, } i \neq j \\ \Re(Y_{\frac{i}{2}, \frac{j}{2}}) - \Re\left(S_{\frac{i}{2}}\left(\frac{W_{\frac{i}{2}}[0]}{V_{\frac{i}{2}}[0]}\right)\right) & i, j \text{ even, } i = j \end{cases} \quad (4.85)$$

A sample of this matrix can be expanded and shown explicitly.

$$Y'_R = \begin{bmatrix} G_{1,1} + \Re\left(S_1 \frac{W_1[0]}{V_1[0]}\right) & -B_{1,1} - \Im\left(S_1 \frac{W_1[0]}{V_1[0]}\right) & \cdots & G_{1,m} & -B_{1,m} \\ B_{1,1} - \Im\left(S_1 \frac{W_1[0]}{V_1[0]}\right) & G_{1,1} - \Re\left(S_1 \frac{W_1[0]}{V_1[0]}\right) & \cdots & B_{1,m} & G_{1,m} \\ \vdots & \vdots & \ddots & \vdots & \vdots \\ G_{m,1} & -B_{m,1} & \cdots & G_{m,m} + \Re\left(S_m \frac{W_m[0]}{V_m[0]}\right) & -B_{m,m} - \Im\left(S_m \frac{W_m[0]}{V_m[0]}\right) \\ B_{m,1} & G_{m,2} & \cdots & B_{m,m} - \Im\left(S_m \frac{W_m[0]}{V_m[0]}\right) & G_{m,m} - \Re\left(S_m \frac{W_m[0]}{V_m[0]}\right) \end{bmatrix} \quad (4.86)$$

We wish to use this method to solve the power flow problem for the entire system. As indicated by (3.52), the phasor voltages at the PV and swing buses are fixed, so $V[n] = 0$ for $n > 0$. The germ solution for the system, in this case, represents the base case power flow solution, so $V_i[0]$ is known $\forall i$. We are only concerned with solving for $V_i[n]$ for $n > 0$. If we expand (4.80) to make it length $2N$ so it can include the PV and swing bus voltage coefficients, it would have the following form (where $PQ = \{1\dots m\}$ and the remainder of the buses are generator buses).

$$\mathbf{V}_R = \begin{bmatrix} \Re(V_1[n]) \\ \Im(V_1[n]) \\ \vdots \\ \Re(V_m[n]) \\ \Im(V_m[n]) \\ 0 \\ 0 \\ \vdots \\ 0 \\ 0 \end{bmatrix} \quad (4.87)$$

Clearly, the elements of \mathbf{V}_R associated with generators, for $n > 0$, will be equal to 0. Therefore, we remove them entirely set \mathbf{V}_R back to length $2m$. The matrix (4.86) is also of size $2m \times 2m$, and it does not contain generator bus entries. It may seem impossible that the higher order coefficients of load bus voltages can be computed without knowledge of the generator bus voltages, but it must be remembered that the generator bus voltages are still present in the germ (base) solution, and are therefore “embedded” in the full solution. Generator voltages are not a function of the holomorphic parameter s . We may now formulate how to solve for the unknown n^{th} voltage power series coefficients. In doing so, we pull out the complex conjugate operator from the RHS of (4.84).

$$Y'_R \mathbf{V}_R = \left(\begin{bmatrix} \Re(k_1 S_1 W_1[n-1]) \\ -\Im(k_1 S_1 W_1[n-1]) \\ \vdots \\ \Re(k_m S_m W_m[n-1]) \\ -\Im(k_m S_m W_m[n-1]) \end{bmatrix} - \begin{bmatrix} \Re\left(S_1 \frac{\sum_{k=1}^{n-1} W_1[k] V_1[n-k]}{V_1[0]}\right) \\ -\Im\left(S_1 \frac{\sum_{k=1}^{n-1} W_1[k] V_1[n-k]}{V_1[0]}\right) \\ \vdots \\ \Re\left(S_m \frac{\sum_{k=1}^{n-1} W_m[k] V_m[n-k]}{V_m[0]}\right) \\ -\Im\left(S_m \frac{\sum_{k=1}^{n-1} W_m[k] V_m[n-k]}{V_m[0]}\right) \end{bmatrix} \right) \quad (4.88)$$

Solving for \mathbf{V}_R involves simply inverting the non singular matrix Y'_R .

$$\mathbf{V}_R = [Y'_R]^{-1} \left(\begin{bmatrix} \Re(k_1 S_1 W_1[n-1]) \\ -\Im(k_1 S_1 W_1[n-1]) \\ \vdots \\ \Re(k_m S_m W_m[n-1]) \\ -\Im(k_m S_m W_m[n-1]) \end{bmatrix} - \begin{bmatrix} \Re\left(S_1 \frac{\sum_{k=1}^{n-1} W_1[k] V_1[n-k]}{V_1[0]}\right) \\ -\Im\left(S_1 \frac{\sum_{k=1}^{n-1} W_1[k] V_1[n-k]}{V_1[0]}\right) \\ \vdots \\ \Re\left(S_m \frac{\sum_{k=1}^{n-1} W_m[k] V_m[n-k]}{V_m[0]}\right) \\ -\Im\left(S_m \frac{\sum_{k=1}^{n-1} W_m[k] V_m[n-k]}{V_m[0]}\right) \end{bmatrix} \right) \quad (4.89)$$

This final equation will allow for the recursive calculation of the holomorphic voltage coefficients.

Appendix H: Overview of Method for Critical Bus Voltage Solution

Now that the Continuation Power Flow method has been derived using HELM, the holomorphic functions can be used to predict the loading levels which will yield some critically low voltage (or any desired voltage) V_c . This is equivalent to choosing an arbitrary bus voltage value and asking this question: for a given set of loading rates, what level of load will cause a particular bus to reach the chosen voltage value? To show how this can be accomplished, we start by evaluating the Padé approximant at $s = 0$. This corresponds to the complex base load voltage at bus i .

$$V_i = \left| \frac{\sum_{n=0}^{\frac{N_c-1}{2}} A[n] (s^n)}{\sum_{n=0}^{\frac{N_c-1}{2}} B[n] (s^n)} \right|_{s=0} \quad (4.90)$$

For some value of $s = x$, loading will cause the system to reach a critical voltage magnitude (at bus i). We evaluate the Padé approximant at $s = x$ and take the magnitude of the expression.

$$V_c = \left| \frac{\sum_{n=0}^{\frac{N_c-1}{2}} A[n] (s^n)}{\sum_{n=0}^{\frac{N_c-1}{2}} B[n] (s^n)} \right|_{s=x} \quad (4.91)$$

Determining the value of x , though, which will cause the critical voltage V_c can be computed through the following algebraic steps. First, we split the magnitude operator between the numerator and the denominator, and then we multiply through by the denominator.

$$\begin{aligned} \left| \sum_{n=0}^{\frac{N_c-1}{2}} B[n] (s^n) \right| V_c &= \left| \sum_{n=0}^{\frac{N_c-1}{2}} A[n] (s^n) \right| \\ \Downarrow \\ \left| \sum_{n=0}^{\frac{N_c-1}{2}} V_c B[n] (s^n) \right| &= \left| \sum_{n=0}^{\frac{N_c-1}{2}} A[n] (s^n) \right| \end{aligned}$$

↓

$$\begin{aligned}
0 &= \left| \sum_{n=0}^{\frac{N_c-1}{2}} A[n](s^n) \right| - \left| \sum_{n=0}^{\frac{N_c-1}{2}} V_c B[n](s^n) \right| \\
&= \left| A[0] + A[1]s + A[2]s^2 + \dots \right| - \left| V_c B[0] + V_c B[1]s + V_c B[2]s^2 + \dots \right|
\end{aligned}$$

Of course, all of the coefficients are complex, so we write them as such.

$$\begin{aligned}
0 &= \left| A[0] + A[1]s + A[2]s^2 + \dots \right| - \left| V_c B[0] + V_c B[1]s + V_c B[2]s^2 + \dots \right| \\
&= \sqrt{(\Re(A[0]) + \Re(A[1])s + \dots)^2 + (\Im(A[0]) + \Im(A[1])s + \dots)^2} \\
&\quad - \sqrt{(V_c \Re(B[0]) + V_c \Re(B[1])s + \dots)^2 + (V_c \Im(B[0]) + V_c \Im(B[1])s + \dots)^2}
\end{aligned}$$

The radicals can be removed.

$$\begin{aligned}
0 &= (\Re(A[0]) + \Re(A[1])s + \dots)^2 + (\Im(A[0]) + \Im(A[1])s + \dots)^2 \\
&\quad - (V_c \Re(B[0]) + V_c \Re(B[1])s + \dots)^2 - (V_c \Im(B[0]) + V_c \Im(B[1])s + \dots)^2
\end{aligned}$$

Depending on the level of accuracy desired, the previous expression may realistically extend out to s^8 . We therefore seek to come up with a formulaic pattern for applying the exponential operator. In order to do so, we consider the following example.

$$(as^0 + bs^1 + cs^2 + ds^3 + \dots)^2$$

In order to recognize the pattern, we put these coefficients into the following vector **C**. We segment the example at ds^3 .

$$\mathbf{C} = \begin{bmatrix} a \\ b \\ c \\ d \end{bmatrix}$$

↓

$$(as^0 + bs^1 + cs^2 + ds^3)^2 = (\mathbf{C}_1 s^0 + \mathbf{C}_2 s^1 + \mathbf{C}_3 s^2 + \mathbf{C}_4 s^3)^2$$

Notice that we call \mathbf{C}_1 the first element in \mathbf{C} . We now expand the expression and group like coefficients.

$$\begin{aligned}
(\mathbf{C}_1 s^0 + \mathbf{C}_2 s^1 + \mathbf{C}_3 s^2 + \mathbf{C}_4 s^3)^2 &= [\mathbf{C}_1 \mathbf{C}_1] s^0 + \\
&\quad [\mathbf{C}_1 \mathbf{C}_2 + \mathbf{C}_2 \mathbf{C}_1] s^1 + \\
&\quad [\mathbf{C}_1 \mathbf{C}_3 + \mathbf{C}_2 \mathbf{C}_2 + \mathbf{C}_3 \mathbf{C}_1] s^2 + \\
&\quad [\mathbf{C}_1 \mathbf{C}_4 + \mathbf{C}_2 \mathbf{C}_3 + \mathbf{C}_3 \mathbf{C}_2 + \mathbf{C}_4 \mathbf{C}_1] s^3 + \\
&\quad [\mathbf{C}_2 \mathbf{C}_4 + \mathbf{C}_3 \mathbf{C}_3 + \mathbf{C}_4 \mathbf{C}_2] s^4 + \\
&\quad [\mathbf{C}_3 \mathbf{C}_4 + \mathbf{C}_4 \mathbf{C}_3] s^5 + \\
&\quad [\mathbf{C}_4 \mathbf{C}_4] s^6 +
\end{aligned} \tag{4.92}$$

We put these new coefficients into a vector \mathbf{C}' .

$$\mathbf{C}' = \left[\begin{array}{c} \mathbf{C}_1 \mathbf{C}_1 \\ \mathbf{C}_1 \mathbf{C}_2 + \mathbf{C}_2 \mathbf{C}_1 \\ \mathbf{C}_1 \mathbf{C}_3 + \mathbf{C}_2 \mathbf{C}_2 + \mathbf{C}_3 \mathbf{C}_1 \\ \mathbf{C}_1 \mathbf{C}_4 + \mathbf{C}_2 \mathbf{C}_3 + \mathbf{C}_3 \mathbf{C}_2 + \mathbf{C}_4 \mathbf{C}_1 \\ \mathbf{C}_2 \mathbf{C}_4 + \mathbf{C}_3 \mathbf{C}_3 + \mathbf{C}_4 \mathbf{C}_2 \\ \mathbf{C}_3 \mathbf{C}_4 + \mathbf{C}_4 \mathbf{C}_3 \\ \mathbf{C}_4 \mathbf{C}_4 \end{array} \right] \tag{4.93}$$

We may now write the solution as a simple sum. If s^t is the highest order of s , then $n = 2t + 1$.

$$(\mathbf{C}_1 s^0 + \mathbf{C}_2 s^1 + \mathbf{C}_3 s^2 + \mathbf{C}_4 s^3 + \mathbf{C}_5 s^4)^2 = \sum_{i=1}^n \mathbf{C}'_i s^{i-1} \quad n = 7$$

We may generalize the values of \mathbf{C}' in the following way.

$$\mathbf{C}'_i = \begin{cases} \sum_{j=1}^i \mathbf{C}_j \mathbf{C}_{i+1-j} & i \leq (t+1) \\ \sum_{j=i-t}^{t+1} \mathbf{C}_j \mathbf{C}_{i+1-j} & (t+1) < i \leq n \end{cases} \tag{4.94}$$

We show the validity of this expression for three test points: \mathbf{C}'_1 , \mathbf{C}'_4 , and \mathbf{C}'_7 .

$$\begin{aligned}
\mathbf{C}'_1 &= \sum_{j=1}^1 \mathbf{C}_j \mathbf{C}_{2-j} = \mathbf{C}_1 \mathbf{C}_1 \\
\mathbf{C}'_4 &= \sum_{j=1}^4 \mathbf{C}_j \mathbf{C}_{5-j} = \mathbf{C}_1 \mathbf{C}_4 + \mathbf{C}_2 \mathbf{C}_3 + \mathbf{C}_3 \mathbf{C}_2 + \mathbf{C}_4 \mathbf{C}_1 \\
\mathbf{C}'_7 &= \sum_{j=7-3}^4 \mathbf{C}_j \mathbf{C}_{8-j} = \mathbf{C}_4 \mathbf{C}_4
\end{aligned}$$

The expression is shown to be valid. We now return to the original problem, and we assume the largest power of s is s^t .

$$0 = (\Re(A[0]) + \Re(A[1])s + \cdots + \Re(A[t])s^t)^2 + (\Im(A[0]) + \Im(A[1])s + \cdots + \Im(A[t])s^t)^2 \\ - (V_c [\Re(B[0]) + \Re(B[1])s + \cdots + \Re(B[t])s^t])^2 - (V_c [\Im(B[0]) + \Im(B[1])s + \cdots + \Im(B[t])s^t])^2$$

↓

$$0 = (\Re(A[0]) + \Re(A[1])s + \cdots + \Re(A[t])s^t)^2 + (\Im(A[0]) + \Im(A[1])s + \cdots + \Im(A[t])s^t)^2 \\ - V_c^2 (\Re(B[0]) + \Re(B[1])s + \cdots + \Re(B[t])s^t)^2 - V_c^2 (\Im(B[0]) + \Im(B[1])s + \cdots + \Im(B[t])s^t)^2$$

To solve this problem using the previous results, we note that vectors $\tilde{\mathbf{A}}$ and $\tilde{\mathbf{B}}$ are analogous to vector \mathbf{C} above. We restate the problem using this notation, where $\tilde{\mathbf{A}}_1 = A[0]$, and s^t is the highest order of s . The expression $\tilde{\mathbf{A}}^{\Re}$ indicates the real values of the vector $\tilde{\mathbf{A}}$.

$$0 = \left(\sum_{i=0}^t \tilde{\mathbf{A}}_{i+1}^{\Re} s^i \right)^2 + \left(\sum_{i=0}^t \tilde{\mathbf{A}}_{i+1}^{\Im} s^i \right)^2 - V_c^2 \left(\sum_{i=0}^t \tilde{\mathbf{B}}_{i+1}^{\Re} s^i \right)^2 - V_c^2 \left(\sum_{i=0}^t \tilde{\mathbf{B}}_{i+1}^{\Im} s^i \right)^2 \quad (4.95)$$

Now we apply the exponential operator and employ $\tilde{\mathbf{A}}^{\Re'}$ (and its cousins) which are analogous to \mathbf{C}' . Again, the value of n is $2t+1$, where t is the highest exponent of s .

$$0 = \sum_{i=1}^n \tilde{\mathbf{A}}_i^{\Re'} s^{i-1} + \sum_{i=1}^n \tilde{\mathbf{A}}_i^{\Im'} s^{i-1} - V_c^2 \sum_{i=1}^n \tilde{\mathbf{B}}_i^{\Re'} s^{i-1} - V_c^2 \sum_{i=1}^n \tilde{\mathbf{B}}_i^{\Im'} s^{i-1} \quad (4.96)$$

Since each sum has the same indices and bounds, we may combine the expression into a single summation.

$$0 = \sum_{i=1}^n [\tilde{\mathbf{A}}_i^{\Re'} + \tilde{\mathbf{A}}_i^{\Im'} - V_c^2 \tilde{\mathbf{B}}_i^{\Re'} - V_c^2 \tilde{\mathbf{B}}_i^{\Im'}] s^{i-1} \quad (4.97)$$

At this point, we notice that the previous expression is simply a polynomial of degree $n-1$. Therefore, a numerical solver, such as the “roots” command in MATLAB, can find its roots with ease. In this case, the meaningful solution will be the single smallest, positive (real) root. This will be the value of s corresponding to the critical voltage in question.

Bibliography

- [1] V. Ajjarapu and C. Christy. The continuation power flow: a tool for steady state voltage stability analysis. *IEEE Transactions on Power Systems*, 7(1):416–423, Feb 1992.
- [2] G. Andersson, P. Donalek, R. Farmer, et al. Causes of the 2003 major grid blackouts in north america and europe, and recommended means to improve system dynamic performance. *Power Systems, IEEE Transactions on*, 20(4):1922–1928, Nov 2005.
- [3] Jhonatan Andrade dos Santos, Lampros Papangelis, Claudio a Canizares, et al. Test Systems for Voltage Stability Analysis and Security Assessment. 2015.
- [4] Sina Baghsorkhi and Sergey Suetin. Embedding ac power flow with voltage control in the complex plane : The case of analytic continuation via pad approximants. 3 2015.
- [5] A.R. Bergen and V. Vittal. *Power Systems Analysis*. Prentice Hall, 2000.
- [6] Maarten C. Boerlijst, Thomas Oudman, and Andre M. de Roos. Catastrophic collapse can occur without early warning: Examples of silent catastrophes in structured ecological models. *PLoS ONE*, 8(4), 04 2013.
- [7] Francesco Bullo, John Simpson-porco, and Florian Dorfler. Voltage collapse in complex power grids. *Nature Communications*, page 8, 2016.
- [8] C. A. Canizares, A. C. Z. De Souza, and V. H. Quintana. Comparison of performance indices for detection of proximity to voltage collapse. *IEEE Transactions on Power Systems*, 11(3):1441–1450, Aug 1996.
- [9] E. Cotilla-Sanchez, P.D.H. Hines, and C.M. Danforth. Predicting critical transitions from time series synchrophasor data. *IEEE Transactions on Smart Grid*, 3(4):1832 –1840, Dec. 2012.
- [10] Vasilis Dakos, Egbert H. Van Nes, Paolo D’Odorico, and Marten Scheffer. Robustness of variance and autocorrelation as indicators of critical slowing down. *Ecology*, 93, 2012.
- [11] Ian Dobson. Observations on the geometry of saddle node bifurcation and voltage collapse in electrical power systems. *IEEE Transactions on Circuits and Systems I: Fundamental Theory and Applications*, 39(3):240–243, 1992.
- [12] Ian Dobson. The irrelevance of electric power system dynamics for the loading margin to voltage collapse and its sensitivities. *IEICE*, 2(3):263–280, 2011.
- [13] Ian Dobson, Benjamin a. Carreras, Vickie E. Lynch, and David E. Newman. Complex systems analysis of series of blackouts: Cascading failure, critical points, and self-organization. *Chaos*, 17, 2007.
- [14] B. Gao, G.K. Morison, and P. Kundur. Voltage stability evaluation using modal analysis. *IEEE Transactions on Power Systems*, 7(4):1529–1542, 1992.

- [15] Crispin W Gardiner. *Handbook of Stochastic Methods for Physics, Chemistry, and the Natural Sciences*. Springer, Berlin, Germany, 4th edition, 2004, Sec. 4.4.6, pp. 109–112.
- [16] G. Ghanavati. *Statistical Analysis of High Sample Rate Time-Series Data for Power System Stability Assessment*. PhD thesis, University of Vermont, May 2015.
- [17] Goodarz Ghanavati, Paul D. H. Hines, Taras Lakoba, and Eduardo Cotilla-Sanchez. Calculation of the autocorrelation function of the stochastic single machine infinite bus system. In *Proceedings of the North American Power Symposium*, Sep. 2013.
- [18] Goodarz Ghanavati, Paul D. H. Hines, and Taras I. Lakoba. Identifying useful statistical indicators of proximity to instability in stochastic power systems. *IEEE Transactions on Power Systems*, (in press), 2015.
- [19] Goodarz Ghanavati, Paul D. H. Hines, Taras I. Lakoba, and Eduardo Cotilla-Sanchez. Understanding early indicators of critical transitions in power systems from autocorrelation functions. *IEEE Transactions on Circuits and Systems I: Regular Papers*, 61(9), Sep. 2014.
- [20] Goodarz Ghanavati, Paul D.H. Hines, and Taras I. Lakoba. Investigating early warning signs of oscillatory instability in simulated phasor measurements. In *Proceedings of the IEEE Power and Engineering Society General Meeting*, page 5, Washington, DC, July 2014.
- [21] J.D. Glover, M.S. Sarma, and T. Overbye. *Power System Analysis and Design*. Cengage Learning, 2011.
- [22] S. Greene, I. Dobson, and F. L. Alvarado. Sensitivity of the loading margin to voltage collapse with respect to arbitrary parameters. *IEEE Transactions on Power Systems*, 12(1):262–272, Feb 1997.
- [23] Paramjeet Kaur, Manojkumar Jaiswal, and Priyanka Jaiswal. Review and Analysis of Voltage Collapse in Power System. *International Journal of Scientific and Research Publications*, 2(1):2–5, 2012.
- [24] Prabha Kundur, John Paserba, Venkat Ajjarapu, et al. Definition and Classification of Power System Stability. *IEEE Transactions on Power Systems*, 21(3):1387–1401, 2004.
- [25] Atsushi Kurita and T. Sakurai. The power system failure on july 23, 1987 in tokyo. In *Decision and Control, 1988., Proceedings of the 27th IEEE Conference on*, pages 2093–2097 vol.3, Dec 1988.
- [26] A. A. P. Lerm, C. A. Canizares, and A. Silveira e Silva. Multiparameter bifurcation analysis of the south brazilian power system. *IEEE Transactions on Power Systems*, 18(2), May 2003.
- [27] a P Lerm, Claudio a Ca, and a B Lemos. Multi-parameter Bifurcation Analysis of Power Systems. *Electrical Engineering*, 18(October):1–7, 1998.
- [28] Federico Milano. *Power System Analysis Toolbox Reference Manual for PSAT version 2.1. 6.*, 2.1.6 edition, 5 2010.
- [29] Borka Milosevic and Miroslav Begovic. Voltage-stability protection and control using a wide-area network of phasor measurements. *IEEE Transactions on Power Systems*, 18(1):121–127, 2003.
- [30] T. Ohno and S. Imai. The 1987 tokyo blackout. In *Power Systems Conference and Exposition, 2006. PSCE '06. 2006 IEEE PES*, pages 314–318, Oct 2006.
- [31] D. Podolsky and K. Turitsyn. Random load fluctuations and collapse probability of a power system operating near codimension 1 saddle-node bifurcation. In *IEEE Power and Energy Soc. Gen. Meeting*, Jul. 2013.

- [32] L. Ramirez and I. Dobson. Monitoring voltage collapse margin with synchrophasors across transmission corridors with multiple lines and multiple contingencies. In *2015 IEEE Power Energy Society General Meeting*, pages 1–5, July 2015.
- [33] S. Rao, Y. Feng, D. J. Tylavsky, and M. K. Subramanian. The holomorphic embedding method applied to the power-flow problem. *IEEE Transactions on Power Systems*, PP(99), 2015.
- [34] Sidney Redner. *A Guide to First-Passage Processes*. Cambridge University Press, 2001. Cambridge Books Online.
- [35] G. Revel, A.E. Leon, D.M. Alonso, and J.L. Moiola. Bifurcation analysis on a multimachine power system model. *Circuits and Systems I: Regular Papers, IEEE Transactions on*, 57(4), April 2010.
- [36] P. W. Sauer and M. A. Pai. Power system steady-state stability and the load-flow jacobian. *IEEE Transactions on Power Systems*, 5(4), Nov 1990.
- [37] Marten Scheffer, Jordi Bascompte, William a Brock, Victor Brovkin, Stephen R Carpenter, Vasilis Dakos, Hermann Held, Egbert H van Nes, Max Rietkerk, and George Sugihara. Early-warning signals for critical transitions. *Nature*, 461, 2009.
- [38] A. K. Sinha and D. Hazarika. Voltage collapse proximity indicating index using diagonal element of jacobian matrix. In *Industrial Technology 2000. Proceedings of IEEE International Conference on*, volume 1, pages 480–485 vol.2, Jan 2000.
- [39] M. Subramanian. Application of holomorphic embedding to the power-flow problem. Master’s thesis, Arizona State University, July 2015.
- [40] A. Trias. The holomorphic embedding load flow method. In *2012 IEEE Power and Energy Society General Meeting*, July 2012.
- [41] I. a. van de Leemput, M. Wijchers, et al. Critical slowing down as early warning for the onset and termination of depression. *Proceedings of the National Academy of Sciences*, 111(1):87–92, 2014.
- [42] Wikipedia. Holomorphic function, 2016. Online; accessed 11-July-2016.
- [43] Wikipedia. Ornstein-uhlenbeck process, 2016. Online; accessed 11-July-2016.
- [44] C. Wissel. A universal law of the characteristic return time near thresholds. *Oecologia*, 65(1):101–107, 1984.
- [45] Yang Yang, Jianhui Wang, and Adilson E. Motter. Network observability transitions. *Physical Review Letters*, 109(25):1–22, 2012.